

EVALUATION OF THE BIAXIAL MECHANICAL PROPERTIES OF THE MITRAL  
VALVE ANTERIOR LEAFLET UNDER PHYSIOLOGICAL LOADING CONDITIONS

by

Jonathan Sayer Grashow

BS, University of Pittsburgh, 2002

Submitted to the Graduate Faculty of

The School of Engineering in partial fulfillment

of the requirements for the degree of

Master of Science

University of Pittsburgh

2005

UNIVERSITY OF PITTSBURGH

SCHOOL OF ENGINEERING

This thesis was presented

by

Jonathan Sayer Grashow

It was defended on

April 12, 2005

and approved by

Dr. Richard Debski,  
Assistant Professor, Department of Bioengineering  
Assistant Professor, Department of Orthopedic Surgery

Dr. Jiro Nagatomi,  
Research Assistant Professor, Department of Bioengineering

Dr. Michael Sacks,  
William Kepler Whiteford Professor, Department of Bioengineering  
Thesis Advisor

# EVALUATION OF THE BIAXIAL MECHANICAL PROPERTIES OF THE MITRAL VALVE ANTERIOR LEAFLET UNDER PHYSIOLOGICAL LOADING CONDITIONS

Jonathan Sayer Grashow, MS

University of Pittsburgh, 2005

It is a fundamental assumption that a repaired mitral valve (MV) or MV replacement should mimic the functionality of the native MV as closely as possible. Thus, improvements in valvular treatments are dependent on the establishment of a complete understanding of the mechanical properties of the native MV. In this work, the biaxial mechanical properties, including the viscoelastic properties, of the MV anterior leaflet (MVAL) were explored. A novel high-speed biaxial testing device was developed to achieve stretch rates both below and beyond in-vitro values reported for the MVAL (Sacks et al, ABME, Vol. 30,pp. 1280-90, 2002). Experiments were performed with this device to assess the effects of stretch rate (from quasi-static to physiologic) on the stress-stretch response in the native leaflet. Additionally, stress-relaxation and creep tests were performed on the MVAL under physiologic biaxial loading conditions.

The results of these tests showed that the stress-stretch responses of the MVAL during the loading phases were remarkably independent of stretch rate. The results of the creep and relaxation experiments revealed that the leaflet exhibited significant relaxation, but unlike traditional viscoelastic biological materials, exhibited negligible creep.

These results suggested that the MVAL may be functionally modeled as an anisotropic quasi-elastic material and highlighted the importance of performing creep experiments on soft

tissues. Additionally, this study underscored the necessity of performing biaxial experiments in order to appropriately determine the mechanical properties of membranous tissues.

## TABLE OF CONTENTS

1.0	INTRODUCTION .....	1
1.1	ANATOMY AND PHYSIOLOGY OF THE HEART.....	1
1.2	MITRAL VALVE ANATOMY .....	4
1.3	MITRAL VALVE HISTOLOGICAL STRUCTURE .....	7
1.3.1	Tri-layered leaflet structure.....	7
1.3.2	Passive components of the mitral valve.....	8
1.3.2.1	Collagen.....	8
1.3.2.2	Elastin.....	11
1.3.2.3	Glycosaminoglycans.....	11
1.3.3	Active components of the mitral valve.....	12
1.3.4	Small angle light scattering analysis of collagen architecture.....	14
1.4	MITRAL VALVE DISEASE .....	16
1.4.1	Mitral valve stenosis .....	16
1.4.2	Mitral valve regurgitation .....	17
1.5	PROSTHETIC VALVE REPLACEMENTS .....	21
1.6	VALVULAR COORDINATE SYSTEM.....	23
1.7	MITRAL VALVE DYNAMICS .....	24
1.7.1	Surface stretches of the anterior leaflet.....	27
1.8	MECHANICAL PROPERTIES OF MITRAL VALVE LEAFLETS.....	31
1.9	VISCOELASTIC BEHAVIOR .....	36

1.9.1	Stress-relaxation testing.....	37
1.9.2	Creep testing.....	38
1.9.3	Hysteresis.....	40
1.9.4	Modeling viscoelastic behavior - the Boltzmann superposition principle.....	40
1.9.5	Modelling viscoelastic behavior - quasilinear viscoelasticity.....	41
1.9.6	Stretch rate sensitivity in soft tissues.....	43
1.9.7	Creep and stress-relaxation in soft tissues.....	44
1.10	MOTIVATION FOR THE CURRENT STUDY & STUDY AIMS.....	46
1.10.1	Specific study aims.....	48
2.0	METHODS.....	49
2.1	HIGH-SPEED BIAXIAL TESTING DEVICE.....	49
2.1.1	Device specifications.....	49
2.1.1.1	Displacements and displacement rates.....	49
2.1.1.2	Maximum loads.....	50
2.1.1.3	Stretch & load measurement frequency.....	51
2.1.2	Device design.....	53
2.1.2.1	Device overview.....	53
2.1.2.2	Actuation components.....	56
2.1.2.3	Specimen attachments.....	58
2.1.2.4	Specimen bath.....	60
2.1.2.5	Stretch and load measurement.....	60
2.1.3	Device software.....	63
2.1.3.1	Marker identification.....	63

2.1.3.2	Stretch calculation.....	65
2.1.3.3	Quasi-static control.....	68
2.1.3.4	High stretch rate testing.....	70
2.1.3.5	Stress-relaxation testing.....	70
2.1.3.6	Creep testing.....	71
2.2	CHARACTERIZATION OF DEVICE PERFORMANCE.....	72
2.2.1	Stretch measurement system.....	72
2.2.2	Load cell calibration.....	73
2.2.3	Ability to reach quasi-static peak loads.....	75
2.2.4	Load cell momentum sensitivity.....	75
2.2.5	System relaxation.....	76
2.3	BIAXIAL TESTING OF THE MV ANTERIOR LEAFLET.....	77
2.3.1	Specimen preparation.....	77
2.3.2	Quasi-static biaxial testing.....	80
2.3.3	High-speed biaxial testing.....	82
2.3.4	Kinematic analysis.....	84
2.3.5	Statistical methods.....	85
3.0	RESULTS.....	86
3.1	CHARACTERIZATION OF DEVICE PERFORMANCE.....	86
3.1.1	Stretch Measurement Accuracy.....	86
3.1.2	Load cell calibration.....	87
3.1.3	Ability to reach peak loads.....	87
3.1.4	Load cell momentum sensitivity.....	88

3.1.5	System relaxation.....	91
3.2	EFFECTS OF STRETCH RATE .....	92
3.2.1	Device Control.....	92
3.2.2	Effects of Stretch Rate on Stress-Stretch Response.....	95
3.2.3	Effects of Stretch Rate on Hysteresis.....	98
3.3	STRESS-RELAXATION AND CREEP .....	103
3.3.1	Device control.....	103
3.3.2	Biaxial Stress-Relaxation.....	105
3.3.3	Uniaxial Stress-Relaxation.....	108
3.3.4	Reduced Relaxation Function Fit.....	109
3.3.5	Creep.....	110
4.0	DISCUSSION.....	113
4.1	RELEVANCE OF STUDY .....	113
4.2	MECHANICAL ANISOTROPY.....	114
4.3	STRETCH RATE EFFECTS.....	115
4.4	STRESS-RELAXATION .....	117
4.5	CREEP .....	123
4.6	RELATIONSHIP OF STRESS-RELAXATION AND CREEP .....	124
4.7	COMPARISONS TO SMALL ANGLE X-RAY SCATTERING RESULTS.....	125
4.8	STUDY LIMITATIONS .....	129
4.9	CONCLUSIONS.....	130
4.10	RECOMMENDATIONS FOR FUTURE STUDY .....	131
5.0	THESIS SUMMARY .....	133

APPENDIX A.....	134
APPENDIX B.....	136
APPENDIX C.....	166
BIBLIOGRAPHY.....	182

## LIST OF TABLES

Table 1. Specimen database.....	78
Table 2. Stretch measurement accuracy.....	86
Table 3. Peak loads for the ten cycle test using a latex test sample.....	88
Table 4. Circumferential and radial membrane tensions $\pm$ STDEV for all creep tests after the initial loading phase. ....	105

## LIST OF FIGURES

- Figure 1. A cross section of the heart looking down on the four heart valves from the atria. Reproduced from Otto CM. Valvular Heart Disease. Elsevier Inc. 2004..... 3
- Figure 2. A photograph of the MV leaflets. (A) anterior leaflet (P) posterior leaflet. Reproduced from Otto CM. Valvular Heart Disease. Elsevier Inc. 2004..... 5
- Figure 3. Diagram from a pathological perspective with division of the septum illustrating the fibrous continuity between the mitral and aortic valves. Reproduced from Anderson RH, Wilcox BR: The anatomy of the mitral valve, in Wells FC, Shapiro LM (eds): Mitral Valve Disease. Oxford, England, Butterworth-Heinemann, 1996. .... 6
- Figure 4. The organization of tropocollagen molecules to form collagen fibrils. Reproduced from Fung, Y.C., Biomechanics: Mechanical Properties of Living Tissues. 2nd ed. 1993, New York: Springer Verlag. 568..... 8
- Figure 5. Schematic showing the hydrogen bonding between strands that is responsible for collagen's strength (A) and the tri-helical structure that the three collagen strands take when they assemble into a collagen fiber (B). Reproduced from Voet, Biochemistry, 1995 ..... 10
- Figure 6. Picture illustrates the extensive branching characteristic of GAG molecules which account for their ability to attract and retain water molecules to enhance their molecular volume. Reproduced from Alberts, Molecular Biology of the Cell, 1994. .... 13
- Figure 7. A map of the collagen fiber architecture of the MV anterior leaflet. Colors from red (highly aligned) to blue (randomly aligned) represent the degree of collagen alignment. ... 15
- Figure 8. (A, B) 2D echocardiographic images of mitral valve regurgitation in diastole and systole respectively. (C) Color flow Doppler image showing the eccentric jet of regurgitation. Reproduced from Otto CM. Valvular Heart Disease. Elsevier Inc. 2004... 19
- Figure 9. Typical Pressure-Volume loops for the normal heart, mitral regurgitation, and aortic regurgitation. Reproduced from Otto CM. Valvular Heart Disease. Elsevier Inc. 2004... 20
- Figure 10. On-X bileaflet pyrolytic carbon mechanical aortic valve (MCRI Inc.)..... 21
- Figure 11. Porcine aortic valve (Edwards Lifesciences) ..... 22

Figure 12. A drawing, looking down on the mitral orifice, showing the circumferential and radial specimen axes. Reproduced from May-Newman and Yin. Biaxial Mechanical Properties of the Mitral Valve leaflets. American Journal of Physiology, 1995.	23
Figure 13. Drawing of balance of forces in mitral apparatus in the left panel. In the right panel, potential effect of papillary muscle displacement to restretch leaflet closure, causing mitral regurgitation. Reproduced from Liel-Cohen N, Guerrero JL, Otsuji Y. Design of a new surgical approach for ventricular remodeling. Circulation, 2000; 101: 2756.	25
Figure 14. Motion of marker placed on free edge of anterior leaflet. Reproduced from Tsakiris AG, Gordon DA, Mathieu Y, et al: Motion of both mitral valve leaflets: a cineroentgenographic study in intact dogs. J Appl Physiol 1975; 39:359.	26
Figure 15. Left-heart simulating flow loop used by Sacks et al to quantify the surface stretches of the MV anterior leaflet. Reproduced from Sacks et al. Surface stretches in the anterior leaflet of the functioning mitral valve.	28
Figure 16. Principle stretches observed in left heart-simulating flow loop (closed symbols) and in vivo using sonomicrometry method (open symbols). Reproduced from Sacks MS et al. In-vivo dynamic deformation of the mitral valve leaflet. Annals of Thoracic Surgery. Submitted 2005.	29
Figure 17. Principle stretch rates versus time for the MV anterior leaflet under normal physiologic conditions. Reproduced from Sacks MS et al. In-vivo dynamic deformation of the mitral valve leaflet. Annals of Thoracic Surgery. Submitted 2005.	30
Figure 18. Experimental setup for biaxial mechanical testing of the MV leaflet. Reproduced from May-Newman and Yin. Biaxial Mechanical Properties of the Mitral Valve leaflets. American Journal of Physiology, 1995.	32
Figure 19. Membrane stress-stretch relations from porcine anterior (A) and posterior (B) leaflets comparing equibiaxial (open symbols) and strip biaxial (filled symbols) protocols. Circles, circumferential axis; triangles, radial axis. Reproduced from May-Newman and Yin. Biaxial Mechanical Properties of the Mitral Valve leaflets. American Journal of Physiology, 1995.	33
Figure 20. Pressure - areal stretch relationship of the MV anterior leaflet measured in left heart-simulating flow loop. Reproduced from Sacks et al. Surface stretches in the anterior leaflet of the functioning mitral valve.	34
Figure 21. (a) The seven loading protocols used to characterize the biaxial stress-stretch response, and (b) response to all loading protocols for an AV cusp (open circles), along with the structural model fit, demonstrating an excellent fit.	35

Figure 22. (b) The stress-relaxation responses to three different stretch histories (a). Reproduced from Wineman AS, Rajagopal KR, Mechanical Response of Polymers. Cambridge University Press. 2000. ....	38
Figure 23. The creep responses (b) to three different stress histories (a). Reproduced from Wineman AS, Rajagopal KR, Mechanical Response of Polymers. Cambridge University Press. 2000. ....	39
Figure 24. The high-speed biaxial testing device mounted on a vibration isolation table.....	53
Figure 25. Overhead schematic of the high speed biaxial testing device; a) stepper motors; b) screw-driven linear actuators; c) load cells; d) specimen bath outlet; e) specimen bath inlet; f) heating element maintained bath temperature at 37°C; g) high speed digital camera; h) standard digital camera; i) beam splitter; j) sub specimen mirror. ....	55
Figure 26. Two computers used to control the biaxial testing device. ....	57
Figure 27. A CAD model of one suture attachment arm. (A) Custom suture attachments were designed to balance the force applied by each carriage through all four suture lines. (B) Specimens were mounted to these attachment arms in a trampoline fashion by attaching two loops of 000 nylon suture to each side of the specimen via four stainless steel surgical staples. (C) Specimen.....	59
Figure 28. A CAD model of the cross-shaped specimen bath with specimen window/stand. ....	61
Figure 29. The dual biaxial testing device dual camera system. ....	62
Figure 30. A sample bitmap showing four markers (black) and the user-defined marker subregions (green).....	64
Figure 31. Marker coordinates were mapped into an isoparametric coordinate system.....	66
Figure 32. A photograph of the calibration fixture mounted on the bath. ....	74
Figure 33. Diagram of the native mitral valve. Square specimens were taken from the anterior leaflet with sides parallel to the circumferential and radial axes of the leaflet centered circumferentially and extending radially from just below the annulus to just above the first chordae tendineae attachment site. ....	79
Figure 34. Biaxial stretch rate sensitivity, creep, stress-relaxation, and uniaxial stress-relaxation protocols.....	81
Figure 35. Specimens were mounted in the biaxial testing device with the circumferential and radial specimen axes aligned with the device axes. ....	82

Figure 36. Load versus time curves for the loaded axis (closed symbols) and unloaded axis (open symbols) showed that the load cell on the unloaded axis was not affected by rapid motions.....	89
Figure 37. Residuals versus time for the unloaded axis showed no clear trend, further indicating that the unloaded axis was not affected by rapid motions. ....	90
Figure 38. Relaxation of the biaxial test system and sutures. Both device axes (open symbols: device axis 1, closed symbols: device axis 2) showed minimal relaxation and were indistinguishable from each other.....	91
Figure 39. Typical tension-stretch curves for the initial and final 1s loading/unloading protocols. ....	93
Figure 40. Typical (a)Load versus time and (b)stretch versus time curves for 1s and 0.1s loading periods. The load versus time and stretch versus time curves were similar for the full range of cycle periods. As displayed above, the device was able to accurately control rise time for different cycle periods. Note the different time scales between the 1s and 0.1s plots.....	94
Figure 41. Typical tension-stretch curves for each loading cycle period (15s, 1s, 0.5s, 0.1s, and 0.05s) for the circumferential (a) and radial (b) specimen directions. Curves generally showed no apparent stretch rate-dependence. Note the different stretch scales between the circumferential and radial plots. ....	96
Figure 42. The circumferential and radial stretches of the leaflet at the 90 N/m equitension state. ....	97
Figure 43. Loading and unloading membrane tension (T) vs. stretch curves for 15, 1, 0.5 and 0.1 second loading and unloading of a single specimen.....	100
Figure 44. Membrane stretch energy versus membrane tension for a typical loading cycle. Note the larger amount of energy storage in the tissue at lower tension levels due to the relatively higher tissue extensibility at low stretch levels.....	101
Figure 45. Energy stored or dissipated within the leaflet specimens during loading and unloading phases with different cycle times.....	102
Figure 46. Typical membrane tension versus time curves for the first 500 ms of a biaxial stress-relaxation experiment. The biaxial stretching mechanism was able to load the specimens within the allotted 100 ms rise time with minimal vibrations and overshoot.....	104
Figure 47. Membrane tension versus time curves for a typical stress-relaxation experiment. Membrane tension levels at 3 hours were statistically less than those immediately after loading (100 ms) for both specimen axes. ....	106

Figure 48. Relaxation percentage for different test groups and specimen axes. Relaxation was observed in both uniaxial and biaxial experiments, however, the amount of radial relaxation was significantly greater in the biaxial experiments and the circumferential and radial relaxation percentages were not statistically different in the uniaxial experiments as they were in the biaxial experiments. .... 107

Figure 49. The one phase reduced relaxation model fit both the uniaxial (pictured) and biaxial relaxation data very well for both the circumferential and radial (pictured) axes. .... 109

Figure 50. Stretch versus time curves for a typical biaxial creep experiment. Minimal relaxation was observed on either axis. Note the anisotropic leaflet behavior exhibited by the relatively higher radial stretch required to maintain the 90 N/m membrane tension. .... 111

Figure 51. Creep percentages were not statistically different from zero for any time point on the circumferential or radial axes. .... 112

Figure 52. Changes in stretch over the three hour duration of the stress relaxation experiments compared to the changes in stretch required to reach the same membrane tension in quasi-static unloading cycle. .... 118

Figure 53. In uniaxial stress-relaxation experiments, stretch levels increased for axes under tension and decreased on the free axis. Data presented as mean  $\pm$  SEM. .... 120

Figure 54. Changes in collagen D-spacing as a function of membrane tension (left). Membrane tension versus areal stretch % for the same MVAL specimen. Reproduced from Liao, J. Unpublished Communication. .... 126

Figure 55. D-spacing as a function of creep experiment duration (left). Areal stretch as a function of creep test duration for the same specimen (right). Reproduced from Liao, J. Unpublished Communication. .... 127

Figure 56. Normalized membrane tension versus stress-relaxation test duration (top). Collagen D-spacing as a function of stress-relaxation test duration for the same specimen (bottom). Reproduced from Liao, J. Unpublished Communication. .... 128

## ACKNOWLEDGEMENTS

Although I have worked at the Engineered Tissue Mechanics Laboratory (ETML) for five years, sometimes I feel like it has only been a week, and other times I feel like I can't remember what it was like to do anything else. My time at ETML was spent with many great people whom I could not have survived without. I would like to thank ( in no particular order) Dan Hildebrand, Thanh Lam, Claire Gloeckner, Wei Sun, W. David Merryman, Hiroatsu Sugimoto, Ajay Abad, Khashayar Toosi, John Stella and George Engelmayr for all of their help. I would also like to thank my committee members, Drs. Debski, Nagatomi and Sacks for all of their advice and help with my thesis.

Outside of the laboratory, I also owe many thanks to my parents for the plethora of positive energy and pixie dust that have fueled my most important achievements. Also, I would like to thank to Kathryn Beardsley and Sol Dostilio for moral support and for convincing me that, "yes, I would actually finish my thesis one day."

## **1.0 INTRODUCTION**

### **1.1 ANATOMY AND PHYSIOLOGY OF THE HEART**

The heart propels blood through the circulation, providing necessary nutrients and removing waste products from the many organ systems throughout the body. The mammalian heart consists of four chambers: the left and right atria and the left and right ventricles (Figure 1). The walls of these chambers are composed of myocardium which contracts, allowing each chamber to function as a positive displacement pump. The right atrium fills with blood from the systemic and coronary circulation via the superior and inferior vena cava. From the right atrium blood moves into the right ventricle which, in turn, pumps the blood into the pulmonary circulation where it is oxygenated in the lungs. The left atrium fills with blood returning from the pulmonary circulation via the pulmonary veins. This blood is pumped into the left ventricle which, in turn, pumps the blood through the systemic and coronary circulation via the aorta and coronary arteries.

Each cardiac chamber pumps blood through a one way valve. The mitral and tricuspid valves, are known as the atrioventricular valves due to their location between the atria and ventricles. These valves prevent retrograde flow from the left and right ventricles respectively during ventricular contraction or “systole.” The mitral valve has two leaflets while the tricuspid

valve, as its name denotes, has three leaflets. The leaflets of the atrioventricular valves are tethered to papillary muscles, located within the respective ventricles, via thin tendinous structures known as chordae tendineae. A second pair of valves, the aortic and pulmonary valves, are known as the semi-lunar valves. These valves each have three leaflets, but the leaflets lack the chordal attachments present on the atrioventricular valves. The aortic valve is located between the left ventricle and the aorta, while the pulmonary valve is located between the right ventricle and the pulmonary arteries.

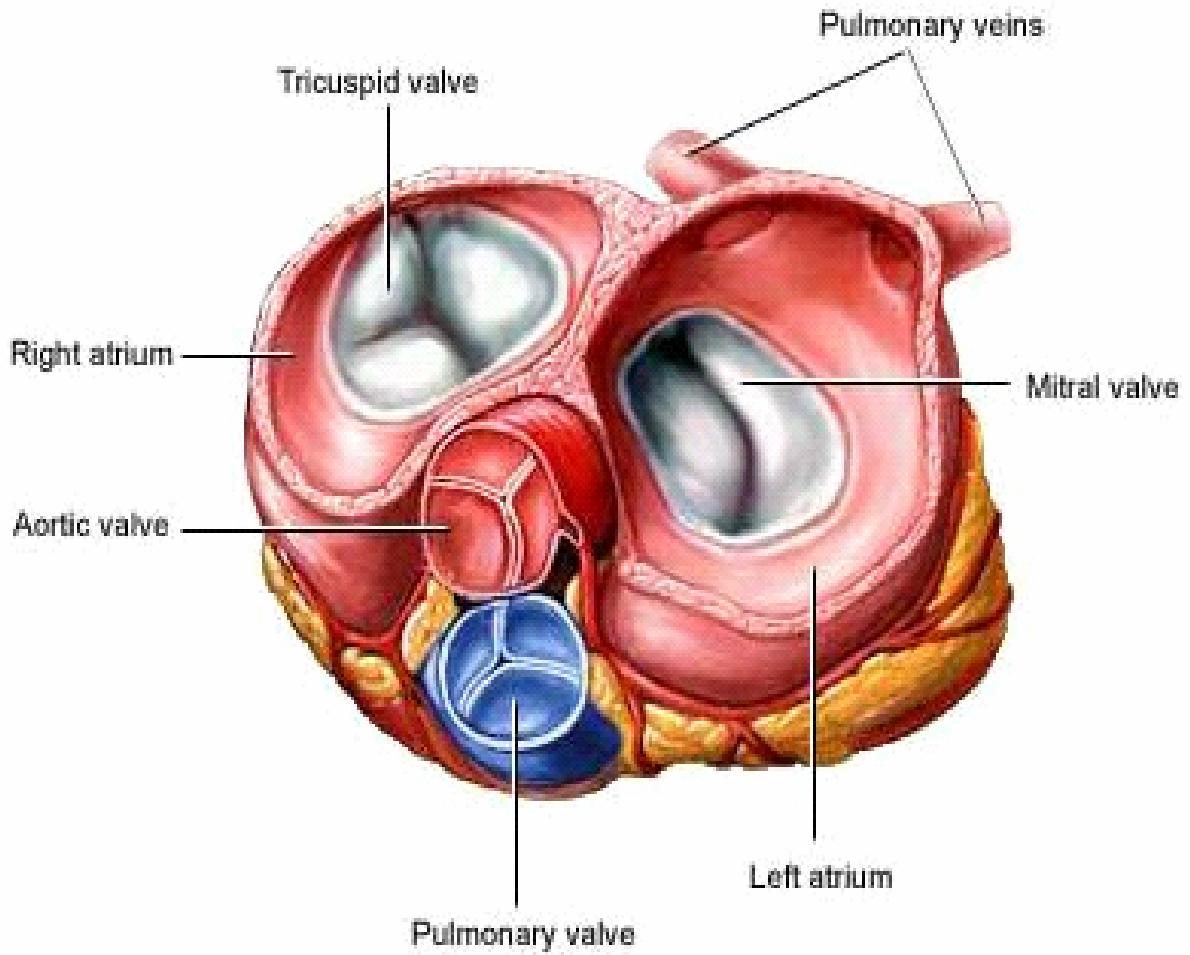


**Figure 1. A cross section of the heart looking down on the four heart valves from the atria.**

**Reproduced from Otto CM. Valvular Heart Disease. Elsevier Inc. 2004.**

## 1.2 MITRAL VALVE ANATOMY

The mitral valve (MV) serves to prevent blood regurgitation into the left atrium during left ventricular contraction. The complete valve apparatus consists of a saddle-shaped annulus that adjoins the base of the left atrium to the two valve leaflets (anterior and posterior), which extend into the ventricle where they are connected to the papillary muscles via an intricate arrangement of chordae tendineae [1-5]. The mitral annulus consists of both fibrous and muscular tissue. The two major collagenous structures within the annulus are referred to as fibrous trigones. (Figure 3) Thin collagen bundles called the fila of Henle stretch circumferentially from each trigone into the mitral orifice. The annular muscle, predominant in the posterior region of the annulus, is primarily oriented orthogonally to the annulus. When the MV is opened by cutting one of the leaflets as in (Figure 2), no distinct separation is observed between the two leaflets. The anterior leaflet is generally somewhat larger and has a smooth appearance while the posterior leaflet tends to be smaller and has a scalloped texture.

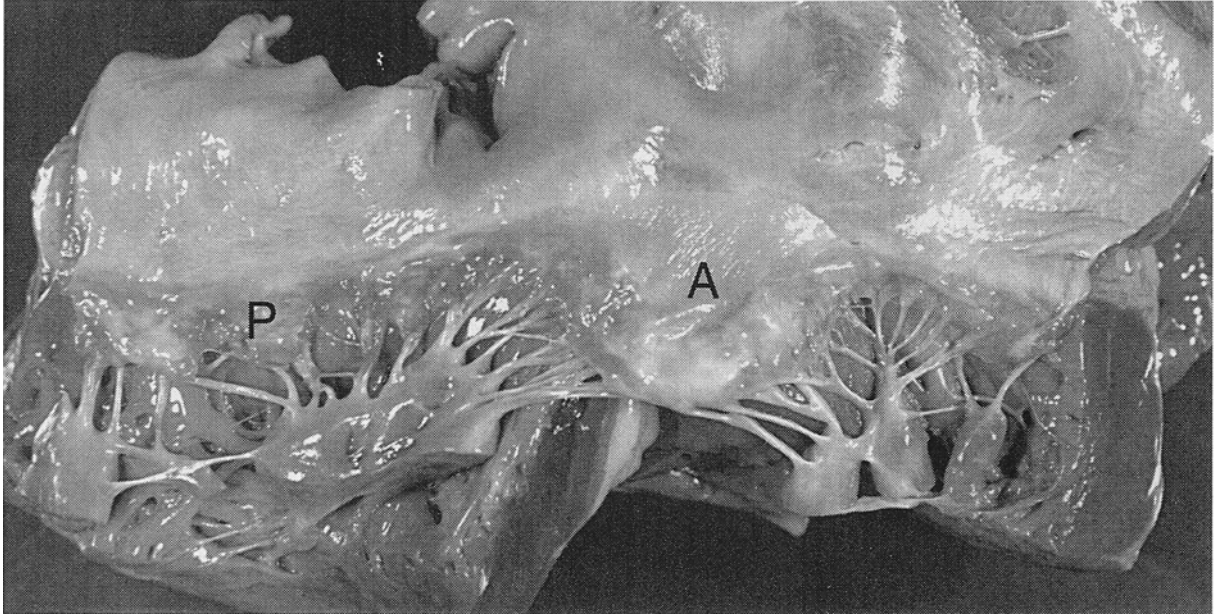


**Figure 2. A photograph of the MV leaflets. (A) anterior leaflet (P) posterior leaflet.  
Reproduced from Otto CM. Valvular Heart Disease. Elsevier Inc. 2004.**

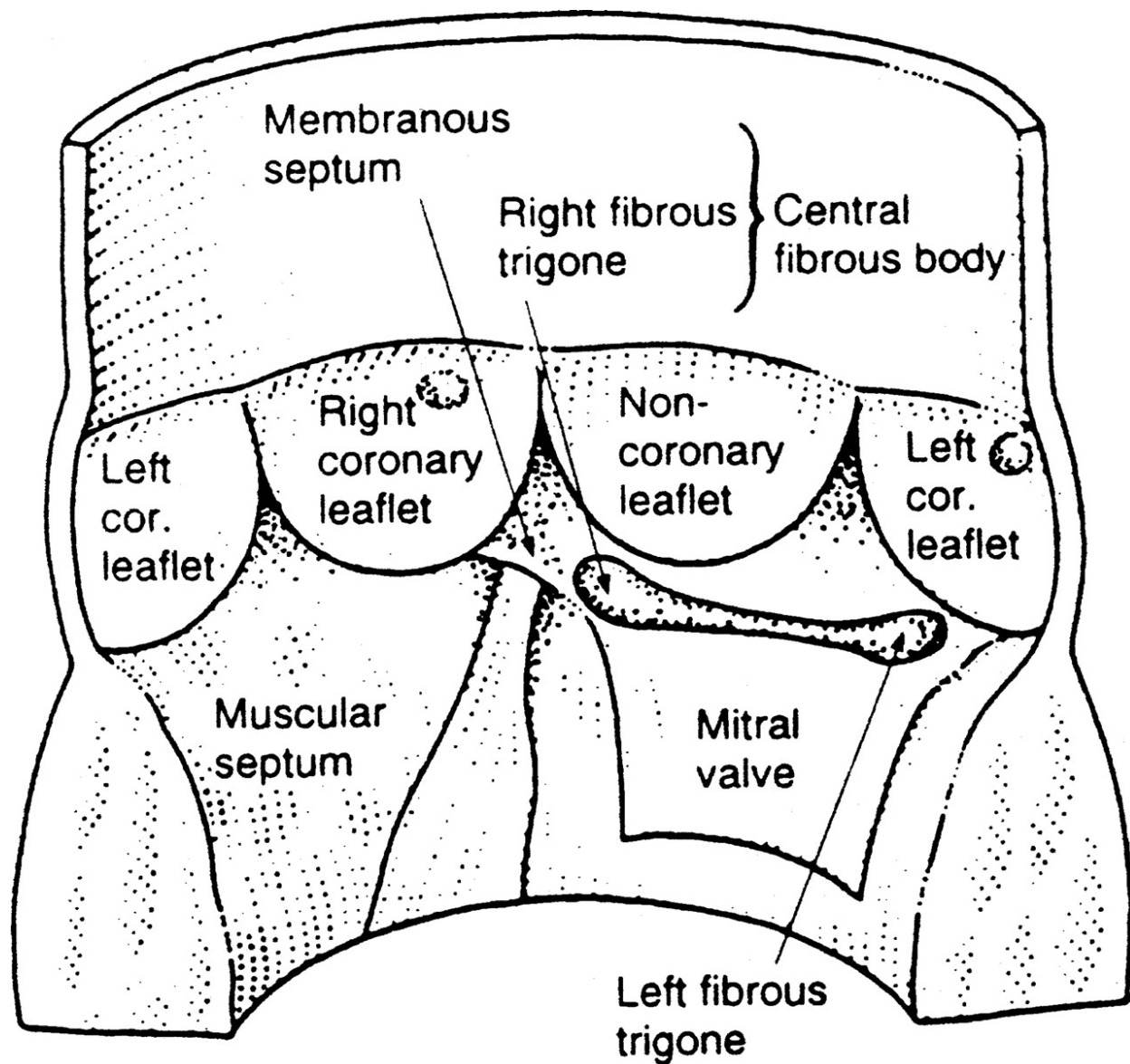


Figure 3. Diagram from a pathological perspective with division of the septum illustrating the fibrous continuity between the mitral and aortic valves. Reproduced from Anderson RH, Wilcox BR: The anatomy of the mitral valve, in Wells FC, Shapiro LM (eds): Mitral Valve Disease. Oxford, England, Butterworth-Heinemann, 1996.

## **1.3 MITRAL VALVE HISTOLOGICAL STRUCTURE**

### **1.3.1 Tri-layered leaflet structure**

The MV leaflets are composed of three membranous layers [6]. Beginning on the atrial side, the first layer, termed the spongiosa, consists of proteoglycans, elastin, and a variety of connective tissue cells. The spongiosa contains a relatively small number of collagen fibers when compared to the other two layers. The core of the leaflets is named the fibrosa due to its large collagenous content. This layer is thought to bear the majority of the loads applied to the leaflets evidenced by the fact that collagen fibers from this layer have been shown to extend directly into the chordae tendineae. Both the spongiosa and the fibrosa are wrapped in a thin fibrous layer composed of densely packed elastin fibers. On the atrial side of the leaflet, covering the spongiosa, this layer is termed the atrialis while on the ventricular side of the leaflet this layer is termed the ventricularis. The ventricularis predominantly covers the anterior leaflet and contains higher collagen content than the atrialis. Additionally, the ventricularis may thicken with age due to increases in collagen and elastin content.

### 1.3.2 Passive components of the mitral valve

1.3.2.1 **Collagen.** The term collagen fiber describes an intricately arranged set of tropocollagen molecules. Three single chains are wound around each other in a left handed  $\alpha$ -helix. Each of these chains contains approximately one third glycine, one third proline and hydroxyproline, and one third other amino acids. These left-handed helices are then wrapped together to form a right-handed super helix (Figure 4). The integrity of this helical structure is maintained by the interactions of proline and glycine amino acid residues. Additionally, hydroxylated proline and lysine residues serve to further stabilize the structure via hydrogen bonding interactions. These tropocollagen molecules are then assembled into collagen fibrils (Figure 5) which are organized fibers with diameter on the scale of a single micrometer.

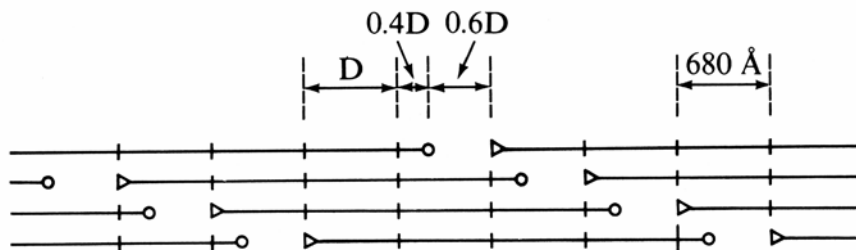


**Figure 4. The organization of tropocollagen molecules to form collagen fibrils. Reproduced from Fung, Y.C., Biomechanics: Mechanical Properties of Living Tissues. 2nd ed. 1993, New York: Springer Verlag. 568.**

To date, over 30 distinct types of collagen have been identified. Valve leaflets are composed mainly of type I collagen with some type III collagen. Collagen is strongest in tension and primarily serves as a load bearing mechanism. Collagen fibers are typically crimped in their stress-free configuration [7]. Due to this arrangement, in some cases collagen fibers may not develop their full load bearing capacity until they are sufficiently distended.

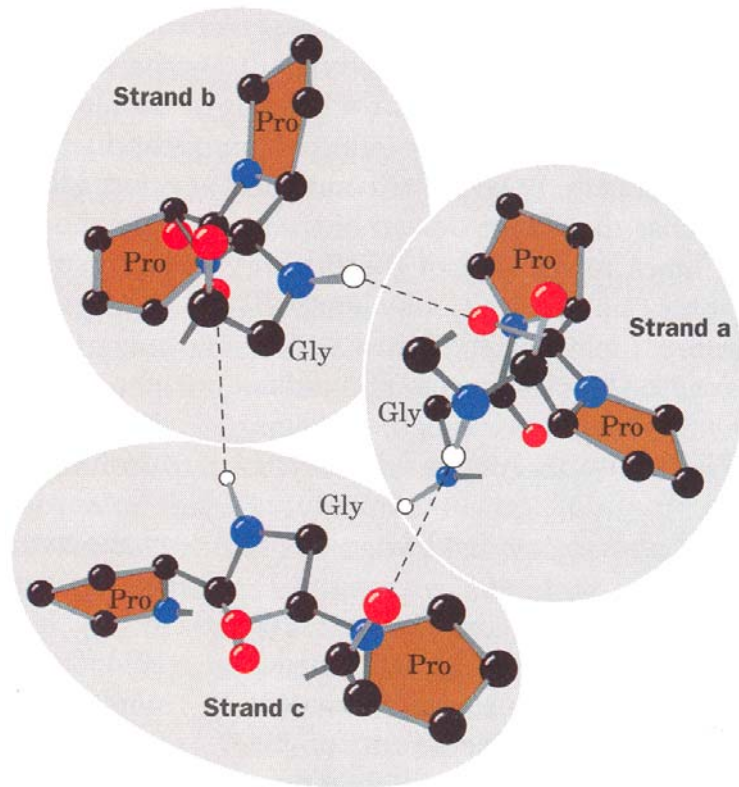


**Figure 5. Schematic showing the hydrogen bonding between strands that is responsible for collagen's strength (A) and the tri-helical structure that the three collagen strands take when they assemble into a collagen fiber (B). Reproduced from Voet, Biochemistry, 1995**

1.3.2.2 **Elastin.** Elastin fibers are composed of proline and glycine rich amino acid linkages that do not possess the stabilizing hydroxylated or glycosylated residues present in collagen. Elastin fibers are known to be highly distensible when compared to collagen and therefore the mechanical contribution of elastin to load bearing is most noticeable when the collagen fibers are not fully recruited. The highly branched structure of elastin typically contains many coiled fibers. This coiling is hypothesized to allow the elastin fibers to retain elastic mechanical properties even when highly distended.

1.3.2.3 **Glycosaminoglycans.** Glycosaminoglycans (GAGs) are composed of a series of are negatively charged unbranched polysaccharides attached to a protein core (Figure 6). The negative charges of the GAGs cause these molecules to be highly hydrophilic. This property allows GAGs to retain a relatively large volume of water given their molecular weight. Because of the GAG content, valve leaflets typically contain a large amount of water which enables them to resist compressive forces due to the incompressibility of water.

### **1.3.3 Active components of the mitral valve**

In addition to the previously mentioned passive components, the MV leaflets contain cells that may actively contribute to the leaflets' mechanical properties such as myocardium, smooth muscle and contractile interstitial cells. These cells are supplied with blood by a sparse arrangement of blood vessels which runs throughout the leaflets. The MV leaflets are innervated with both adrenergic and cholinergic nerves [8, 9] and recent evidence has shown that neural control may play a role in controlling some of the finer motions of the leaflets such as regulating the precise leaflet deformations necessary for proper leaflet coaptation.

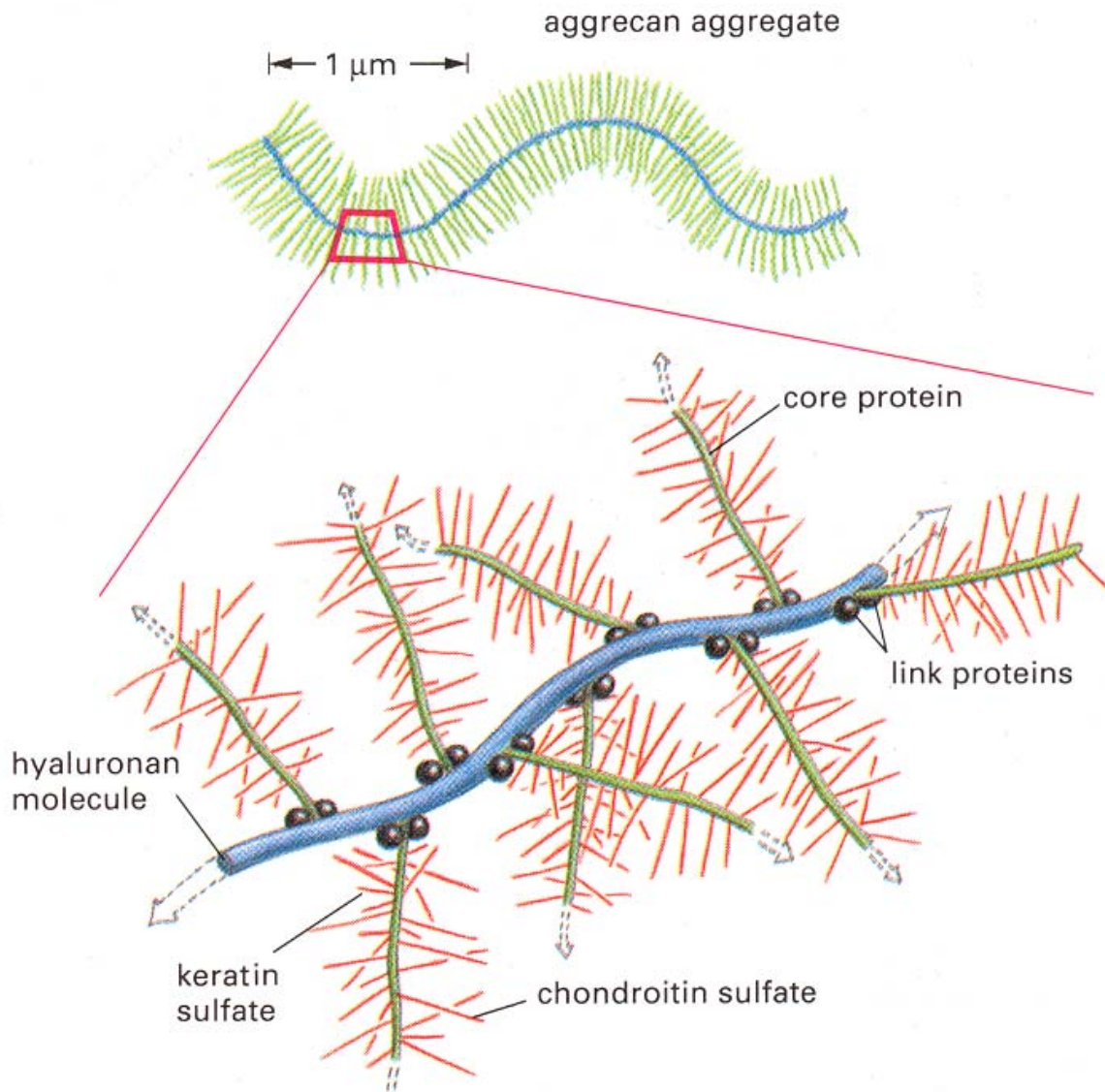


**Figure 6. Picture illustrates the extensive branching characteristic of GAG molecules which account for their ability to attract and retain water molecules to enhance their molecular volume. Reproduced from Alberts, Molecular Biology of the Cell, 1994.**

#### **1.3.4 Small angle light scattering analysis of collagen architecture**

The orientation of collagen fibers within the MV anterior leaflet has been examined using a small angle light scattering (SALS) technique (Figure 7). This technique consists of directing a helium neon laser through dehydrated tissue specimens and recording the subsequent beam diffraction [10]. According to the principles of Fraunhofer Diffraction, the laser light scatters in a direction orthogonal to the fibers within the beam envelope. Based on this principle, the collagen fiber orientations can be reconstructed from the recorded diffraction pattern.

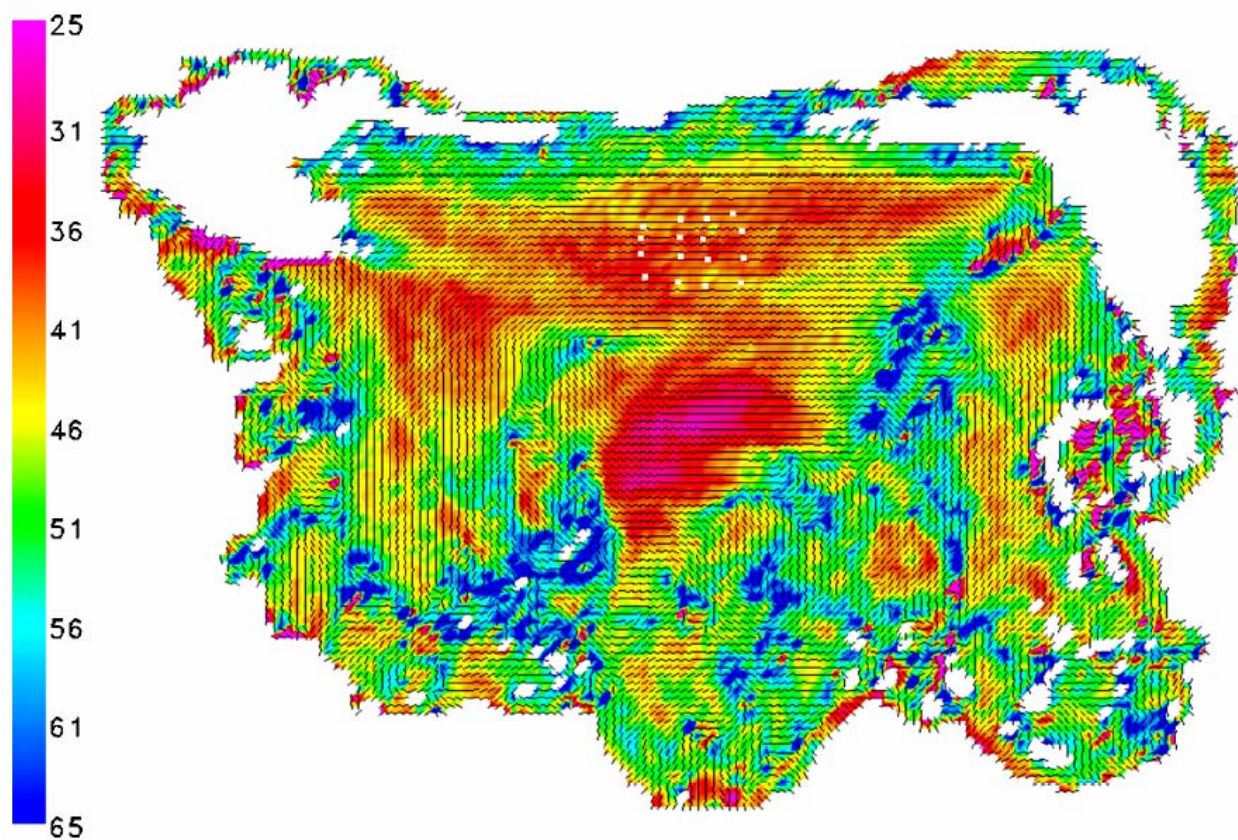


**Figure 7. A map of the collagen fiber architecture of the MV anterior leaflet. Colors from red (highly aligned) to blue (randomly aligned) represent the degree of collagen alignment.**

## **1.4 MITRAL VALVE DISEASE**

Diseases of the MV can be logically separated into two categories: those that cause left ventricular inflow obstruction, termed MV stenosis, and those that allow retrograde flow from the left ventricle during systole, termed MV regurgitation.

### **1.4.1 Mitral valve stenosis**

The most widely recognized symptoms of MV stenosis are associated primarily with pulmonary venous congestion or low cardiac output. Additionally, systemic thromboembolism may occur. In general, thromboembolic events are much more common in patients with MV stenosis or a combination of MV stenosis and regurgitation than they are in patients with MV regurgitation alone. The most common cause of MV stenosis is rheumatic heart disease which causes occlusion of the mitral orifice due to structural changes, such as scarring, to the valve leaflets [11]. 20 million cases of rheumatic fever are reported annually, with this condition being particularly prevalent in third world countries [12]. It is believed that rheumatic MV stenosis typically begins before the age of twenty, but may take up to thirty years to fully develop into a clinically important condition. Other causes of MV stenosis include MV calcification, congenital mitral valve deformities, thrombus formation within the left atrium, and certain inherited metabolic diseases.

Although this condition develops with a relatively long time course, preemptive treatment is generally not performed since the primary treatment is surgical intervention. Surgical options

include both valvular repair and replacement. In order to repair the stenotic valve, a surgeon typically removes the leaflet-like regions between the anterior and posterior leaflets known as commissures in order to create a larger mitral orifice. Replacement of the MV with a prosthetic valve may be superior to repair in this case. Patients who undergo MV replacement have a reduced need for additional procedures in the first ten years following implantation [13].

#### **1.4.2 Mitral valve regurgitation**

The most common valve disorder, affecting five to twenty percent of the population [14], is mitral valve prolapse (MVP) (Figs. 8, 9), in which the MV leaflets coapt improperly and allow leakage from the ventricle into the atrium during systole. In MVP one or both of the leaflets typically extend above the plane of the atrioventricular junction during ventricular contraction. In the United States, MVP results in 4000 mitral valve surgical procedures (25% of all cases), 1000 cases of endocarditis (10% of all cases), and 4000 cases of sudden death [3]. Symptoms of MV prolapse may include chest pain, palpitations, dyspnea, fatigue, and dizziness. Acute cases of MV leakage may trigger the onset of cardiogenic shock, while chronic mitral regurgitation may affect the geometric structure of the ventricle [15] and may lead to pulmonary edema [16]. MVP is often correlated with symptoms of myxomatous mitral valve disease such as opaque and thickened leaflets and chordal elongation, thinning, and rupture.

Current treatment for the diseased MV includes surgical repair and valve replacement. Repair techniques include partial leaflet resection, chordal transplantation, chordal shortening, insertion of artificial chordae, and edge-to-edge leaflet apposition [17-21]. These methods are

usually accompanied with annuloplasty [22, 23] which, is thought to increase the durability of the repair by stabilizing the valve [24].

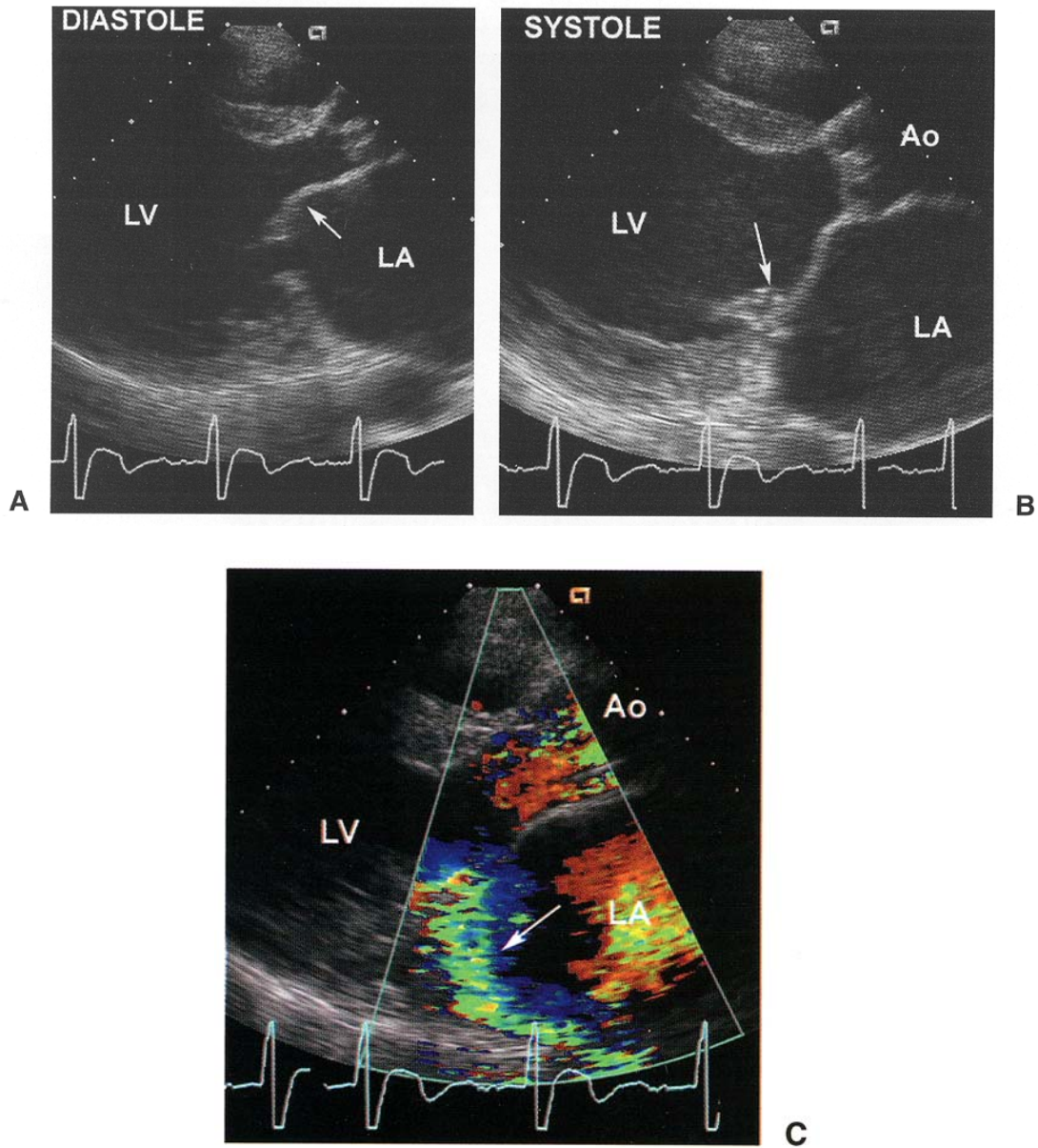


**Figure 8. (A, B) 2D echocardiographic images of mitral valve regurgitation in diastole and systole respectively. (C) Color flow Doppler image showing the eccentric jet of regurgitation. Reproduced from Otto CM. Valvular Heart Disease. Elsevier Inc. 2004.**

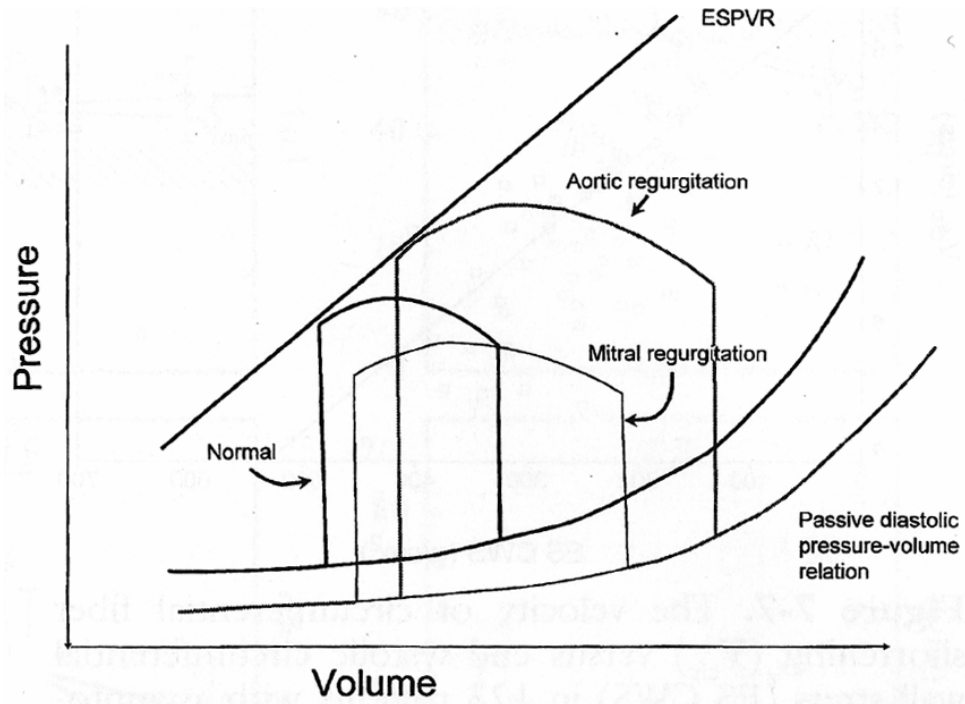


**Figure 9. Typical Pressure-Volume loops for the normal heart, mitral regurgitation, and aortic regurgitation. Reproduced from Otto CM. Valvular Heart Disease. Elsevier Inc. 2004.**

## 1.5 PROSTHETIC VALVE REPLACEMENTS

In many instances, damage to the MV is too severe for the valve to be effectively repaired and the valve must be replaced with a prosthetic valve. Mechanical valves are completely fabricated from synthetic materials (Figure 10). These implants pose an increased risk of thromboembolism, so that patients require continuous anticoagulation therapy for the lifetime of the implant. Additionally, the hemodynamic characteristics of mechanical valves do not perfectly duplicate those of the native valve, often causing hemolysis.



**Figure 10. On-X bileaflet pyrolytic carbon mechanical aortic valve (MCRI Inc.)**

“Bioprosthetic” alternatives (Figure 11) (made of biologically-derived, chemically modified collagenous tissues) greatly reduce the risks associated with mechanical valves, but have limited durability and may require anti-calcification treatment to prevent material failure [25].



**Figure 11. Porcine aortic valve (Edwards Lifesciences)**

## 1.6 VALVULAR COORDINATE SYSTEM

The coordinate system used to describe orientation with respect to the valve, is typically based on the circumferential and radial specimen axes (Figure 12). The circumferential direction describes the axis that would be created by following the mitral orifice about its circumference, while the radial direction is defined as the direction orthogonal to the circumferential axis which typically is parallel to the path from the atrium into the ventricle.

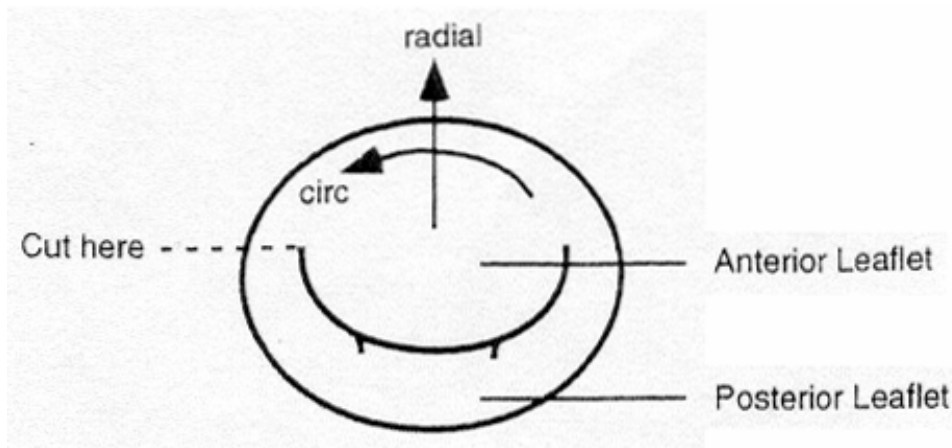


**Figure 12. A drawing, looking down on the mitral orifice, showing the circumferential and radial specimen axes. Reproduced from May-Newman and Yin. Biaxial Mechanical Properties of the Mitral Valve leaflets. American Journal of Physiology, 1995.**

## 1.7 MITRAL VALVE DYNAMICS

The proper and coordinated action of each of the components of the MV apparatus (Figure 13) is critical to the normal function of the valve [26-28]. The majority of blood flow through the MV occurs at the beginning of diastole. This flow is driven primarily by passive forces supplemented with relaxation of the left ventricular myocardium and active movement of the mitral annulus.[24]. In order to properly regulate the left ventricular volume, the mitral orifice must become enlarged beyond the size of the aortic valve. Typically, enlargement of the mitral orifice starts just before the end of systole and the orifice returns to its original, smaller size at the end of diastole [2].

During ventricular systole valve closure occurs when the two leaflets coapt to form an arc-shaped closure line. While the valve is closed, both the anterior and posterior MV leaflets are generally shaped with a concave curvature to the left ventricle [29]. After ventricular systole is completed, the valve leaflets open starting from the center of the leaflets [30] and quickly reverse their curvature into a convex formation with respect to the left ventricle. Subsequently, the leaflets straighten and the edges of the valve separate. The larger anterior leaflet then continues to open, reaching a position more widely open than that of the posterior leaflet. As systole becomes eminent, the anterior leaflet then moves towards the closed configuration at a much faster rate than the posterior leaflet ensuring that the leaflets coapt properly and then return to the concave closed configuration. Analysis of MV leaflet dynamics was performed by Tsakiris et al [31], who measured the motions of both the anterior and posterior leaflets by tracking radiopaque markers sutured onto the valve leaflets and annulus using film angiograms and correlated the marker displacements with an electrocardiogram. Of particular relevance is

their analysis of the anterior leaflet (Figure 14) which showed the closing time of the leaflet to be approximately 63 milliseconds and the opening time to be approximately 42 seconds.

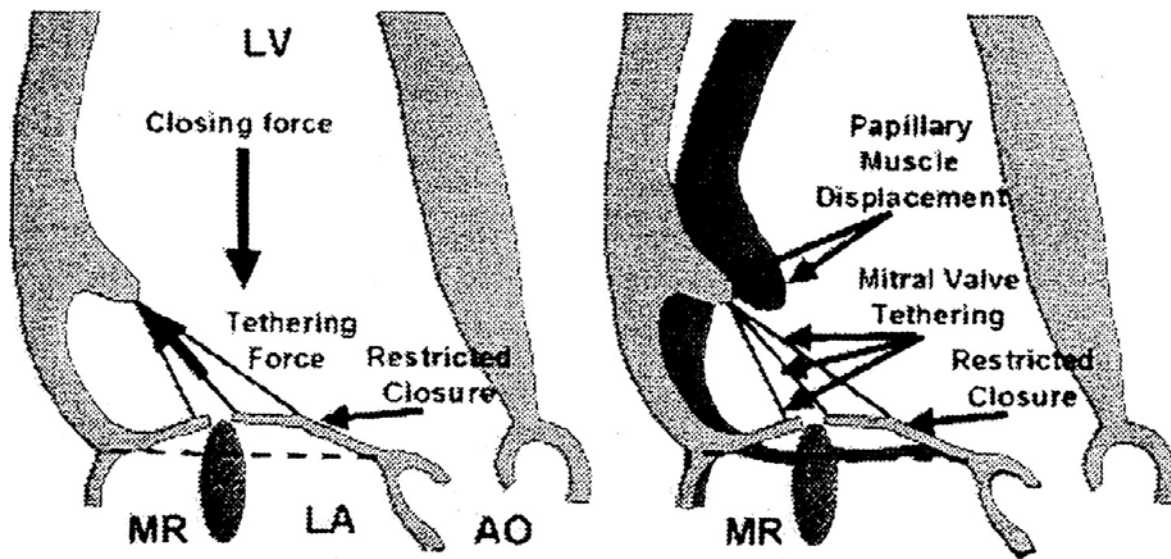


Figure 13. Drawing of balance of forces in mitral apparatus in the left panel. In the right panel, potential effect of papillary muscle displacement to restretch leaflet closure, causing mitral regurgitation. Reproduced from Liel-Cohen N, Guerrero JL, Otsuji Y. Design of a new surgical approach for ventricular remodeling. *Circulation*, 2000; 101: 2756.

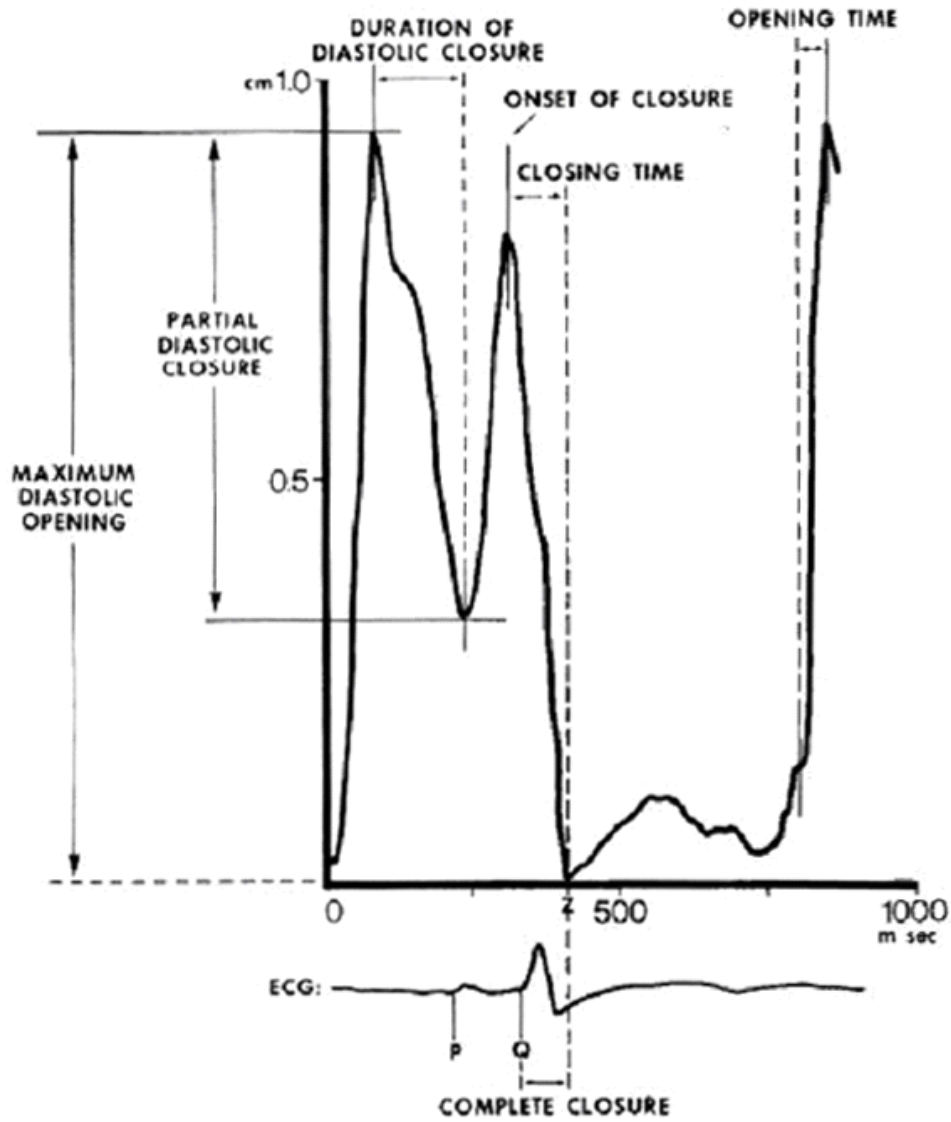
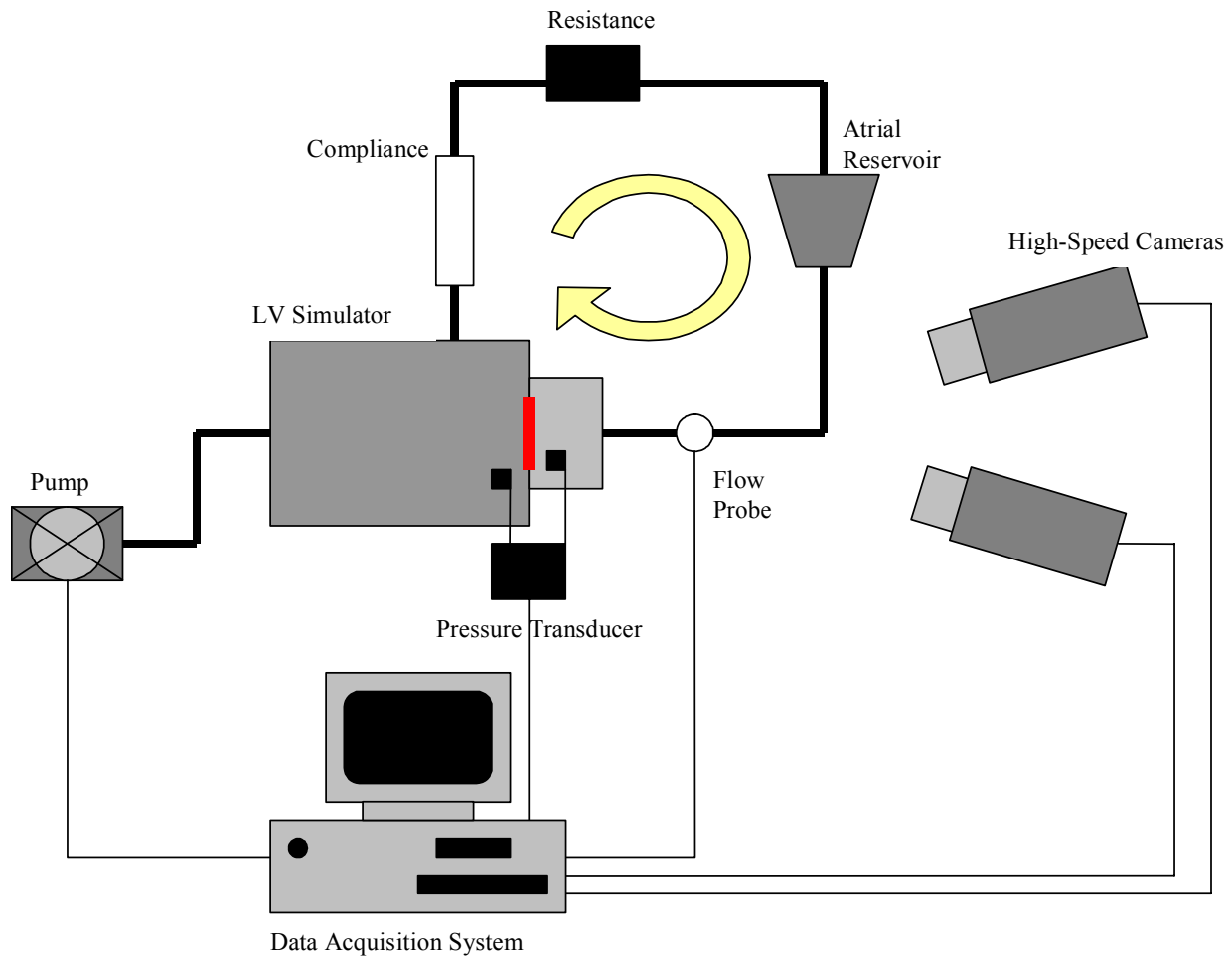


Figure 14. Motion of marker placed on free edge of anterior leaflet. Reproduced from Tsakiris AG, Gordon DA, Mathieu Y, et al: Motion of both mitral valve leaflets: a cineroentgenographic study in intact dogs. *J Appl Physiol* 1975; 39:359.

### **1.7.1 Surface stretches of the anterior leaflet**

A recent study by Sacks et al [32] measured the surface stretches of the anterior leaflet under physiologic conditions by tracking graphite markers glued onto the surface of the valve leaflet in a left-heart simulating flow loop (Figure 15). This study made use of two high speed digital cameras that were both focused on the leaflet, but were oriented at thirty degrees to one another such that 3D spatial coordinates could be determined from the two camera images using a direct linear transform method. [33]. The results of this analysis confirmed that the anterior leaflet opened in approximately 70 milliseconds and closed in approximately 40 milliseconds, and additionally confirmed that the leaflet deformation occurred faster during opening than they did in closure.

In this study, the authors were able to quantify the surface stretches (Figure 16) as well as the surface stretch rates of the anterior leaflet (Figure 17). Additionally, this study showed that after valve closure, the leaflet stretch state remained constant while the valve was held closed for approximately 0.3 seconds during systole, before finally returning to its original configuration as the valve opened. The surface stretches observed by Sacks et al in vitro were confirmed in vivo in an unpublished study by Sacks et al in which sonomicrometry crystals were tracked on the MV leaflets of living sheep (Figures. 16, 17).



**Figure 15. Left-heart simulating flow loop used by Sacks et al to quantify the surface stretches of the MV anterior leaflet. Reproduced from Sacks et al. Surface stretches in the anterior leaflet of the functioning mitral valve.**

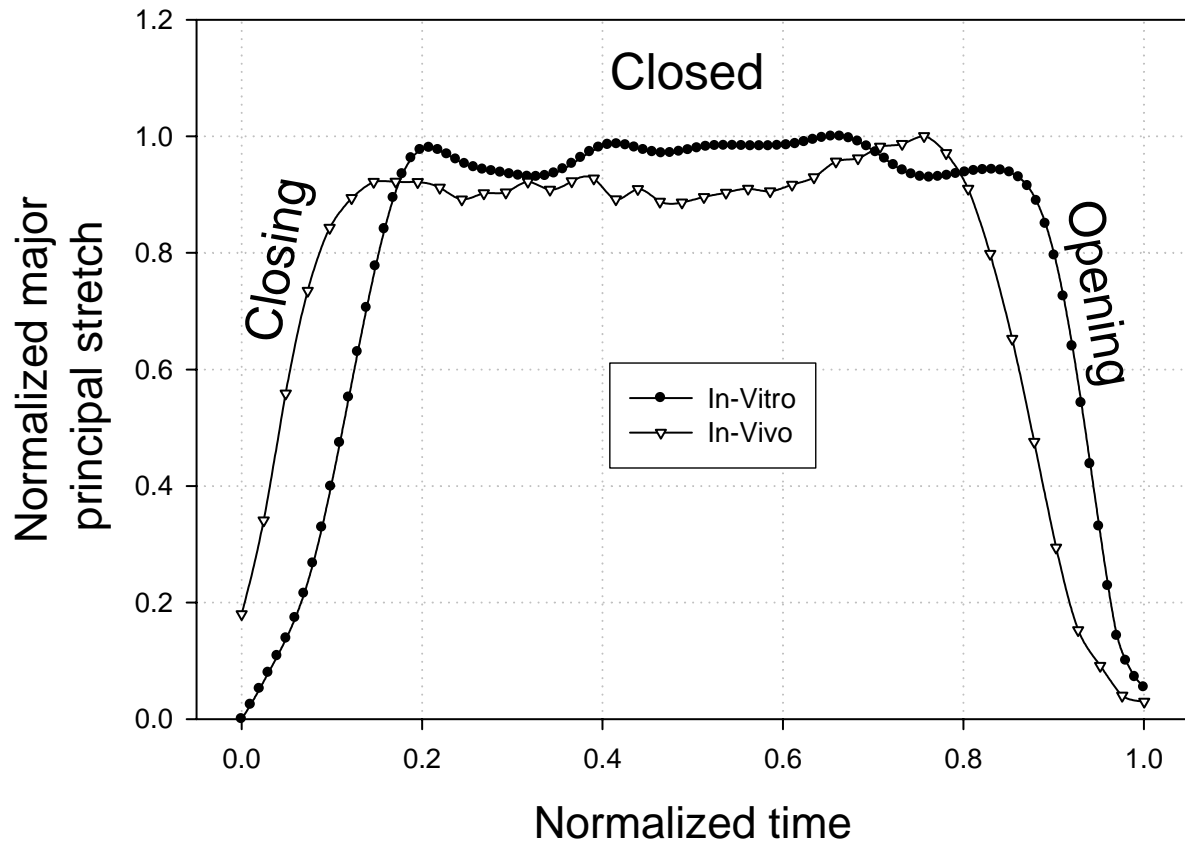


**Figure 16. Principle stretches observed in left heart-simulating flow loop (closed symbols) and in vivo using sonomicrometry method (open symbols). Reproduced from Sacks MS et al. In-vivo dynamic deformation of the mitral valve leaflet. Annals of Thoracic Surgery. Submitted 2005.**

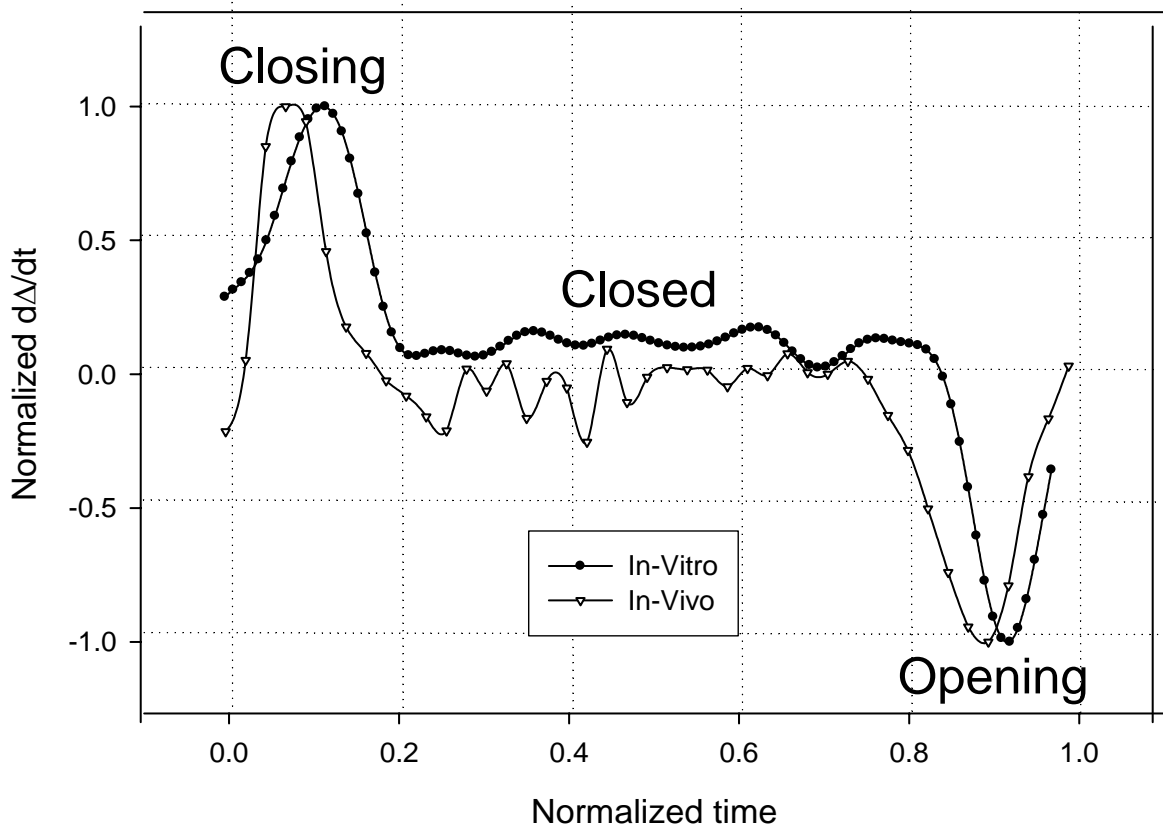


**Figure 17. Principle stretch rates versus time for the MV anterior leaflet under normal physiologic conditions. Reproduced from Sacks MS et al. In-vivo dynamic deformation of the mitral valve leaflet. Annals of Thoracic Surgery. Submitted 2005.**

## 1.8 MECHANICAL PROPERTIES OF MITRAL VALVE LEAFLETS

May-Newman and Yin measured the mechanical properties of the MV leaflets in response to a series of different biaxial leaflet stretch states [34]. In this study, MV leaflets were mounted in a biaxial stretching mechanism (Figure 18) using a series of suture loops on 3 of the four leaflet edges and directly tethering the leaflet chordae tendineae on the final edge. In this study, cyclic stretching was applied with displacement ramp times of 10 seconds corresponding to stretch rates of 4-12% per second.

Results of this study showed that the mechanical properties of the valve leaflets were highly anisotropic with the circumferential axis much less distensible than the radial axis. Additionally this study revealed that the mechanical behavior each specimen axis was highly dependent on the stretch state of the alternate specimen axis (Figure 19). The stress-stretch responses of both specimen axes were found to be highly nonlinear. The authors of this study attributed this nonlinear behavior to the stretch dependent recruitment of collagen fibers.

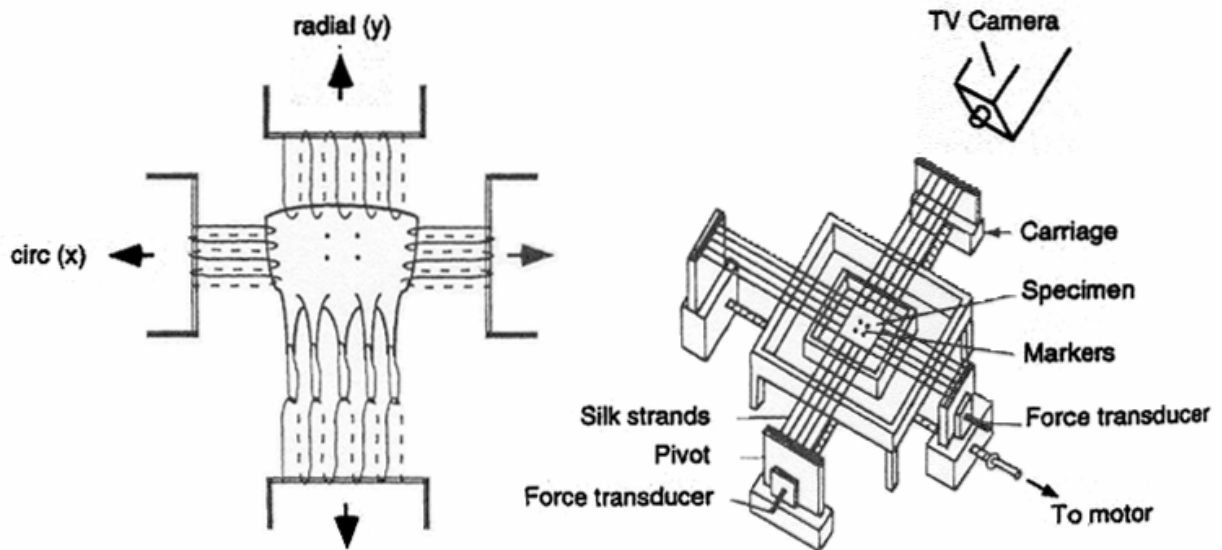


**Figure 18. Experimental setup for biaxial mechanical testing of the MV leaflet. Reproduced from May-Newman and Yin. Biaxial Mechanical Properties of the Mitral Valve leaflets. American Journal of Physiology, 1995.**

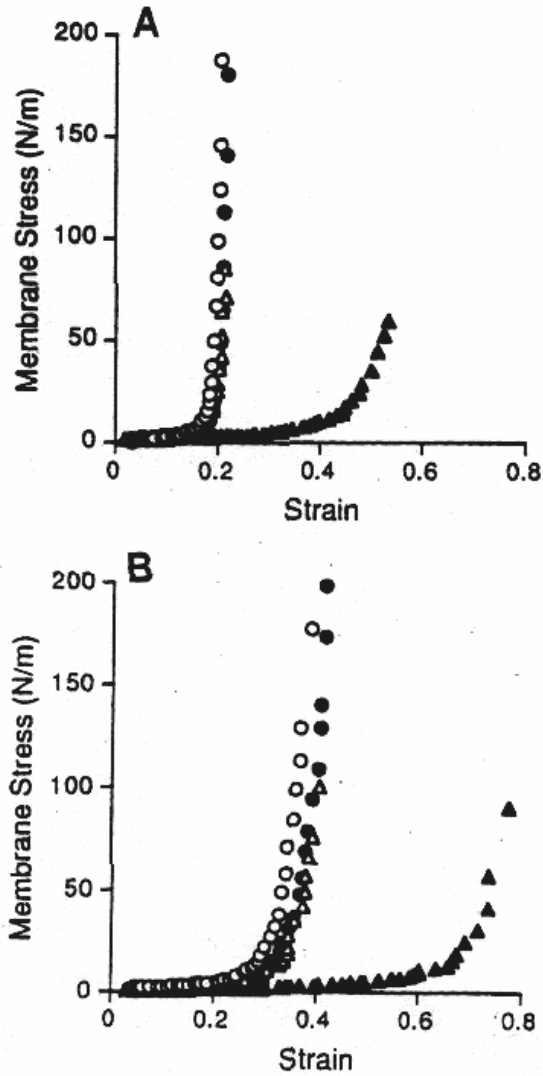
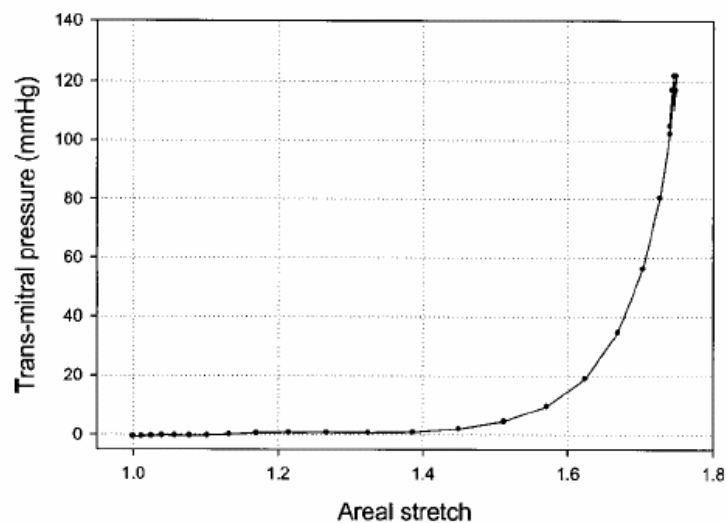


Figure 19. Membrane stress-stretch relations from porcine anterior (A) and posterior (B) leaflets comparing equibiaxial (open symbols) and strip biaxial (filled symbols) protocols. Circles, circumferential axis; triangles, radial axis. Reproduced from May-Newman and Yin. Biaxial Mechanical Properties of the Mitral Valve leaflets. *American Journal of Physiology*, 1995.

The nonlinear behavior measured in the quasi-static biaxial testing was similar to the nonlinear pressure-areal stretch relationship observed by Sacks et al in their left heart-simulating flow loop (Figure 20). In the May-Newman study, differences in the loading and unloading stress-stretch curves were observed, though no attempt was made to quantify this behavior. In addition to the 10 displacements, a select number of specimens were tested at higher stretch rates, up to 40% per second for comparison. The mechanical properties of these specimens were not found to be different from the specimens tested at the slower speeds.



**Figure 20. Pressure - areal stretch relationship of the MV anterior leaflet measured in left heart-simulating flow loop. Reproduced from Sacks et al. Surface stretches in the anterior leaflet of the functioning mitral valve.**

This characteristic nonlinear stress-stretch response has been observed for other valvular materials as well. In their study on the biaxial mechanical properties of the aortic valve cusp, Billiar and Sacks [35] reported similar nonlinearity, anisotropy and mechanical coupling (Figure 21).

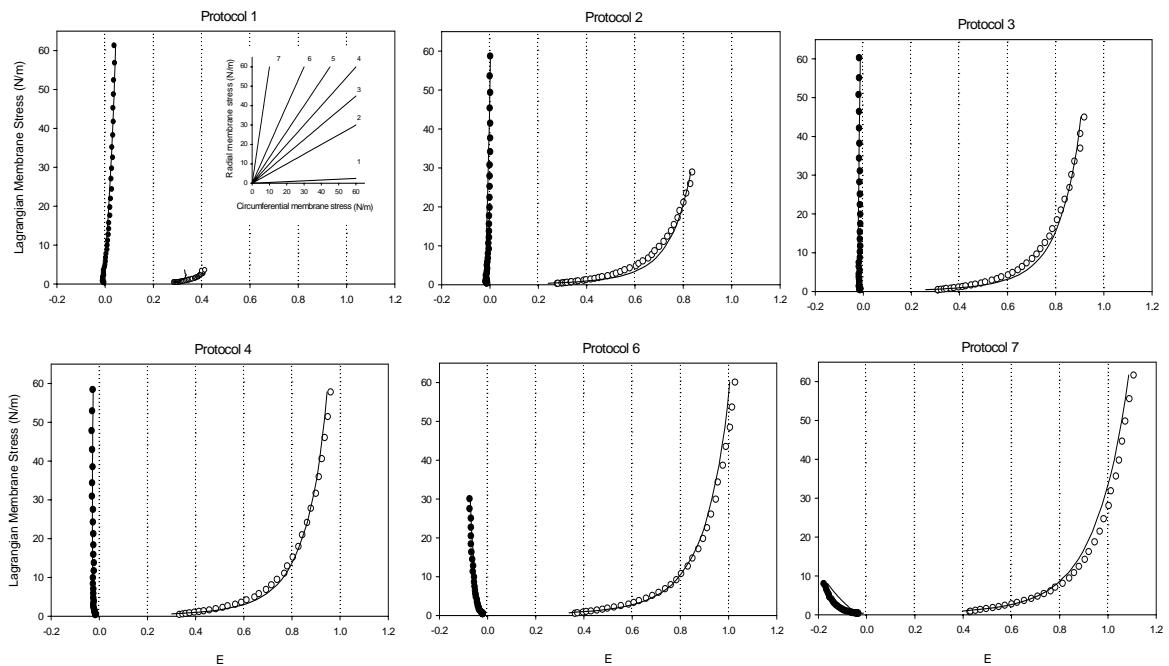


**Figure 21. (a) The seven loading protocols used to characterize the biaxial stress-stretch response, and (b) response to all loading protocols for an AV cusp (open circles), along with the structural model fit, demonstrating an excellent fit.**

## 1.9 VISCOELASTIC BEHAVIOR

The term “viscoelastic” implies that the mechanical properties of such a material are composed of both a time dependent (or viscous) and a time-independent (or elastic) component. Much of the pioneering work on the viscoelasticity of living tissues was done by Fung, who summarized the time dependence of biological tissues: “When a body is suddenly stretched and then the stretch is maintained constant afterward, the corresponding stresses induced in the body decrease with time: this phenomenon is called “stress-relaxation.” If the body is suddenly stressed and then the stress is maintained constant afterward, the body continues to deform: this phenomenon is called “creep.” If the body is subjected to a cyclic loading, the stress-stretch relationship in the loading process is usually somewhat different from that in the unloading process: this phenomenon is called “hysteresis.” These behaviors are all features of a mechanical property called “viscoelasticity.” [36]

On its most basic level, viscoelasticity suggests that the time-dependent mechanical properties of a material are dependent on the deformations to which the particular specimen has been previously subjected; a classification often termed “stretch-history dependence.” Currently, the viscoelastic properties of the MV leaflets remain largely unstudied, mainly due to the complexity of the necessary experimental protocols.

Generally, one of three main theories is used to describe the viscoelastic mechanisms in soft tissues.

1. Time-dependent reorientation of collagen fibers within a viscous matrix.
2. Molecular relaxations within the GAG matrix.
3. Molecular relaxations within the collagen fibers themselves.

The following subsections give information on viscoelastic testing in general.

### **1.9.1 Stress-relaxation testing**

Stress-relaxation experiments (Figure 22) typically include a rapid loading phase to a desired stretch level, after which, the material stretch state is held constant. The maintenance of a constant stretch state has special implications for typical biological materials including the MV leaflet; the lack of change in the stretch state of the material limits the ability of the fibers within a tissue to reorient themselves for the duration of the test. Thus, changes in the specimen loading state required to maintain the constant stretch state can be assumed to be independent of fiber rotations. It should be noted that currently many membranous tissues are subjected to uniaxial “stress-relaxation” tests. These tests, while important in their own right, are not true stress-relaxation experiments since deformations are possible on the free specimen axis.

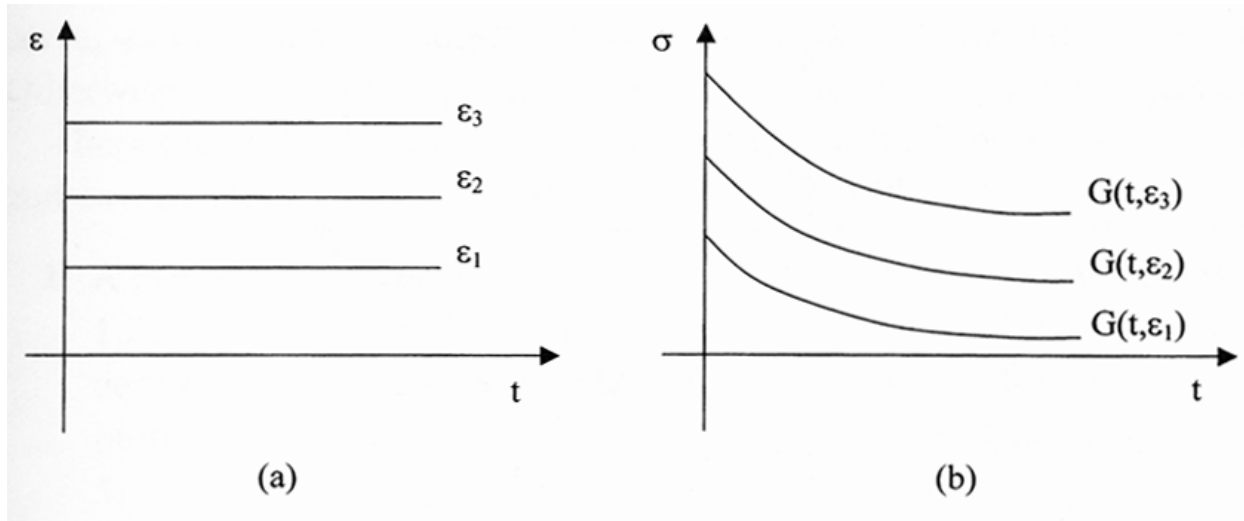


**Figure 22. (b) The stress-relaxation responses to three different stretch histories (a). Reproduced from Wineman AS, Rajagopal KR, Mechanical Response of Polymers. Cambridge University Press. 2000.**

## 1.9.2 Creep testing

In a creep test (Figure 23), a specimen is loaded to a desired load or stress level, then the loading state is maintained for the duration of the test by adjusting the specimen stretch state. In many instances the creep experiment provides more physiologically relevant data for bodily tissues than are provided by the stress-relaxation test since, *in vivo*, most tissues are generally loaded with a certain force rather than stretched to a certain stretch state. One disadvantage of the creep experiment is that, unlike the stress-relaxation case, the fibers within a tissue specimen are free

to rotate and changes in the mechanical properties of the tissue cannot be isolated from the dynamic rearrangements of fibers within the material.

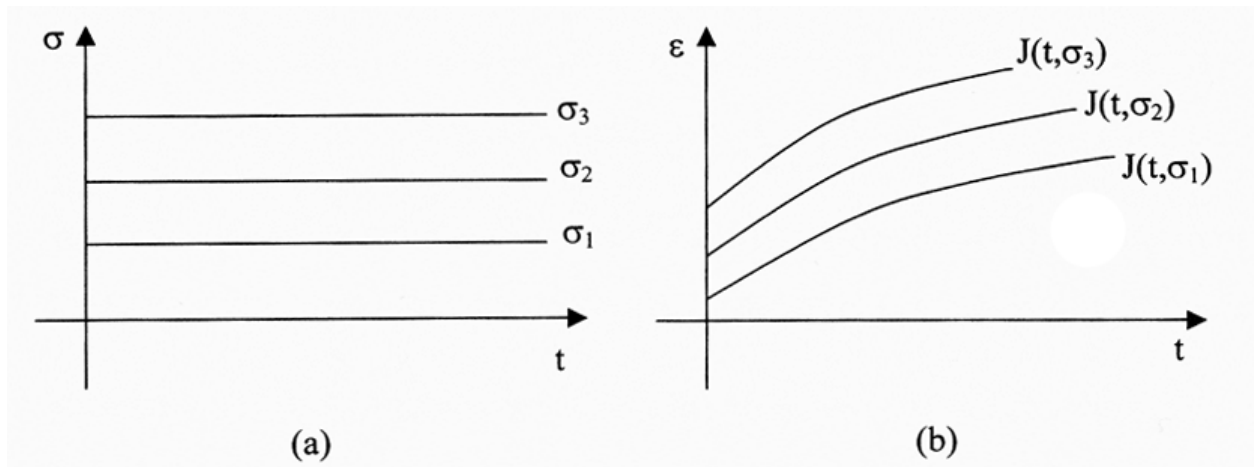


**Figure 23. The creep responses (b) to three different stress histories (a). Reproduced from Wineman AS, Rajagopal KR, Mechanical Response of Polymers. Cambridge University Press. 2000.**

### 1.9.3 Hysteresis

Hysteresis represents the energy lost when a material is loaded. Hysteresis is typically calculated as the ratio of the change in energy between the loading and unloading cycles to the total energy stored in the loading cycle. Energy storage is usually determined by calculating the area beneath the loading versus displacement curves.

### 1.9.4 Modeling viscoelastic behavior - the Boltzmann superposition principle

The superposition principle, developed by Boltzmann, states that the total stretch response of a material to the application of individual stress histories is the sum of the effect of applying each stress separately. In the one-dimensional case, we may consider a simple bar subjected to a force  $F(t)$  and elongation  $u(t)$ . The elongation  $u(t)$  is caused by the total stress history before the current time,  $t$ . If the function  $F(t)$  is continuous and differentiable, then in a small time interval  $d\tau$  at time  $\tau$  the increment of loading is  $(dF/d\tau)d\tau$ . This increment acts on the bar and contributes an element  $du(t)$  to the elongation at time  $t$ , with a proportionality constant  $c$ :

$$du(t) = c(t - \tau) \frac{dF(\tau)}{d\tau} d\tau \quad (1)$$

If the origin of time corresponds with the beginning of motion and loading, then, by the contributions of all loading for all time, we obtain:

$$u(t) = \int_0^t c(t - \tau) \frac{dF(\tau)}{d\tau} d\tau \quad (2)$$

A similar argument, with the role of  $F$  and  $u$  interchanged, gives

$$F(t) = \int_0^t k(t-\tau) \frac{du(\tau)}{d\tau} d\tau \quad (3)$$

These laws are linear. Scaling the load by a given factor causes the elongation to be scaled by the identical amount, and vice versa. The functions  $c(t-\tau)$  and  $k(t-\tau)$  are the creep and relaxation functions, respectively. The application of the Boltzmann principle of superposition allows the use of a limited amount of experimental data, from both static and time dependent experiments, to predict the mechanical response of a tissue to a wide number of loading conditions.

### **1.9.5 Modelling viscoelastic behavior - quasilinear viscoelasticity**

In order to adequately model the viscoelastic properties of soft tissues under finite deformations, the non-linear stress-stretch characteristics of the tissue must be considered [37]. For this reason Fung has developed a theory known as quasi-linear viscoelasticity (QLV) in which the relaxation function,  $K(\epsilon, t)$ , is dependent on time (as in the linear viscoelasticity formulation) as well as stretch level. This theory is termed “quasi-linear” because the relaxation function may be separated into a reduced relaxation function,  $G(t)$  that is a function of time only and an elastic response,  $\sigma(e)(\epsilon)$  that is a function of stretch only.

$$K(\varepsilon, t) = G(t)\sigma^{(e)}(\varepsilon) \quad (4)$$

In this formulation, the generalized form of  $G(t)$  proposed by Fung is given by:

$$G(t) = \frac{1 + \int_0^\infty S(\tau)e^{-\frac{t}{\tau}}d\tau}{1 + \int_0^\infty S(\tau)d\tau} \quad (5)$$

where  $S(\tau)$  is defined based on the stress response of the material to be modeled. Experimental evidence has shown that the relaxation of soft tissues tends to decrease with time. This behavior can be modeled simply using the following formulation:

$$S(t) = \frac{c}{\tau} \quad (6)$$

for  $\tau_1 \leq t \leq \tau_2$  where  $c$  is the magnitude of relaxation,  $\tau_1$  is the short time constant and  $\tau_2$  is the long time constant.

QLV has been used previously to model many soft tissues such as ligament [38], bladder [39] and valvular materials [40] to name just a few. QLV analysis is very attractive because the QLV formulation is formed from continuous functions and the viscoelastic behavior may be described using only three physically meaningful mathematical parameters.

### **1.9.6 Stretch rate sensitivity in soft tissues**

The hypothesis that the mechanical properties of the MV anterior leaflet may be sensitive to stretch-rate, necessitating the need to define the mechanical properties of the valve under physiologic stretch rates, is based on several observations of the stretch rate sensitivity of the MV leaflet and other soft tissues throughout the biomechanical literature. The dynamic viscoelasticity of the MVAL was investigated by Lim et al. [41] who measured the bulge height of the MV leaflet in response to sinusoidal pressure gradients applied at frequencies varying from 0.5 to 5.0 Hz. Their results suggested that the mechanical properties of the valve were dependent on stressing frequency. This finding was supported by a study by Leeson-Deitrich et al. [42] who used a uniaxial tension testing mechanism to test porcine pulmonary and aortic valve leaflet strips and reported that the average leaflet stiffness increased with stretch rate.

Results for other soft tissues have revealed varying behaviors among different tissues. Naimark et al. [43] explored the effects of uniaxial loading rate on mammalian pericardia and showed that the stress-stretch relationship for pericardia was not dependent on stretch rate. Woo et al. [38] found that the stress-stretch relationship for the canine medial collateral ligament was only slightly affected by stretch rate while a study by Lydon et al. [44] measured the affects of elongation rate on the rabbit anterior cruciate ligament and found that the stress-stretch response of the ligament was highly dependent on elongation rate. Haut and Little [45] explored the effects of stretch rates on rat tail tendon and observed that the stiffness of the tendon was affected slightly by stretch rate, but that the failure stretch increased dramatically with stretch rate.

Additional studies have explored the effects of loading rate on biologically derived valvular materials, again with varying results. Lee et al. [46] performed uniaxial experiments on glutaraldehyde-stabilized porcine aortic valve leaflet strips and found that the stress-stretch relationship was dependent on stretch rate in the circumferential direction and independent of stretch rate in the radial direction.

Overall, the stretch rate sensitivity of soft tissues appears to be highly tissue specific and dependent on the specific experimental protocol. The variation in the findings of these studies underscores the necessity for characterization of the MV leaflet mechanical properties under the physiologic condition.

### **1.9.7 Creep and stress-relaxation in soft tissues**

In addition to the stretch rate sensitivity, the creep and relaxation aspects of MV leaflet mechanical behavior remain to be explored. These tests are particularly relevant to the 300 millisecond constant stretch phase observed in the leaflet surface during valve closure.

Of particular relevance to this study is a recent study by Liao and Vesely [40], in which uniaxial stress relaxation experiments were performed on the porcine MV chordae tendineae. This study reported relaxation percentages between 30% and 60% after 100 seconds and went on to link the amount and rate of relaxation to the glycosaminoglycan (GAG) content of the individual chordae. Although the investigations into the stress-relaxation and creep response of the MV leaflets are non-existent to the author's knowledge, the creep and relaxation literature for soft tissues reveals some interesting behaviors that should be investigated in the MV.

Provenzano et al [47] explored the relaxation and creep behavior of the rat medial collateral ligament (MCL) and found that the rate of relaxation was nonlinearly inversely proportional to the stretch level and that the rate of creep was nonlinearly directly proportional to the applied stress. Dunn and Silver [48] showed that the amounts of relaxation in aorta, skin, tendon, dura matter and pericardium were all dependent on stretch level. In contrast to these two studies, Lee et al [46] found that the percentage of stress remaining in glutaraldehyde-stabilized porcine aortic valve strips after a 1000 second uniaxial stress-relaxation test was independent of initial load. In their study of the rabbit MCL, Thornton et al observed an imbalance between stress-relaxation and creep rates of MCL specimens initially loaded to the same level [49]. To quantify their results, Thornton et al fit the MCL relaxation data with a quasilinear viscoelastic (QLV) model and used this model to predict the MCL creep behavior. A comparison to the actual creep data showed that the QLV formulation predicted much higher creep percentages than those actually observed (150% predicted versus 115% observed). These findings were supported by the findings of the previously mentioned study by Provenzano et al [47] in which the rate of stress-relaxation proceeded approximately two times faster than the creep rate in the rat MCL when contralateral ligaments were tested simultaneously. Vesely et al [50] expanded on these findings by showing that the stress-relaxation behavior of porcine aortic valve cusps was highly dependent on the initial rise time. As seen in the stretch rate sensitivity literature, it is clear that the creep and relaxation responses in different studies are highly tissue specific. Additionally, the experimental factors such as initial rise time, initial stretch/load level and test duration heavily influence the results.

## 1.10 MOTIVATION FOR THE CURRENT STUDY & STUDY AIMS

The ultimate goal for any MV repair or replacement is to permanently reproduce the functional properties of the native valve. Studying the mechanical properties of the native valve will provide the necessary data for the qualification of suitable prosthetic materials. Additionally, an in-depth understanding of the relationship between the valvular function, macrostructure, and microstructure may provide motivation for the progression of novel repair techniques as well as the development of suitable tissue-engineered replacement materials. The primary objective of any biomechanical study should be to first describe the functional properties of the valve. The investigation of biomaterial behavior under non-physiologic conditions does supply useful information and may provide insight into the inner workings of a given material, but this information is of much greater value when it complements a complete understanding of the physiologically relevant material properties.

In the case of the MV, the valve leaflet is a thin and nearly incompressible membrane. Therefore, planar biaxial testing can be used to quantitatively characterize its mechanical properties [51]. In the work by May-Newman and Yin discussed previously [34], quasi-static (stretch rates of 4% to 12 %/second) biaxial experiments were performed on the MV leaflets. This work provided biomechanical data by subjecting MV leaflet specimens to a range of biaxial stretch-based protocols and this data was later used to develop a stretch energy-based constitutive model for a generalized loading state [52]. This study provided a valuable data, but was performed before a complete understanding of MV surface stretches was available. The recent study by Sacks et al [32], in which the surface stretches of the leaflet were measured in a left heart-simulating flow loop, showed that the stretch rates of the MV anterior leaflet were on

the order of 1000% per second, more than an order of magnitude greater than the maximum stretch rates employed in the May-Newman study. In addition to the stretch rate analysis, the study by Sacks and colleagues reported the stretch states of the leaflet under physiological conditions, thus providing the necessary data to reasonably replicate the in vivo loading condition of the valve leaflet under controlled conditions in a biaxial stretching mechanism. It is critical to determine if previously reported quasi-static biomechanical data can be used to model the behavior of the valve in the physiological condition, since the application of any such model (i.e. to optimize MV repair or replacement techniques) would be used to predict behavior under physiological conditions.

### **1.10.1 Specific study aims**

The goal of this work was to expand on previous studies by quantifying the biaxial viscoelastic properties of the MV anterior leaflet under physiological conditions. Specific aims were:

1. To develop a biaxial testing device capable of testing MV leaflet specimens under physiologic stretch and loading conditions at physiological stretch rates.
2. To determine the stretch rate sensitivity of the MV anterior leaflet when loaded to physiologic stretch levels at stretch rates ranging from quasi-static to physiological.
3. To determine the stress-relaxation and creep responses of the MV anterior leaflet at a physiologic stretch or loading state with physiologic initial rise times.

## 2.0 METHODS

### 2.1 HIGH-SPEED BIAXIAL TESTING DEVICE

#### 2.1.1 Device specifications

The following section describes the factors taken into account in the design of the high-speed biaxial testing device. These specifications were deemed to be those necessary to adequately represent the physiological properties of the MV leaflet.

**2.1.1.1 Displacements and displacement rates.** In order to adequately reproduce the stretch rates experienced by the MVAL in vivo, the necessary displacements and displacement rates for the actuation components were determined based on the in vitro findings of Sacks et al in their left heart-simulating flow loop [32]. In this study, the mean circumferential and radial stretches were 1.11 and 1.33 respectively (refer to INTRODUCTION as necessary). To calculate the maximum stretches for the device requirements, the standard deviations of the circumferential and radial stretches, 0.07 and 0.16 respectively, were multiplied by three and added to the mean values. This stretch range was chosen in order to encompass 99% of the MVAL specimens. The specification for the maximum specimen stretches calculated in this manner were 1.31 (circumferential) and 1.80 (radial). To translate the maximum stretches into displacements, they

were multiplied by the appropriate maximum expected specimen dimension. Maximum specimen dimensions were estimated to be 3 cm x 3cm based on previous experience. These dimensions resulted in maximum displacements of 0.93 cm (circumferential) and 2.40 cm (radial). These displacements were divided by two to account for the fact that each specimen axis would be stretched by two actuators (one on each free edge) for maximum displacements of 0.47 cm (circumferential) and 1.20 cm (radial) per actuator.

Using the calculated displacements, the maximum necessary displacement rates were calculated by dividing the necessary displacements by the shortest required loading time. The in vitro data showed the physiological opening and closing times to be approximately 0.07 seconds, so the shortest desired loading time was chosen to be 0.05 seconds to provide sub-physiological loading rates. This resulted in maximum required displacement rates of 0.093 m/s (circumferential) and 0.24 m/s (radial) per actuator. These displacement rates were then multiplied by a safety factor of 2 in order to account for the influence of edge effects on the overall loading. This provided a final displacement rate specification of 0.19 m/s (circumferential) and 0.48 m/s (radial) for each actuator.

2.1.1.2 **Maximum loads.** The maximum loads on the device carriages were calculated by estimating the membrane tension,  $T$  (defined as the load per unit length over which it is applied), on the leaflet under physiological conditions. Assuming the valve was roughly spherical with a radius of 10 mm when loaded, the Law of Laplace was used to calculate  $T$ :

$$T = \frac{PR}{2} \tag{7}$$

where  $P$  is the transvalvular pressure and  $R$  is the radius. Substituting a transvalvular pressure value of 120 mmHg [3] into this equation yielded a  $T=79.99$  N/m. It was preferable for this estimate to slightly overestimate the physiological condition because this would make it more likely that the physiologic condition would be included in the load range, so this estimate was rounded up to 90 N/m (+10%). This peak membrane tension level was converted to axial load by multiplying by the largest expected specimen dimension (3 cm). This yielded a peak load value of 2.7 N. This was converted to grams by multiplying by unit conversion factor of 101.97 g/N to yield peak loads in grams of 275.32. Because the stretch rate sensitivity of the MV tissue was unknown at this point in the design process, this value was rounded up to 1000g to account for any stretch rate sensitivity in the stress response of the leaflets.

**2.1.1.3 Stretch & load measurement frequency.** Using the 0.05 second minimum loading/unloading time, the maximum necessary stretch and load measurement frequencies were calculated by dividing the minimum number of data points desired by the 0.05 second duration. The minimum number of desired data points was estimated at 25. Approximating the stretch response of the MV leaflet to be roughly linear with respect to time during loading and unloading (see INTRODUCTION), 25 data points would allow a maximum stretch step of 0.032 between image acquisitions. Dividing 25 by the 0.05 second minimum loading duration yielded a necessary stretch measurement frequency of 500 Hz.

The load frequency was calculated by multiplying the stretch acquisition frequency by 10. This was done to allow each load data point to represent the average of 10 load acquisitions.

This technique was employed successfully on the previous biaxial testing device to reduce noise levels in the load signal.

## 2.1.2 Device design

The following section describes the specific components used in the design of the testing apparatus in order to meet the design specifications provided in the previous section.

### 2.1.2.1 Device overview

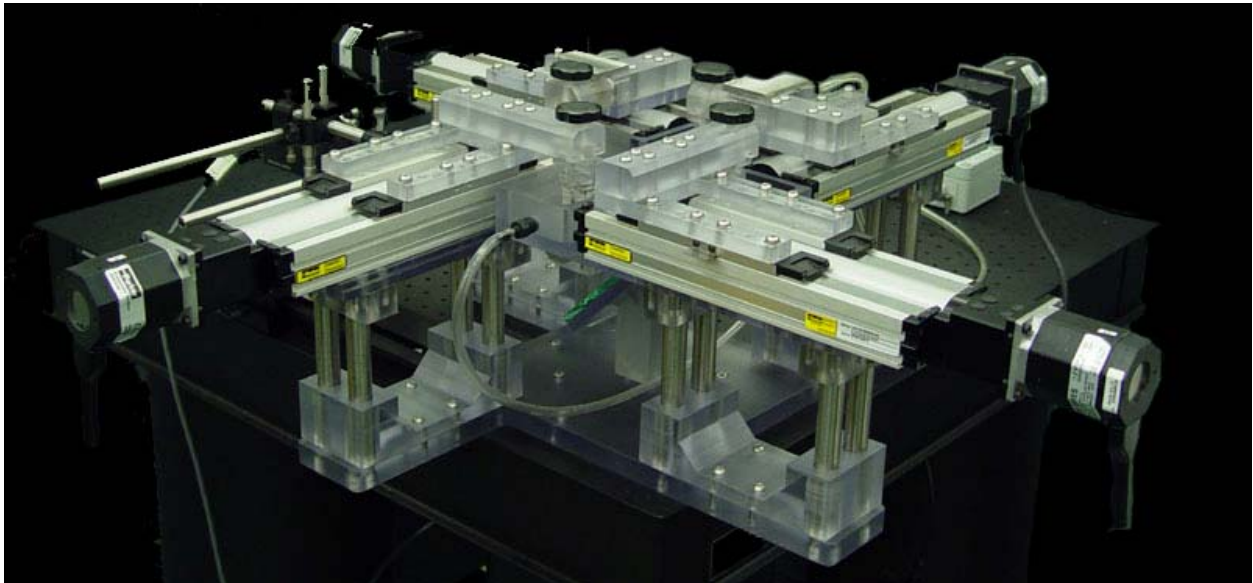


**Figure 24.** The high-speed biaxial testing device mounted on a vibration isolation table.

The high-speed biaxial testing device (Figures 24, 25) consisted of four linear positioners, each driven by a stepper motor. The positioners were arranged around a central specimen bath, with each specimen carriage arm reaching into the bath from a direction orthogonal to its axis of travel. The positioners and bath were mounted on a custom-designed support fixture that was built to be mounted on a vibration isolation tabletop. This fixture raised the bath and positioners 6" above the tabletop so that the specimens could be imaged from below using a 45° mirror configuration. Cameras were mounted separately on a single camera stand that allowed precise, spatial adjustments on 3 axes. In addition to holding the specimen and fluid, the bath had inflow and outflow tubing connectors that allowed the bath fluid to be pumped into a heat exchanger so that fluid temperatures could be maintained at physiologic levels. The device was controlled with a dual computer system (Figure 26), with one computer designated for high-speed imaging.

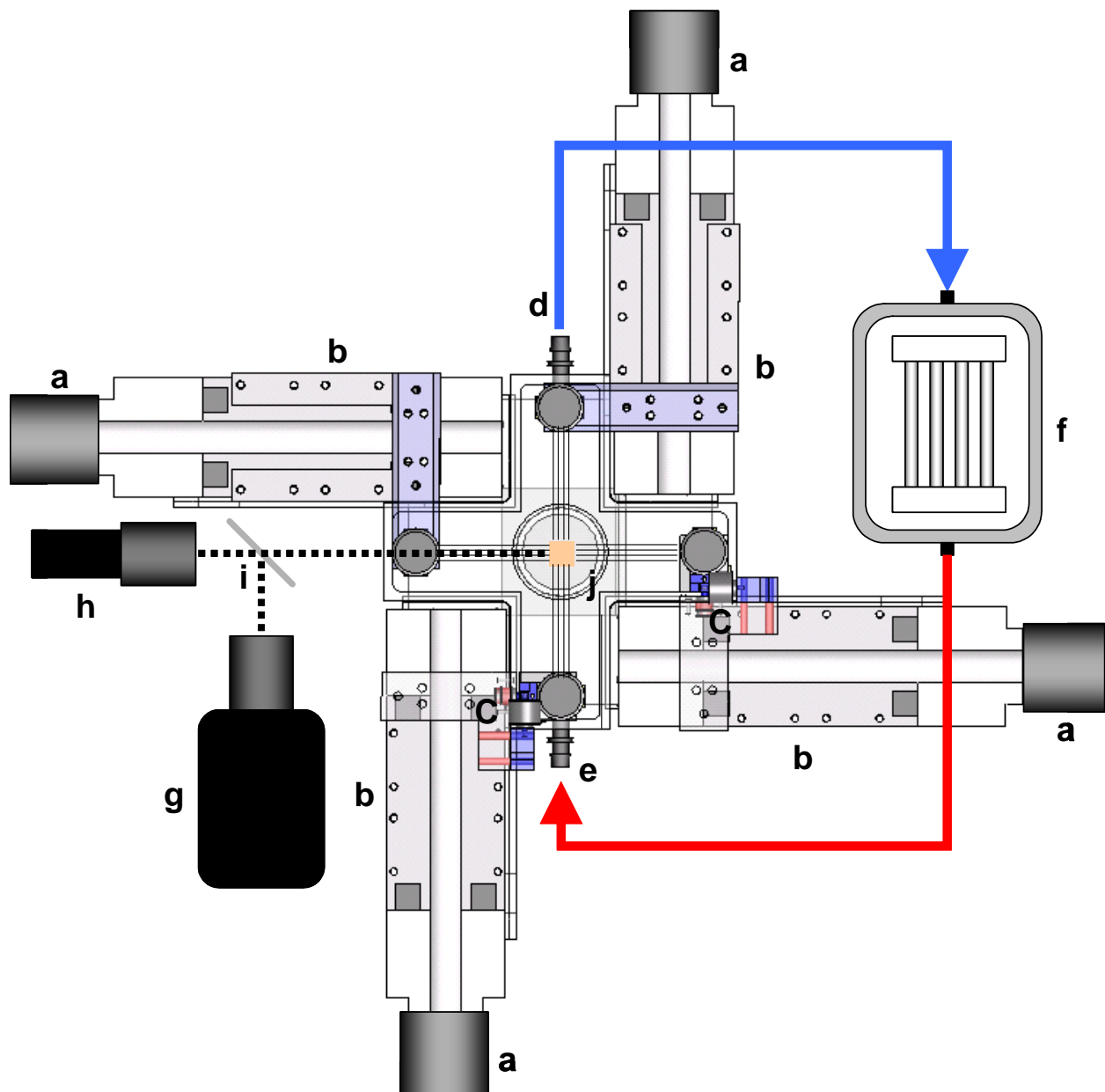


Figure 25. Overhead schematic of the high speed biaxial testing device; a) stepper motors; b) screw-driven linear actuators; c) load cells; d) specimen bath outlet; e) specimen bath inlet; f) heating element maintained bath temperature at 37°C; g) high speed digital camera; h) standard digital camera; i) beam splitter; j) sub specimen mirror.

2.1.2.2 **Actuation components.** The new biaxial stretching device was designed to meet the displacement requirements while accelerating smoothly and stopping precisely in order to prevent overstretching and to minimize excessive vibrations associated with rapid accelerations and decelerations that could potentially result in specimen damage and generally decrease the levels of test repeatability and validity.

To accomplish this, four ball-screw driven linear positioners (404XR, Parker Hannafin Corp., Irwin, PA), each equipped with a 20mm lead capable of achieving a maximum carriage velocity of 1 m/s and maximum carriage acceleration of 25 m/s<sup>2</sup> were mounted in an opposing fashion such that one pair of positioners was aligned to stretch a centered tissue sample along one device axis and a second pair of positioners was aligned, with orientation orthogonal to the first pair, to stretch the sample along the second device axis. These linear positioners were coupled with rotary stepper motors (OS22B-SNL10, Parker Hannafin Corp., Irwin, PA). Each stepper motor was driven with a microstepping drive (E-AC, Parker Hannafin Corp., Irwin, PA) that provided a step resolution of 50,800 steps per revolution, which, when coupled to each aforementioned linear positioner resulted in a spatial resolution of approximately 0.394  $\mu\text{m}$  for each positioner carriage. All stepper motors were controlled via a 4-axis PCI motion controller card (DMC 1840, Galil Motion Control Inc., Rocklin, CA) that was installed in the device control PC (Precision 550, Dell Inc., Round Rock, TX) (Figure 26).

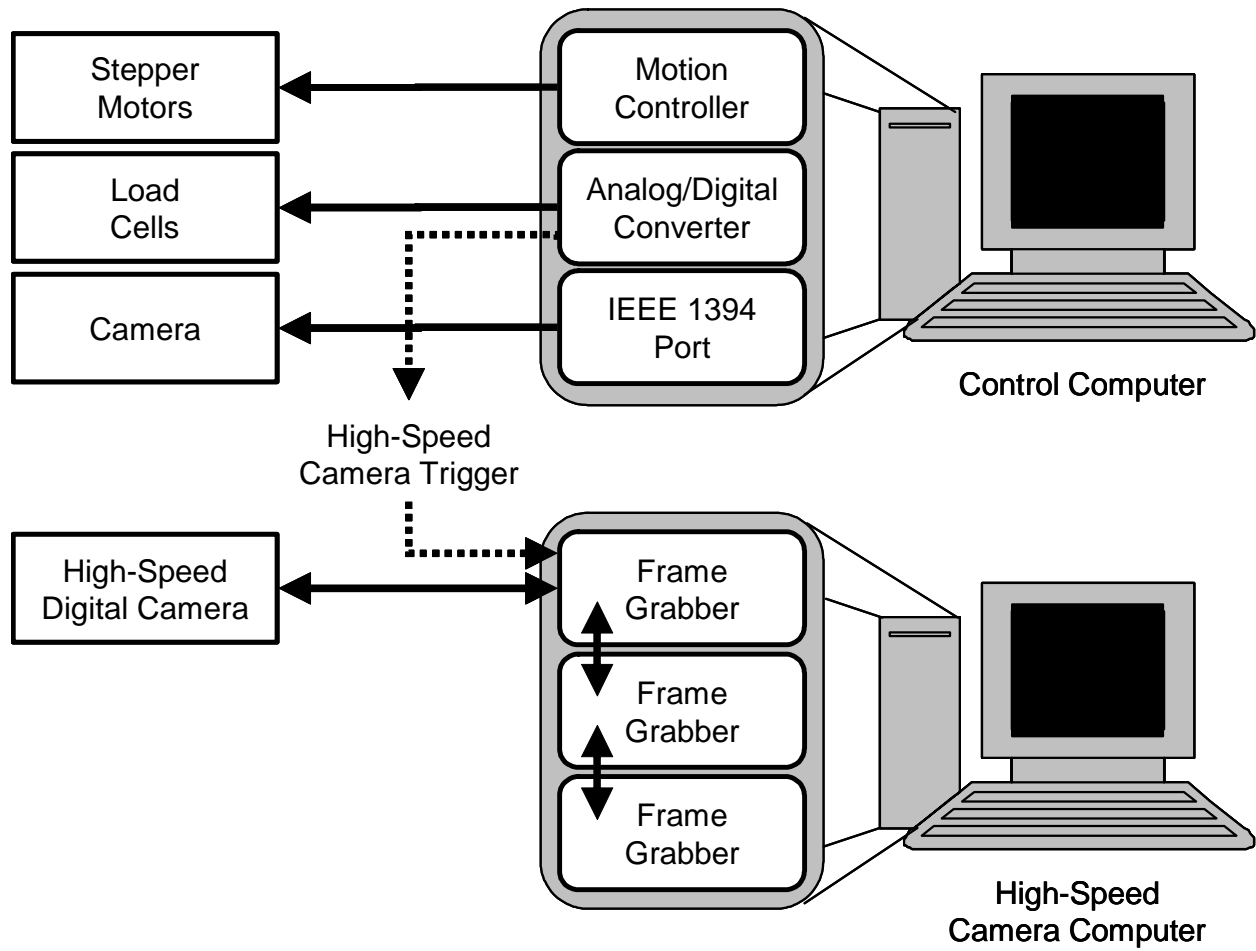
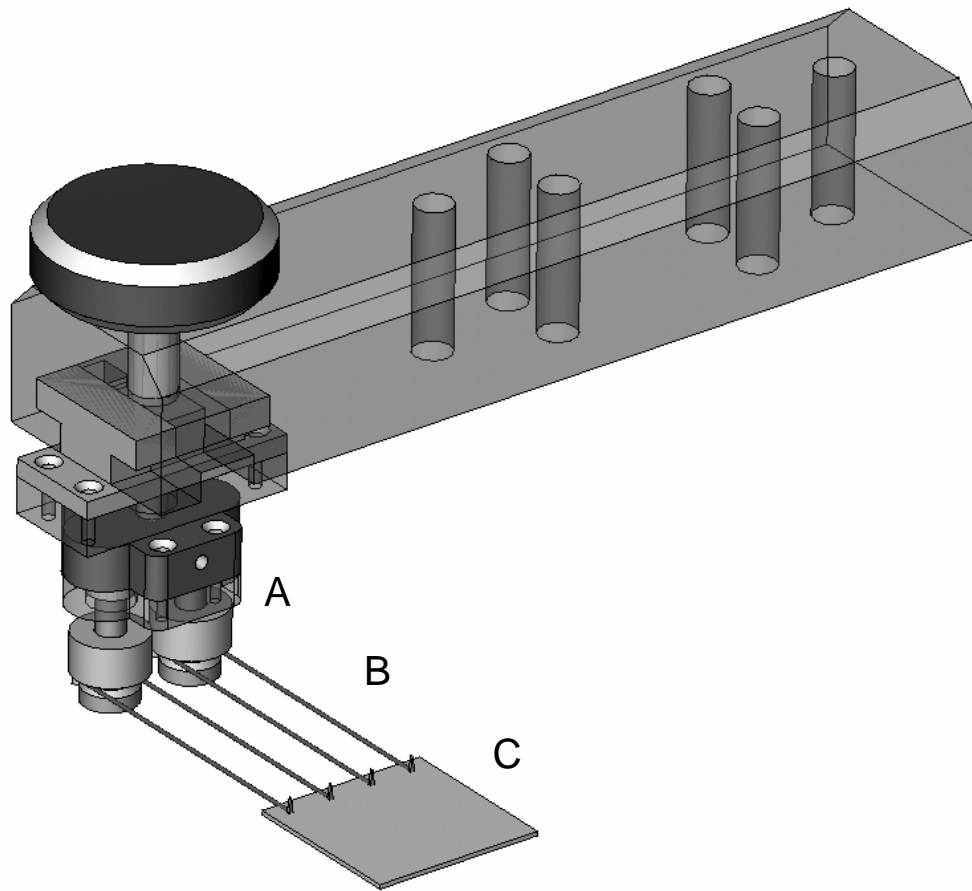


Figure 26. Two computers used to control the biaxial testing device.

2.1.2.3 **Specimen attachments.** Custom attachment arms (Figure 27) were mounted onto the carriage of each linear positioner in order to provide a mechanism for specimen attachment. Leaflet specimens were mounted to these attachment arms in a trampoline fashion by attaching two loops of 000 nylon suture to each side of the specimen via four stainless steel surgical staples. The attachment arms were designed to fasten the two specimen suture loops and to transmit the total load applied by each actuator evenly through all of the attached suture lines. To accomplish this, each attachment arm was furnished with a pair of custom stainless steel pulleys which were free to rotate, ensuring that the forces applied through each pulley were balanced between both of the surgical staple attachments for the attached suture loop. Both pulleys were mounted symmetrically on either side of a central stainless steel ball bearing. This mechanism distributed the total force applied by the positioner equally between both pulleys. This attachment mechanism was based on the previously reported suture attachment pulley system, but improved on that mechanism by ensuring that the orientation of each suture line was aligned with the specimen plane.



**Figure 27. A CAD model of one suture attachment arm. (A) Custom suture attachments were designed to balance the force applied by each carriage through all four suture lines. (B) Specimens were mounted to these attachment arms in a trampoline fashion by attaching two loops of 000 nylon suture to each side of the specimen via four stainless steel surgical staples. (C) Specimen.**

**2.1.2.4 Specimen bath.** The cross-shaped specimen bath (Figure 28) was designed to allow room for the carriage arm/specimen attachment travel required to achieve the necessary specimen displacements. The cross shape was used because it minimized the volume of the bath while still allowing adequate travel lanes for the portions of the specimen attachments that reached into the bath. The central portion of the bath base contained a custom acrylic specimen viewing window. Unlike the rest of the bath, this window was highly polished, allowing a clear image to be taken from beneath the bath. The window doubled as a specimen stand. This stand supported the specimen so that it did not move vertically when the applied membrane tensions were not high enough to keep the specimen perfectly taut. The original prototype specimen window was thin and level with the bottom of the bath, but it was discovered in testing that small vertical specimen motions could cause problems with image focus and could introduce some stretch measurement error since, from the camera viewpoint, the markers appeared to move apart as the specimen moved closer to the camera, thus increasing the size of the specimen in the camera image.

**2.1.2.5 Stretch and load measurement.** Leaflet deformations were measured optically with a dual camera digital imaging system (Figure 29). The first camera (XCD-X700, Sony, Tokyo, Japan) acquired images with a pixel resolution of 1024 x 768 at an acquisition rate of 15 frames per second. These images were stored in the device computer memory in real-time via a Firewire (IEEE 1394) port and were used for control purposes during quasi-static preloading cycles and to acquire data in the later portions of stress-relaxation and creep experiments. During high-speed cycles and the initial loading phases of stress-relaxation and creep experiments an auxiliary high-speed digital imaging system (FastCamera 13, Fast Vision,

Nashua, NH) was engaged. This imaging system made use of a 4 megapixel complementary metal oxide semiconductor (CMOS) image sensor with a maximum resolution of 1240 x 1024 and acquisition speed of 1000 frames per second. This high speed camera was controlled with a second PC that contained 3 high-speed frame grabbers (FastFrame 1300, Fast Vision, Nashua, NH) (Figure 26). Because of the high frame rates, images from the high-speed imaging system were not available in real-time and could not be used for control purposes.

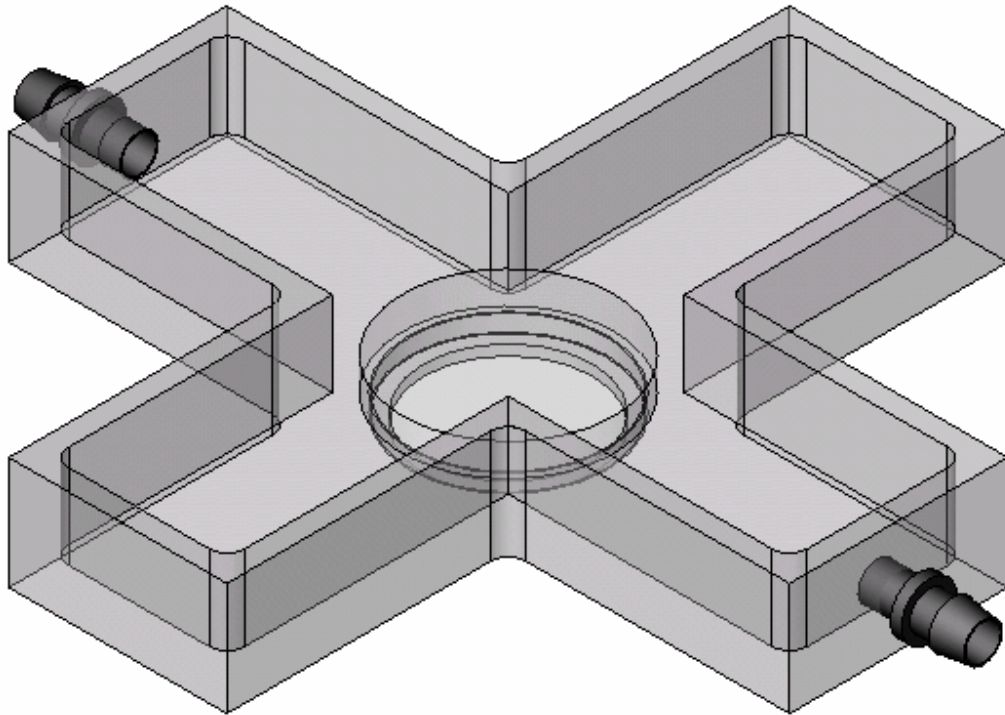


**Figure 28. A CAD model of the cross-shaped specimen bath with specimen window/stand.**



**Figure 29. The dual biaxial testing device dual camera system.**

These images were downloaded after each test and analyzed separately. Both cameras were equipped with 55mm telecentric lenses (H52-271, Edmund Optics, Barrington, NJ) which were focused through a 60-40 beam splitter in order to ensure that both cameras maintained identical specimen views. The greater portion (60%) of the light was directed towards the high-speed

imaging system since this system was more sensitive to light intensity levels due to the rapid image acquisition rates it employed. The specimens were mounted with an orientation parallel to the specimen plane and a sub-specimen 45° angled first-surface mirror was used to direct the camera views to the lower specimen surface. In addition to acquiring images, the high-speed frame grabbers received an image acquisition trigger signal from an analog/digital converter (PCI-6036E, National Instruments, Austin, TX) within the device control computer. This trigger signal served to synchronize the acquired images with load measurements that were acquired by the device control computer from a pair (one on each device axis) of load cells (Model 31, Honeywell Sensotec, Columbus, OH) via the analog/digital converter. The specification for hysteresis in each load cell was 0.5%. All data acquisition and image analysis was accomplished using custom software routines (see Device Algorithms) written using the LabView virtual instrumentation package (Version 6.i, National Instruments, Austin, TX).

### **2.1.3 Device software**

**2.1.3.1 Marker identification.** All images were recorded as 8-bit grayscale images. This resolution provided 256 image intensity increments from black (intensity = 0) to white (intensity = 255). In order to facilitate the location of the graphite markers within the specimen images, an intensity threshold was defined for each experiment which transformed the grayscale specimen images into black and white bitmaps (Figure 30). This was convenient because the graphite markers were typically much darker than the leaflet surface.

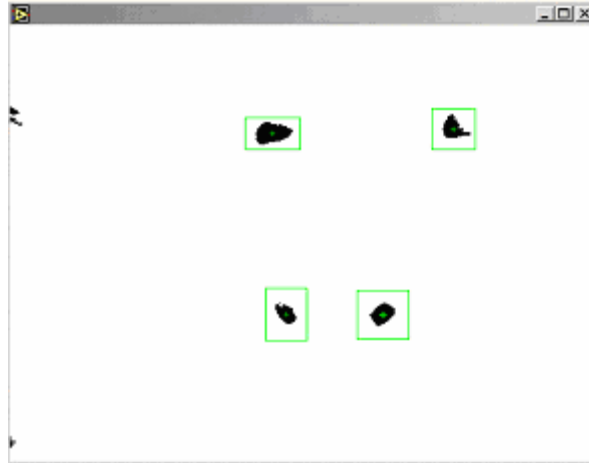


**Figure 30. A sample bitmap showing four markers (black) and the user-defined marker subregions (green).**

This image thresholding technique did not always perform perfectly since, occasionally, the intensity levels of dark markings on the tissue surface or small shadows caused by leaflet surface textures were similar to those of the graphite markers. To correct for this, two additional algorithms were used to identify the markers. First, image subregions were defined for each marker. Once defined, detection of a given marker was only performed within the specified image subregion. The main purpose of this technique was to eliminate the detection of erroneous marker-like shapes that were sufficiently spatially separate from the markers themselves. Because the marker positions within the image moved throughout the test, once a marker was identified within a subregion, the subregion was translated such that it was re-centered on the marker. By translating the subregions with the markers in this way, markers always stayed within the defined subregion as long as they did not translate out of the image subregion in the time duration between individual frames (approximately 0.1 seconds for the device control

camera and 0.002 seconds for the high speed digital camera). To reduce the chances of this occurring, the size of each individual marker subregion was increased to a level that accommodated the motions of the particular marker between frames. After the marker subregions were defined, a size threshold was applied to any markers that were identified within the subregions. This was helpful due to the fact that discolorations on the surface of the leaflets were usually much larger than the graphite markers and had the added benefit of reducing the sensitivity of the marker tracking system to image noise, which occasionally caused small image areas (usually in the single pixel range) to become dark. Marker subregions and detected markers from the device control camera were plotted in green on the device computer monitor specimen image display in real-time so that marker tracking could be visually confirmed. Once markers were located, their precise image coordinates were calculated as the center of area of the pixels below the image intensity threshold.

2.1.3.2 **Stretch calculation.** The stretch calculation method used is well documented for soft tissues [53, 54]. First, consider this generalized homogenous biaxial deformation:

$$x_1 = \lambda_1 X_1 + \kappa_1 X_2, \quad x_2 = \lambda_2 X_2 + \kappa_2 X_1, \quad (8)$$

where  $\mathbf{X}$  and  $\mathbf{x}$  are the location of a particular material particle in the reference and deformed configurations respectively,  $\lambda$  is the stretch ratio, and  $\kappa$  describes the in-plane shear angle.

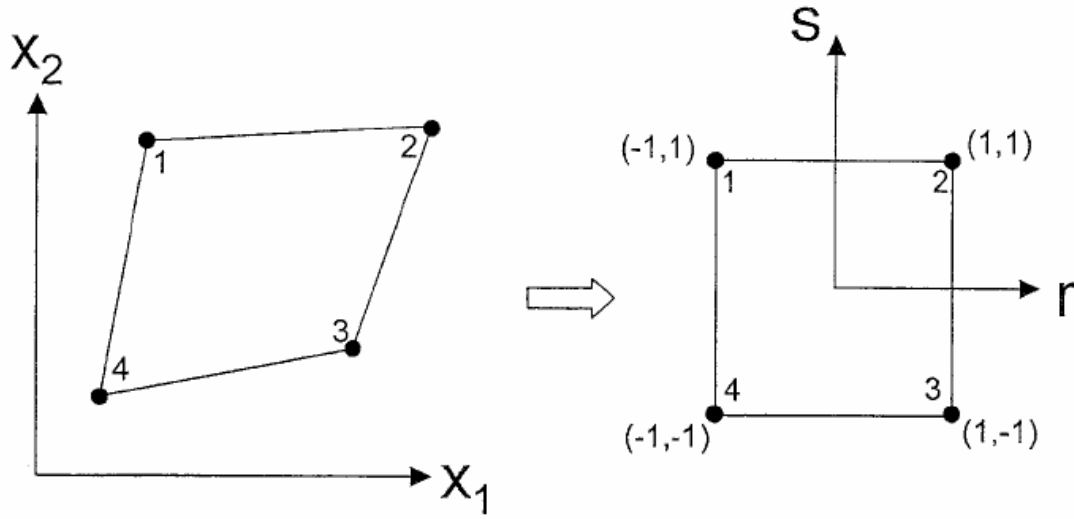


**Figure 31. Marker coordinates were mapped into an isoparametric coordinate system.**

In the biaxial testing protocol,  $X_n$  (where  $n$  is the marker number) are the pixel coordinates of the marker positions in the reference configuration and  $x_n$ , are the time-dependent marker coordinates calculated during the test. Shape functions are used to map the real pixel coordinates into an isoparametric coordinate system (Figure 31) such that the marker displacements  $\mathbf{u}$ , can be calculated as the linear sum of the isoparametric shape functions:

$$\mathbf{u}(r, s) = \sum_{n=1}^m f_n(r, s) \mathbf{u}_n,$$

(9)

where  $\mathbf{f}$  is the set of isoparametric shape functions,  $m$  is the total number of markers,  $n$  denotes a specific marker in the set of  $m$  markers, and  $r$  and  $s$  are the isoparametric coordinates. The spatial derivatives of  $\mathbf{u}$  with respect to  $r$  and  $s$  can then be calculated as:

$$\frac{\partial \mathbf{u}}{\partial r} = \sum_{n=1}^m \frac{\partial f_n}{\partial r} \mathbf{u}_n, \quad \frac{\partial \mathbf{u}}{\partial s} = \sum_{n=1}^m \frac{\partial f_n}{\partial s} \mathbf{u}_n. \quad (10)$$

which can be substituted into:

$$\begin{bmatrix} \frac{\partial}{\partial r} \\ \frac{\partial}{\partial s} \end{bmatrix} = \begin{bmatrix} \frac{\partial u_1}{\partial r} & \frac{\partial u_2}{\partial r} \\ \frac{\partial u_1}{\partial s} & \frac{\partial u_2}{\partial s} \end{bmatrix} \begin{bmatrix} \frac{\partial}{\partial x_1} \\ \frac{\partial}{\partial x_2} \end{bmatrix} \quad (11)$$

to calculate the spatial derivatives of  $\mathbf{u}$  with respect to  $\mathbf{x}$ . These spatial derivatives form the basis of the deformation gradient tensor,  $\mathbf{F}$ , from which  $\lambda$  and  $\kappa$  can be determined by:

$$\mathbf{F} = \mathbf{G} + \mathbf{I} = \begin{bmatrix} \frac{\partial u_1}{\partial X_1} & \frac{\partial u_1}{\partial X_2} \\ \frac{\partial u_2}{\partial X_1} & \frac{\partial u_2}{\partial X_2} \end{bmatrix} + \begin{bmatrix} 1 & 0 \\ 0 & 1 \end{bmatrix} = \begin{bmatrix} \lambda_1 & \kappa_1 \\ \kappa_2 & \lambda_2 \end{bmatrix} \quad (12)$$

This procedure was used to calculate the stretch state of at the center of the marker array, (0,0) is the isoparametric coordinate system. All reported stretch levels were the levels interpolated at this location. For this study, four markers (a 2 by 2 array) were used, providing a bi-linear interpolation of the displacement field. It should be noted that, although it was not used, the biaxial device also included provisions for 9 marker (3 x 3 array) interpolation that could allow bi-quadratic variation of the displacement field.

**2.1.3.3 Quasi-static control.** Due to the non-linear and highly variable mechanical properties of the MV anterior leaflets, the only variables that could realistically be controlled in the quasi-static testing were the loading and unloading time and the upper (peak tensions) and lower (tare configuration) tension limits. In a typical quasi-static loading and unloading cycle, the device carriages moved with constant velocities for the prescribed loading period in order to stretch the centered specimen from the tare configuration to the peak tension limit, reversed direction after the prescribed loading period, then stopped after returning to their original location. Pairs of opposing carriages always moved with the same velocity in order to prevent the specimen from moving out of the camera view, but the two pairs of carriages usually had different velocities in order to account for anisotropic specimen behavior. In the first quasi-static cycle of a given specimen, the carriage velocities were calculated based on stretch estimates input by the user. In this study, these guesses were based on pilot studies of other leaflets as well as experience with other test specimens within the study. Because the carriage velocities required to reach the 90 N/m tension state were highly variable, it was rare that the initial carriage velocity guesses were sufficient. For this reason automated corrections were made to the carriage velocities between cycles. Corrections for each axis were made independently, without considering the correction made on the opposing axis. If the desired peak tension was not reached for a given specimen axis in the desired loading period the following correction was made to the carriage velocity:

$$v_c = v_o \left( \frac{T_{peak}^{desired}}{T_{peak}^{measured}} \right) (C_f) \quad (13)$$

In this formulation,  $v_o$  is the corrected carriage velocity,  $v_c$  is the corrected carriage velocity,  $T_{peak}$  is the peak membrane tension, and  $C_f$  is a user defined correction factor (typically 0.3 for the MV leaflet). The correction factor was used in many of the correction algorithms as a method to decrease the magnitude of the correction. This factor allowed the user to tune the correction algorithms and was very helpful when making corrections to the MV leaflet due to its highly nonlinear mechanical behavior. In essence, the correction factor allowed this linear velocity correction to incrementally make the necessary nonlinear correction over a number of cycles while reducing the propensity of the correction algorithm become stuck in over- and under-correction patterns that are common when linear corrections are made and nonlinear corrections are necessary. Additionally, this correction factor helped reduce the propensity of the correction algorithm to become stuck in over- and under-correction patterns due to the simultaneous corrections (and therefore related coupling effects) on both specimen axes. If, instead of underestimating, the system overestimated the required carriage velocities a different correction was made. If the carriage velocities were too high, the specimen was not stretched for the entire prescribed loading period. Instead, the carriages were stopped once one (or both) of the specimen axes reached the desired peak tension limit. This was done as a safety measure to prevent specimen damage from over-distension. Once the carriages were stopped, they were held for the duration of the loading time before returning to their original configuration. In this case the carriage velocity correction was given by:

$$v_c = v_o \left( \frac{t_{peak}^{measured}}{t_{peak}^{desired}} \right) (C_f) \quad (14)$$

In this formulation,  $t_{\text{peak}}$  is the time to reach the peak tension level in the loading cycle. The effectiveness of these correction algorithms was obviously highly dependent on both the initial carriage velocity guesses and the correction factor. Generally, the 90 N/m equilibrium level was reached in the proper loading duration (15 seconds in this experiment) by the third loading/unloading cycle. In addition to correcting the initial carriage velocity guesses, the correction algorithms allowed the carriage velocities to adapt as the specimen properties shifted due to preconditioning in the initial cycles.

**2.1.3.4 High stretch rate testing.** The high stretch rate testing was always performed after an initial set of 20 quasi-static cycles. Unlike the quasi-static cycles, corrections were not made between the high stretch rate cycles. Instead the carriage velocities from the final quasi-static cycle were simply scaled to accommodate the higher loading times. For instance, the carriage velocity on a given device axis for the first, 1 second high-speed cycle was calculated by multiplying the carriage velocity used in the final 15 second quasi-static cycle by the ratio of quasi-static cycle time to the high-speed cycle time (or 15 in this case). This control method ensured only that the specimen would be loaded and unloaded over the desired high-speed duration to the same carriage displacements reached at the peak of the final quasi-static cycle and back to the tare configuration. Only if the specimen under test did not exhibit any stretch rate sensitivity, would this control method load the specimen to the 90 N/m equilibrium state.

**2.1.3.5 Stress-relaxation testing.** The algorithms used to control the stress-relaxation test were very similar to those used to control the high stretch rate testing. As in the high-speed

cycles, a stress-relaxation experiment always followed a set of quasi-static cycles and the carriage velocities used in the final quasi-static cycle were simply scaled to calculate the carriage velocities required to load the specimen in the 0.1 second rise time. The difference between the stress-relaxation and high-speed loading/unloading cycles was that, after loading the specimen, the carriages were simply held at the peak load configuration for the duration of the test in the case of stress-relaxation.

**2.1.3.6 Creep testing.** As in the high-speed loading/unloading and stress-relaxation tests, the creep test was always performed after a set of quasi-static cycles. The carriage velocities required for the initial 0.1 second loading in the creep test were again calculated by appropriately scaling the quasi-static carriage velocities. The difference between the creep experiment and the stress-relaxation experiment was that, after the initial loading was completed, another algorithm was used to move the device carriages such that the 90 N/m equilibrium state was maintained for the duration of the test. The creep algorithm recalculated this carriage velocity approximately 10 times per second using the following formula:

$$V = (90 - T_{measured})(S_f) \quad (15)$$

where  $V$  is the carriage velocity,  $T_{measured}$  is the current membrane tension and  $S_f$  is a scaling factor that converts the membrane tension difference into the appropriate velocity. In this formulation, negative carriage velocities corresponded to compressions while positive carriage velocities corresponded to stretches. As in the quasi-static tension control, the carriage velocity

for each axis was evaluated separately, ignoring any mechanical coupling effects between specimen axes.

The creep algorithm relied heavily on the fact that the MV was not sensitive to stretch rate. Had this not been the case, the initial loading would not have brought the specimen to the desired 90 N/m equi-tension state and the effectiveness of the creep control algorithm to effectively correct such a possibly large discrepancy is questionable.

## **2.2 CHARACTERIZATION OF DEVICE PERFORMANCE**

### **2.2.1 Stretch measurement system**

In order to measure the performance of the stretch measurement system, artificial marker arrays with known deformations were created using SolidWorks CAD software. The prescribed stretches were chosen to be representative of the physiologic stretch levels observed in the MV anterior leaflet. These marker arrays were printed onto paper and the individual printed paper marker arrays were placed on the specimen window facing down. All of the marker tracking methods that were used on actual specimens (see Marker tracking) were carried out on the paper marker arrays. The specimen stretches calculated by the biaxial testing software were then compared to the prescribed stretches to evaluate the accuracy of the marker tracking method.

### **2.2.2 Load cell calibration**

Load cells were calibrated using a custom calibration fixture (Figure 32) which allowed weight standards to be applied to the specimen attachments. This custom fixture attached to the side of the specimen bath and contained 2 pulleys. Using these two pulleys, the weight of a standard could be redirected, via suture similar to that used in actual testing, to the specimen attachment suture pulleys. A two point calibration procedure was carried out using weights of 1 kg and no weight (0 load condition) until the calibration was repeatable, then the linearity of the load cells was tested by hanging a 500 g weight. The weight of the paper clip attachment was 1.3 g and was compensated for in the calibration and measurement results.

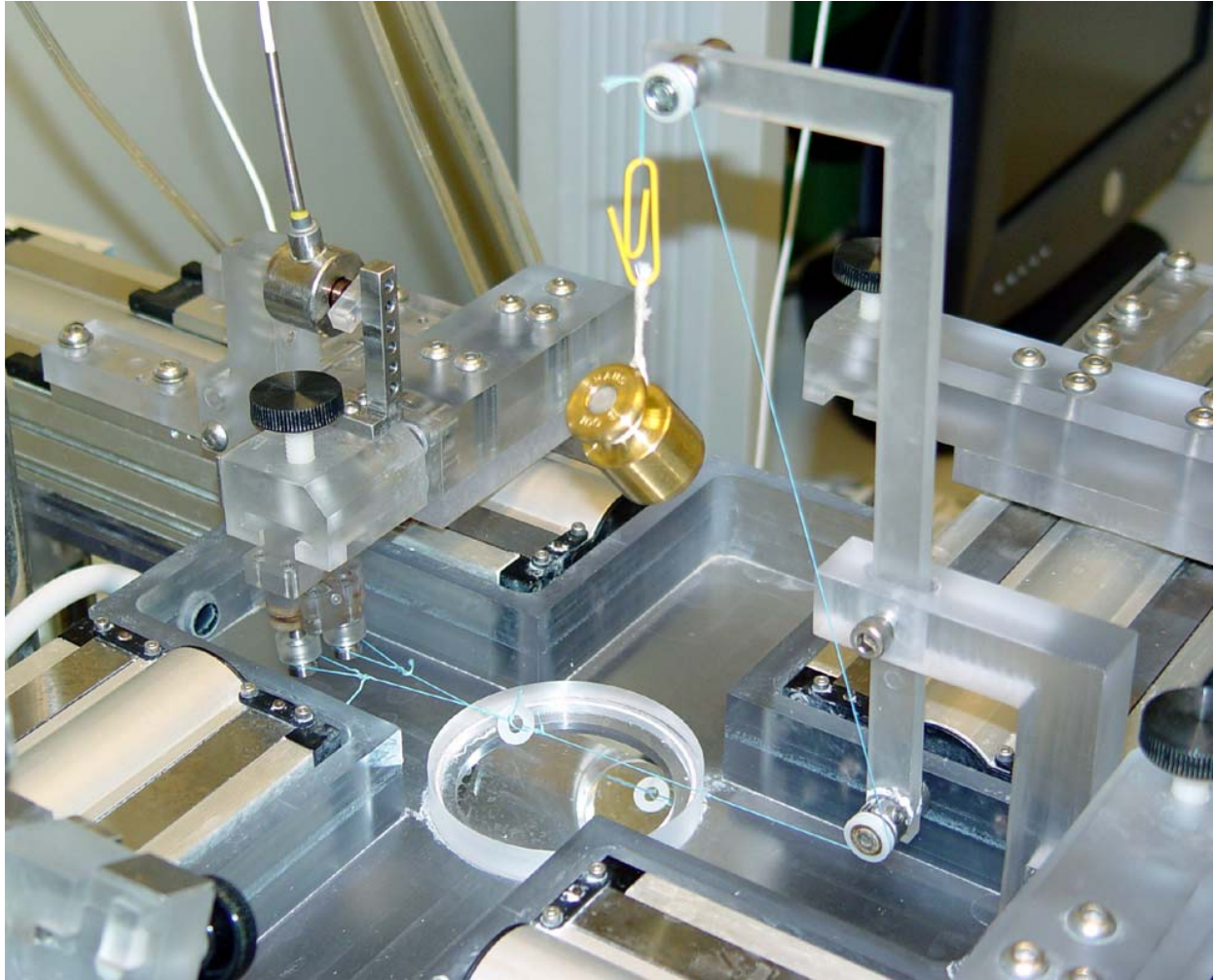


**Figure 32. A photograph of the calibration fixture mounted on the bath.**

### **2.2.3 Ability to reach quasi-static peak loads**

The ability of the device to reach desired peak loading state was evaluated using a latex specimen. For this experiment, peak loads were set at 300g for both axes. Peak specimen loads were measured for 10 quasi-static cycles to assess the ability of the device to reach the desired peak loads.

### **2.2.4 Load cell momentum sensitivity**

In order to assess the effects of rapid motion on the load cells, carriage displacements similar to those predicted for testing were performed without any loads on the load cells. This test measured the sensitivity of the load cells to rapid motions. In this test, one axis was totally unloaded while the other axis was sutured with a latex sample and was loaded to a stretch of 1.1 over 0.2 seconds.

### **2.2.5 System relaxation**

In order to ensure that any stress-relaxation observed in the leaflet testing was real and not simply a relaxation in the test system components, a relaxation test was performed with the opposing sutures hooked to each other without any specimen. By performing a test in this way, the relaxation of the system was quantified and any relaxation greater than that observed in the system itself could be considered real. Suture sets were loaded to a tension of 200g in 0.1 seconds and subsequent relaxation was measured for 3 hours.

## 2.3 BIAXIAL TESTING OF THE MV ANTERIOR LEAFLET

### 2.3.1 Specimen preparation

One set of eight (designated for stretch-rate sensitivity analysis), a second set of eight (designated for biaxial stress-relaxation experiments), a third set of six (designated for uniaxial stress-relaxation experiments) and a fourth set of six (designated for biaxial creep experiments) fresh porcine anterior MV leaflets were obtained from a local slaughterhouse (Table 1). Hearts were obtained immediately after slaughter whereupon the anterior leaflets were removed from each heart and were then stored in a phosphate buffered saline (PBS) solution and frozen for no longer than one week for later use. Prior to testing, each leaflet was thawed at 37°C and trimmed to provide a square specimen with sides parallel to the circumferential and radial axes of the leaflet (Figure 33). Specimens were carefully cut out so that each specimen was centered circumferentially on the anterior leaflet and extended radially from just below the annulus to just above the first chordae tendineae attachment site. Trimmed specimens had dimensions of  $9.9\pm 0.6$  mm x  $9.5\pm 0.9$  mm x  $0.75\pm 0.05$  mm (thickness measured in the center of the specimen); specimen dimensions were measured by hand using calipers. In order to attach the square specimen to the biaxial testing device, four evenly spaced suture lines were hooked through each side of the specimen with stainless steel surgical staples (for uniaxial experiments 2 edges were left free). To provide a basis for optical stretch measurement 4 small graphite markers (~ 250  $\mu$ m in diameter) were glued to the specimen center using a cyanoacrylate adhesive (Permabond, Somerset, NJ) in a 2 x 2 array formation with dimensions of approximately 3mm x 3mm.

**Table 1. Specimen database**

<b>Specimen</b>	<b>Test</b>	<b>Circ (mm)</b>	<b>Rad (mm)</b>	<b>Thickness (mm)</b>
HS1	High Stretch Rate	10	10	0.7366
HS2	High Stretch Rate	9	9	0.635
HS3	High Stretch Rate	11	10	0.8128
HS4	High Stretch Rate	12	11	0.7874
HS5	High Stretch Rate	9	9	0.762
HS6	High Stretch Rate	9	8	0.6096
HS7	High Stretch Rate	10	9	0.7112
HS8	High Stretch Rate	10	10	0.8128
BSR1	Biaxial Stress-relaxation	10	9	0.80
BSR2	Biaxial Stress-relaxation	10	9	0.72
BSR3	Biaxial Stress-relaxation	10	10	0.69
BSR4	Biaxial Stress-relaxation	11	11	0.75
BSR5	Biaxial Stress-relaxation	10	9	0.78
BSR6	Biaxial Stress-relaxation	9	9	0.80
BSR7	Biaxial Stress-relaxation	10	9	0.79
BSR8	Biaxial Stress-relaxation	10	9	0.65
CSR1	Circumferential Stress-relaxation	9	10	0.81
CSR2	Circumferential Stress-relaxation	9	10	0.76
CSR3	Circumferential Stress-relaxation	10	11	0.75
RSR1	Radial Stress-relaxation	9	10	0.83
RSR2	Radial Stress-relaxation	10	10	0.67
RSR3	Radial Stress-relaxation	11	9	0.78
C1	Creep	10	9	0.74
C2	Creep	11	11	0.75
C3	Creep	11	11	0.71
C4	Creep	10	11	0.82
C5	Creep	9	9	0.81
C6	Creep	9	9	0.70

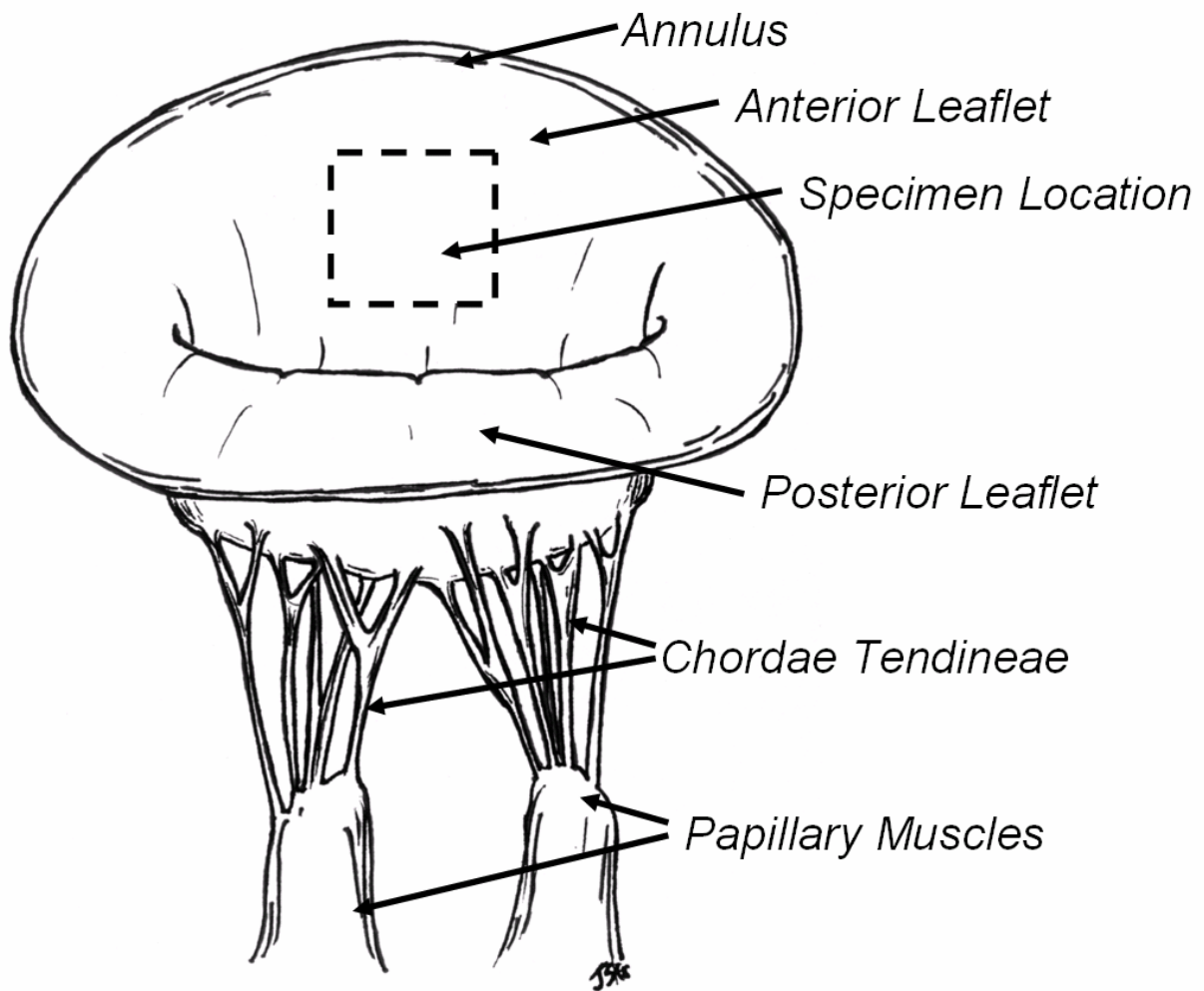


**Figure 33. Diagram of the native mitral valve. Square specimens were taken from the anterior leaflet with sides parallel to the circumferential and radial axes of the leaflet centered circumferentially and extending radially from just below the annulus to just above the first chordae tendineae attachment site.**

### 2.3.2 Quasi-static biaxial testing

Specimens were mounted in the biaxial testing device with the circumferential and radial specimen axes aligned with the device axes (Figure 35) within a specimen bath which was filled with PBS and maintained at a temperature of 37° C for the duration of testing. Each leaflet underwent 20 preconditioning cycles (Figure 34) in which the specimen was stretched such that the membrane tension (**T**) (defined as the force per unit length of tissue over which it was applied) along each specimen edge was increased to 90 N/m over a cycle period of 15 seconds, then was returned to its original configuration over an additional period of 15 seconds. To increase test repeatability, all loading cycles were initiated at a tare load of 0.5g and all presented stretch data were referenced to the preconditioned tare configuration which was taken at the 0.5g tare load after the 20 preconditioning cycles. After the preconditioned tare reference was recorded, specimens underwent either a high-speed stretch rate sensitivity testing protocol, a stress-relaxation protocol or a creep protocol.

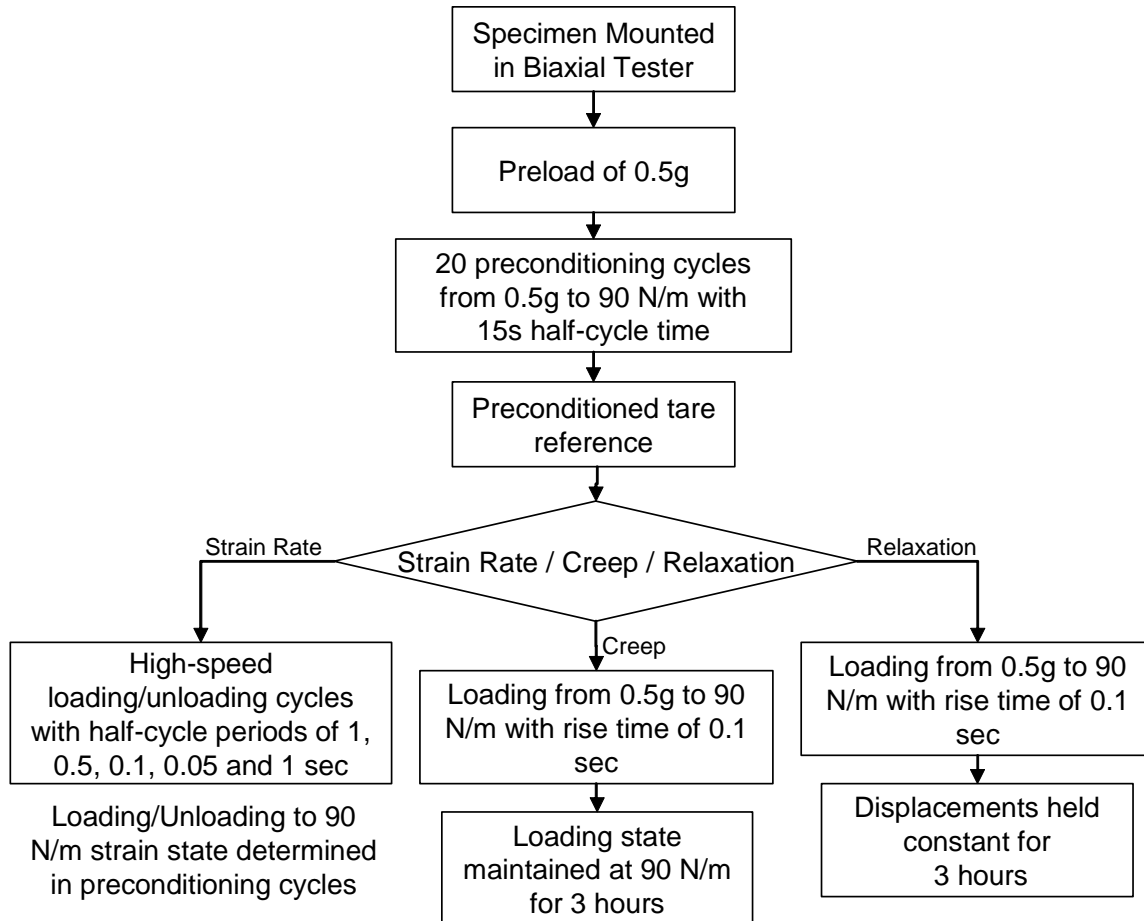


**Figure 34. Biaxial stretch rate sensitivity, creep, stress-relaxation, and uniaxial stress-relaxation protocols.**

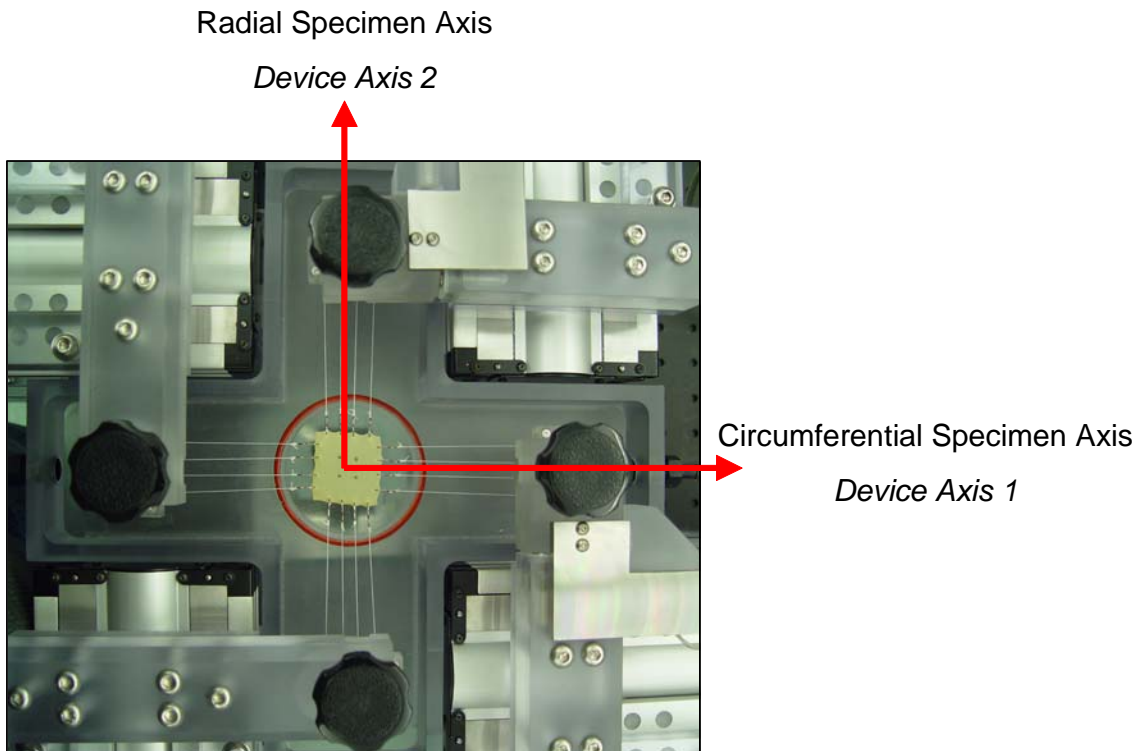


**Figure 35. Specimens were mounted in the biaxial testing device with the circumferential and radial specimen axes aligned with the device axes.**

### **2.3.3 High-speed biaxial testing**

For the stretch rate sensitivity testing, the carriage displacements required to stretch the specimen to the 90 N/m equitension state in the preconditioning cycles were recorded and repeated for 5 additional high speed cycles in which the specimen was stretched and unstretched in loading and unloading cycle periods of 1 second, 0.5 seconds, 0.1 seconds, 0.05 seconds and finally again in 1 second to assess test repeatability. For the relaxation and creep protocols, the device carriages

were returned to displacements required to stretch the specimen to the 90 N/m equitension state in the preconditioning cycles in a rise time of 0.1 seconds. The 0.1 second rise time was chosen because it was very close to the physiologic rise time and was slow enough that any vibrations associated with rapid carriage decelerations at the peak loading state were limited ( $\pm 2\%$  of the peak load). In the stress-relaxation protocol the device carriages were then locked in the displaced positions and the specimens were allowed to relax for 3 hours. For the creep protocols, after reaching the 90 N/m equitension state, the membrane tensions in both the circumferential and radial directions were sustained for 3 hours by adjusting the carriage positions at a rate of approximately 10 Hz in order to maintain the desired membrane tensions. This was accomplished by displacing each axis independently at a rate  $V$  given by  $V = C (90 - T_m)$ , where  $C$  is a tuning constant and  $T_m$  is the measured membrane tension on the axis to be adjusted. For this formulation, positive values of  $V$  corresponded to stretches while negative values of  $V$  corresponded to compressions. Satisfactory maintenance of the 90 N/m equitension state (see RESULTS Table 4) was achieved by evaluating and adjusting each axis independently, ignoring any mechanical coupling between the circumferential and radial specimen axes. Each specimen was used for only one stretch rate sensitivity, stress-relaxation or creep protocol.

### 2.3.4 Kinematic analysis

The leaflet stretches at the 90 N/m equitension state,  $\lambda_c^{\text{peak}}$  and  $\lambda_r^{\text{peak}}$ , were used to quantify leaflet extensibility. In the stretch rate sensitivity protocols, leaflet hysteresis was evaluated by comparing the energy stored in the loading phase to the energy dissipated in the unloading phase for each loading rate. Energy stored/dissipated was calculated as the area beneath the T vs. stretch curve. Areas were calculated using a trapezoidal rule numerical integration.

For the stress-relaxation protocols, membrane tension data were normalized to the peak membrane tension observed for each leaflet. For all specimens, this peak membrane tension was reached immediately after the initial 0.1 second loading. The relaxation percentage was calculated as  $R(\%) = (T^{\text{peak}} - T^{3\text{hr}})/T^{\text{peak}}$  for each axis. Relaxation data was thinned to 20 data points evenly distributed through the duration of testing reduce processing time, and then fit with a reduced relaxation function for long relaxation periods with a single phase relaxation distribution. Where  $c$  was the magnitude of the relaxation distribution,  $\tau_1$  was the short relaxation time constant and  $\tau_2$  was the long relaxation time constant. Creep data was analyzed by comparing the circumferential and radial stretches at four time points: immediately after the initial loading ( $\lambda^{100\text{ms}}$ ), 300 milliseconds ( $\lambda^{300\text{ms}}$ ), 1 second ( $\lambda^{1\text{s}}$ ), and 3 hours ( $\lambda^{3\text{h}}$ ). Creep percentage  $C(\%)$  was calculated as  $C(\%) = (\lambda - \lambda^{100\text{ms}})/(\lambda^{100\text{ms}} - 1)$ .

### 2.3.5 Statistical methods

For all tests, the circumferential and radial data groups were considered separately and the uniaxial and biaxial stress-relaxation groups were considered separately. To determine the effects of stretch rate on each biomechanical parameter in the stretch rate sensitivity protocols (i.e.  $\lambda_c^{\text{peak}}$ ,  $\lambda_r^{\text{peak}}$ , and hysteresis), comparisons between all loading times were performed using one way Analysis of Variance (ANOVA). The Holm-Sidak method was then used to perform pair wise comparisons between loading time groups to further elucidate any significant differences. Student's t-test was used to assess any directional differences between specimen axes in both creep and relaxation experiments and to compare uniaxial and biaxial relaxation percentages. Additional comparisons between creep percentages at 100 ms, 300 ms, 1s and 3 hr were performed using one way ANOVA for both the circumferential and radial creep data sets. All tests were performed with a commercial statistics software package (SigmaStat; SPSS Inc., Chicago, IL). All data values are presented as the mean  $\pm$  the standard error of the mean (SEM).

## 3.0 RESULTS

### 3.1 CHARACTERIZATION OF DEVICE PERFORMANCE

#### 3.1.1 Stretch Measurement Accuracy

The stretch measurement system was found to be accurate to within a stretch of  $\pm 0.001$  (Table 2) and shear angle was measured to within 0.1 degrees.

**Table 2. Stretch measurement accuracy**

<b>Stretch 1</b>		<b>Stretch 2</b>		<b>Shear Angle (°)</b>	
<i>Prescribed</i>	<i>Measured</i>	<i>Prescribed</i>	<i>Measured</i>	<i>Prescribed</i>	<i>Measured</i>
1.200	1.199	1.600	1.600	30.0	29.9
1.200	1.200	1.600	1.600	30.0	29.8
1.200	1.199	1.600	1.600	30.0	29.9

### **3.1.2 Load cell calibration**

After a repeatable calibration was completed, the mean load measurement of the 500g standard was  $501.3 \pm 0.4$  g.

### **3.1.3 Ability to reach peak loads**

The ability of the device to reach the desired equibiaxial tension state of 300 g using a latex test sample is presented in Table 3. The first two cycles were not close to the desired peak loads due to the initial guesses used for the first cycle. These results show the ability of the device correction algorithms to correct for inaccurate initial displacement guesses (see METHODS for details). After the second cycle, the peak loads were reached with a high degree of accuracy. The mean absolute differences between the desired and measured peak loads were  $0.94 \pm 0.83$  g (circumferential) and  $0.12 \pm 0.12$  g (radial).

**Table 3. Peak loads for the ten cycle test using a latex test sample.**

<i>Cycle</i>	<b>Peak Load (g)</b>	
	<i>Axis 1</i>	<i>Axis 2</i>
1	210.3	215.9
2	290.8	295.5
3	299.3	301.5
4	301.1	299.7
5	298.8	300.9
6	301.0	299.9
7	299.0	300.8
8	298.9	299.4
9	301.2	299.6
10	299.8	298.0

### **3.1.4 Load cell momentum sensitivity**

The unloaded device axis showed no sensitivity to high-speed motion (Figure 36). Very little change was observed in the load data from the unloaded axis. This was demonstrated by a linear function which was fit to the load data from the unloaded axis with a slope of 0.006 g/s over the 0.2 second duration. A plot of the residuals showed no clear pattern, indicating that the unloaded axis was not affected by the high speed, rapid acceleration, or sudden deceleration of the carriage displacement.

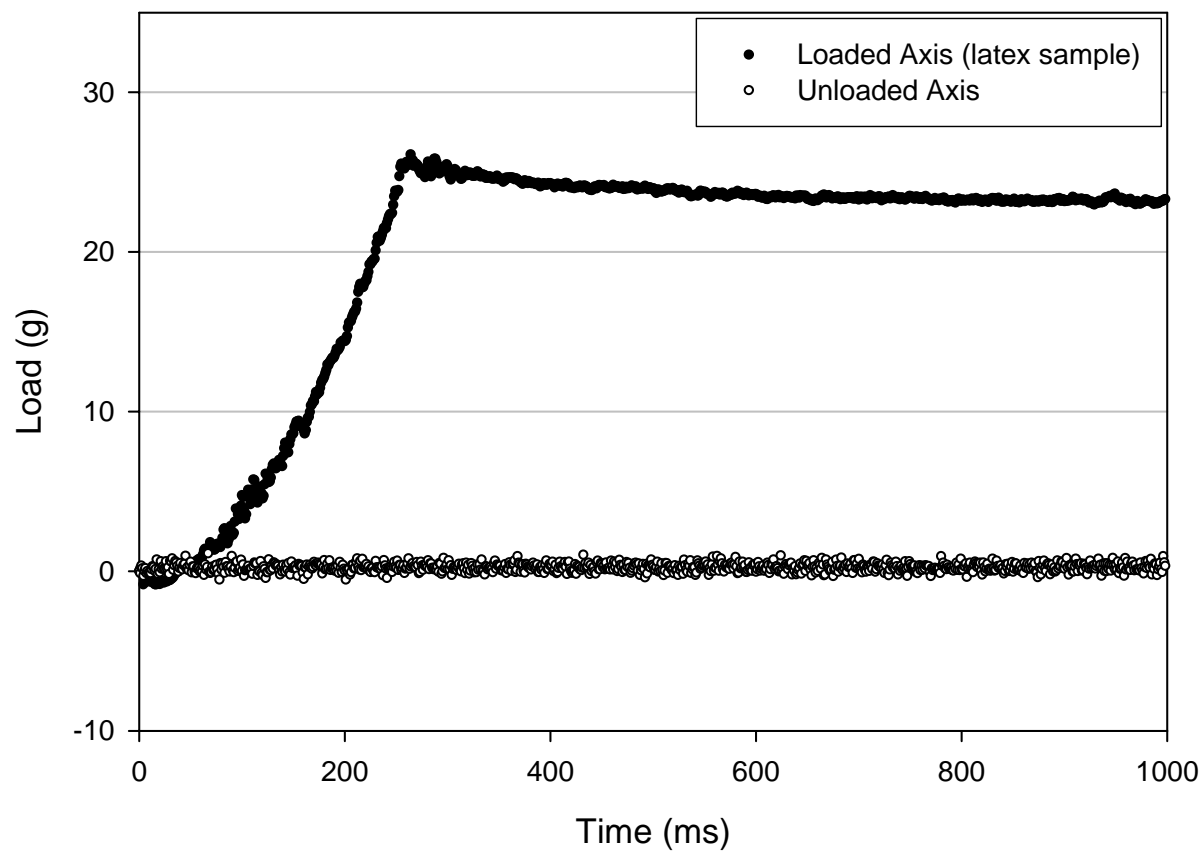


**Figure 36. Load versus time curves for the loaded axis (closed symbols) and unloaded axis (open symbols) showed that the load cell on the unloaded axis was not affected by rapid motions.**

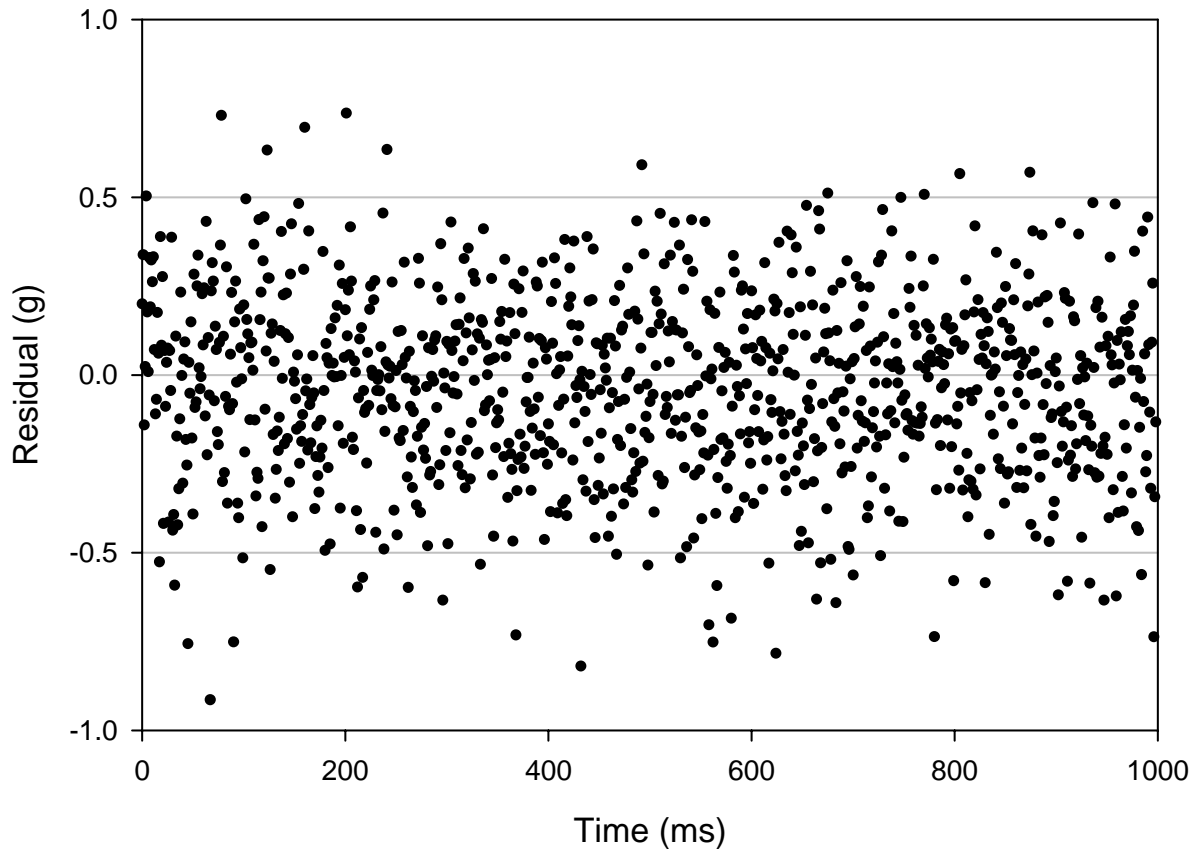


**Figure 37. Residuals versus time for the unloaded axis showed no clear trend, further indicating that the unloaded axis was not affected by rapid motions.**

### 3.1.5 System relaxation

The suture-only relaxation test (Figure 38) showed that the level of relaxation in the system itself was minimal. After the three hour test duration relaxation percentages were 1.2 percent on the first device axis and 1.6 percent on the second device axis.

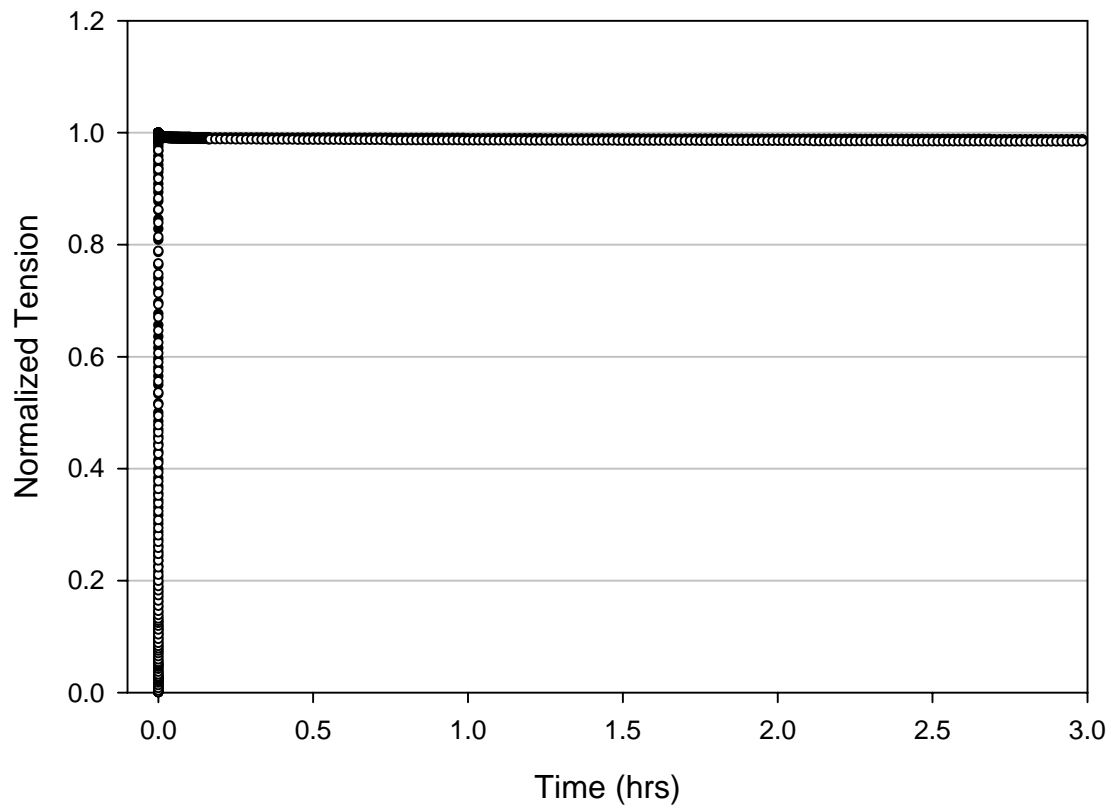


**Figure 38. Relaxation of the biaxial test system and sutures. Both device axes (open symbols: device axis 1, closed symbols: device axis 2) showed minimal relaxation and were indistinguishable from each other.**

## 3.2 EFFECTS OF STRETCH RATE

### 3.2.1 Device Control

Tension and stretch vs. time loading curves were similar among the full range of cycle periods (Figure 40), demonstrating that the biaxial device was able to accurately control loading and unloading time for the different cycle periods. Additionally, the level of test repeatability was found to be quite high as displayed by the close agreement between the first and final 1 second loading/unloading protocols (Figure 39). Between these two protocols, the mean change in  $\lambda_c^{\text{peak}}$  was found to be  $0.006 \pm 0.002$  and the mean change in  $\lambda_r^{\text{peak}}$  was  $0.010 \pm 0.005$ , demonstrating a high degree of accuracy and reproducibility.

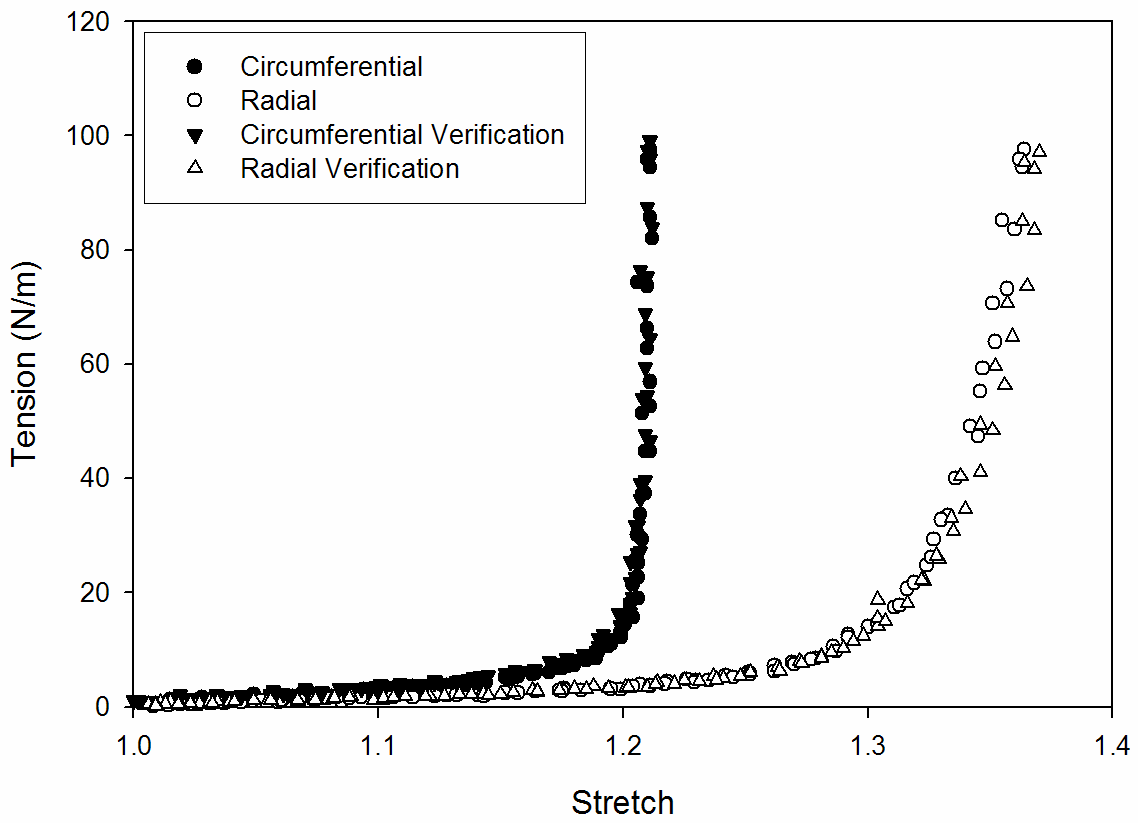


**Figure 39. Typical tension-stretch curves for the initial and final 1s loading/unloading protocols.**

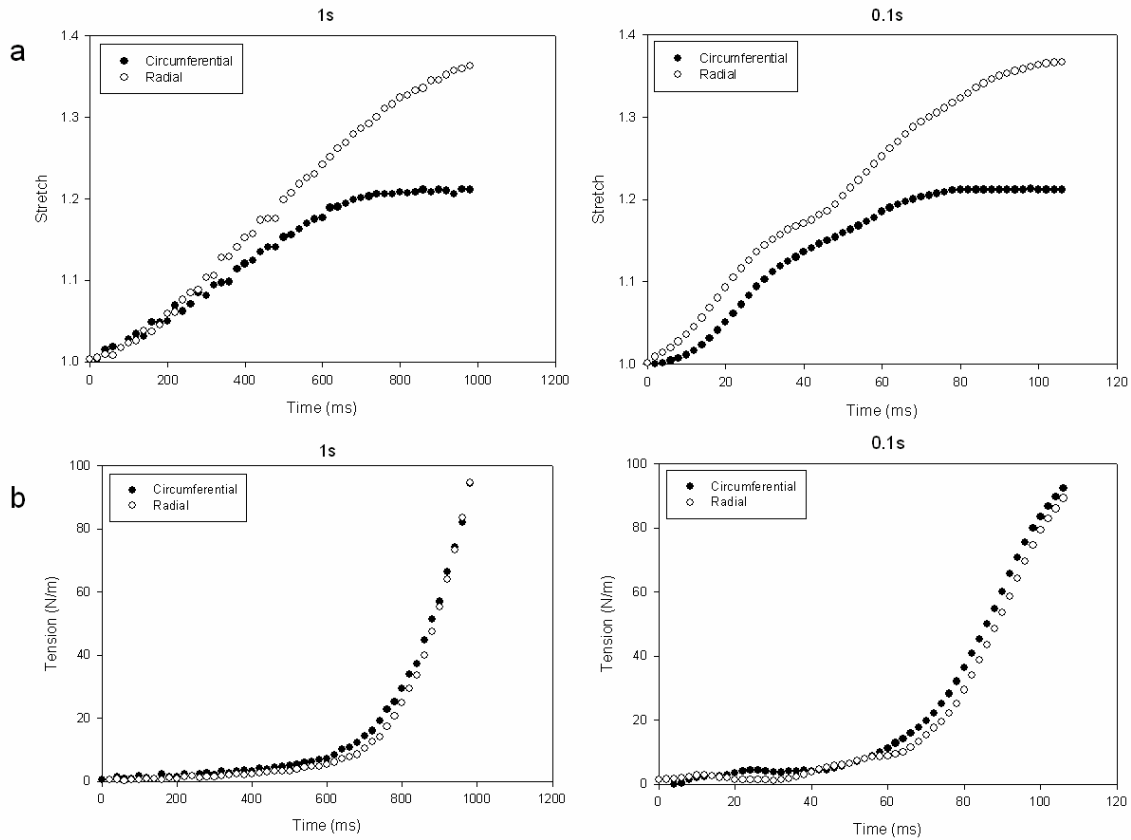


**Figure 40. Typical (a)Load versus time and (b)stretch versus time curves for 1s and 0.1s loading periods. The load versus time and stretch versus time curves were similar for the full range of cycle periods. As displayed above, the device was able to accurately control rise time for different cycle periods. Note the different time scales between the 1s and 0.1s plots.**

### 3.2.2 Effects of Stretch Rate on Stress-Stretch Response

The shapes of the tension vs. stretch loading curves for all loading protocols (15s, 1s, 0.5s, 0.1s, 0.05s) were very similar for each specimen tested (Figure 41). To better present the stretch rate effects, mean  $\lambda_c^{\text{peak}}$  and  $\lambda_r^{\text{peak}}$  for each cycle period were pooled for all specimens (Figure 42). No significant differences were found between any of the loading time protocols in both the circumferential ( $p=0.987$ ) and radial ( $p=0.996$ ) directions. In addition,  $\lambda_c^{\text{peak}}$  and  $\lambda_r^{\text{peak}}$  for all loading times were very similar to, but generally were slightly greater than, the peak stretches observed in left ventricle-simulating flow loop [32]. Moreover the ratio of the mean  $\lambda_c^{\text{peak}}/\lambda_r^{\text{peak}}=0.86$  was very close in value (0.83) to the same ratio observed under simulated physiologic conditions. These results suggest that the 90 N/m peak tensions used in the present study were comparable to actual physiological stress levels.

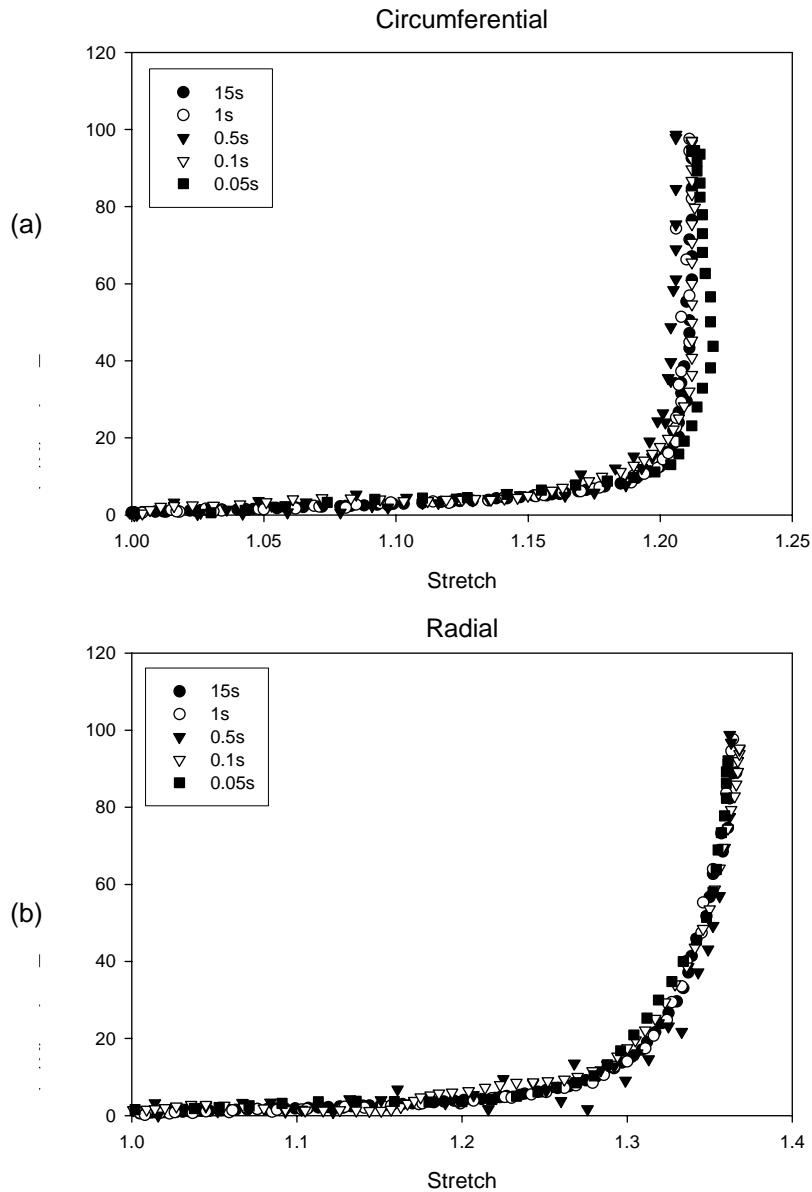


**Figure 41. Typical tension-stretch curves for each loading cycle period (15s, 1s, 0.5s, 0.1s, and 0.05s) for the circumferential (a) and radial (b) specimen directions. Curves generally showed no apparent stretch rate-dependence. Note the different stretch scales between the circumferential and radial plots.**

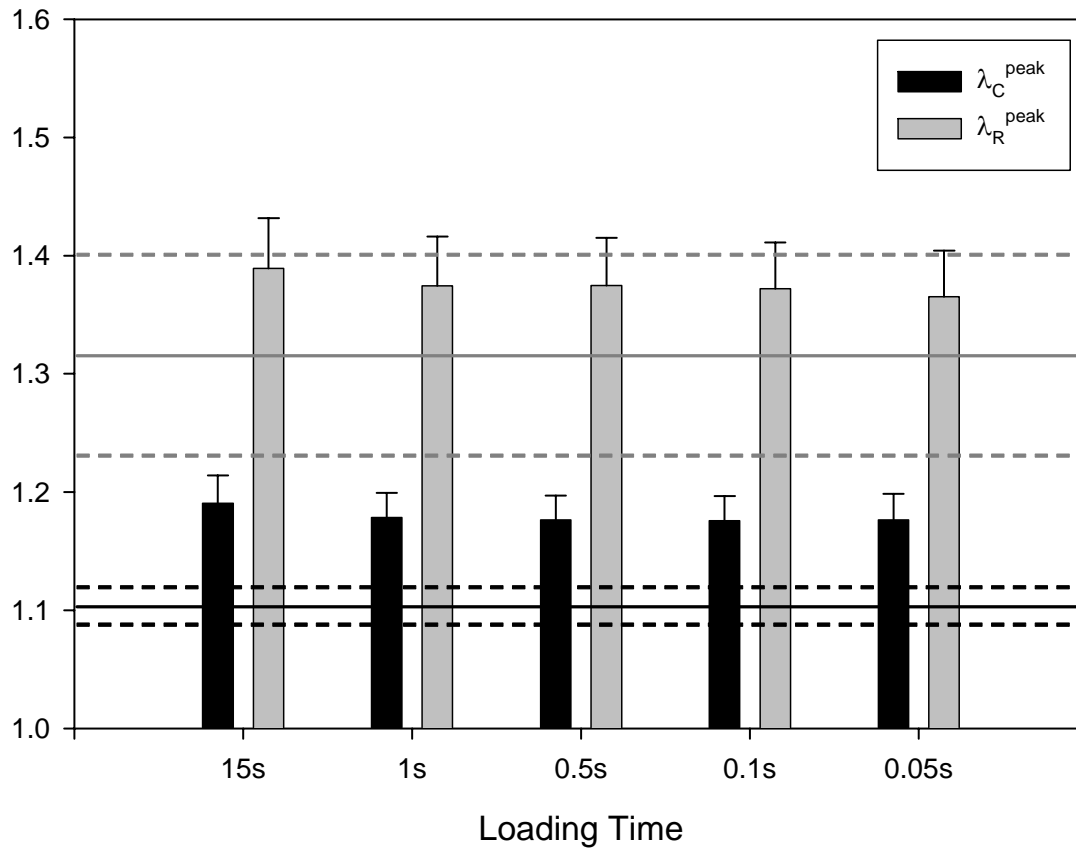


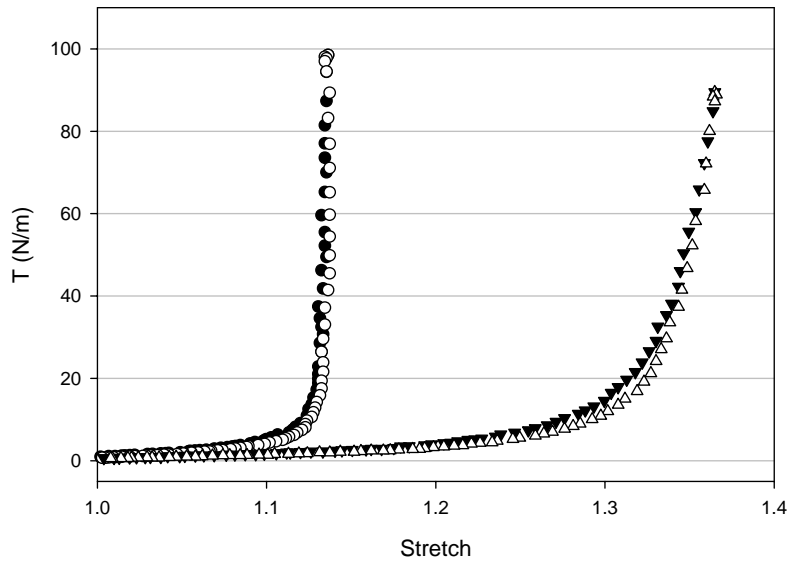
**Figure 42. The circumferential and radial stretches of the leaflet at the 90 N/m equitension state.**

### **3.2.3 Effects of Stretch Rate on Hysteresis**

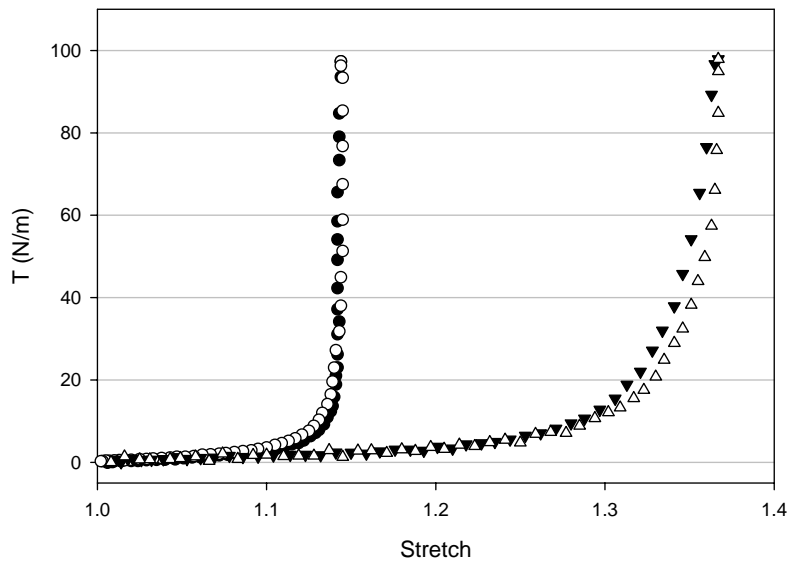
Typical loading and unloading curves for a set of stretch rate protocols on a single leaflet are shown in the four separate panes of Figure 43. Stretch energy storage during loading and dissipation during unloading were minimal due to the extremely nonlinear mechanical behavior of the MV leaflet. As shown in Figure 44, larger amounts of energy were stored in the leaflet at lower tension levels due to the relatively higher level of extensibility of the leaflet tissue at lower stretch levels.

The area beneath the membrane tension versus areal stretch curves (Figure 45) were not statistically among different cycle times for either the loading or unloading phases. Hysteresis levels, loading energy minus unloading energy, were significantly greater than zero for the 15s and 0.1s cycle times only ( $p < 0.01$ ).

15 seconds



1 second



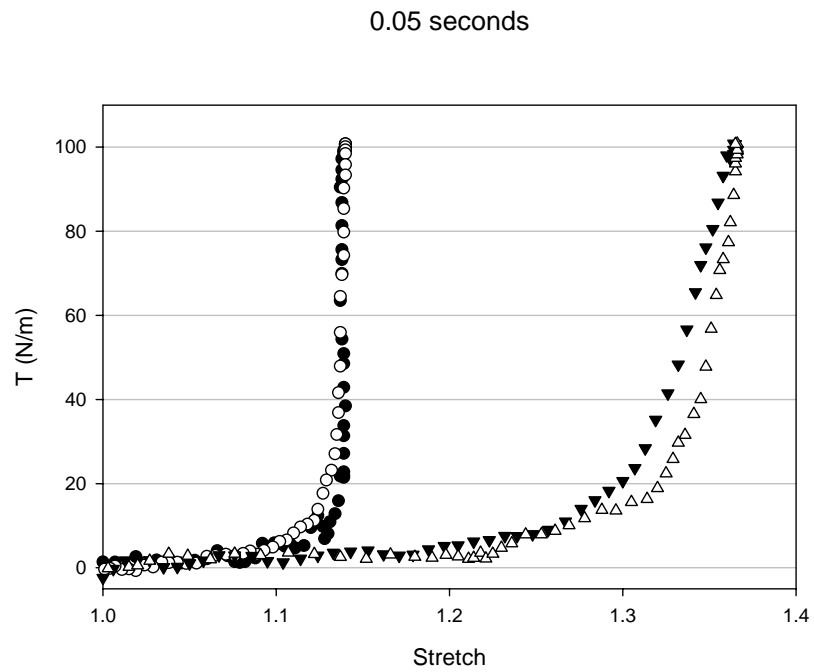
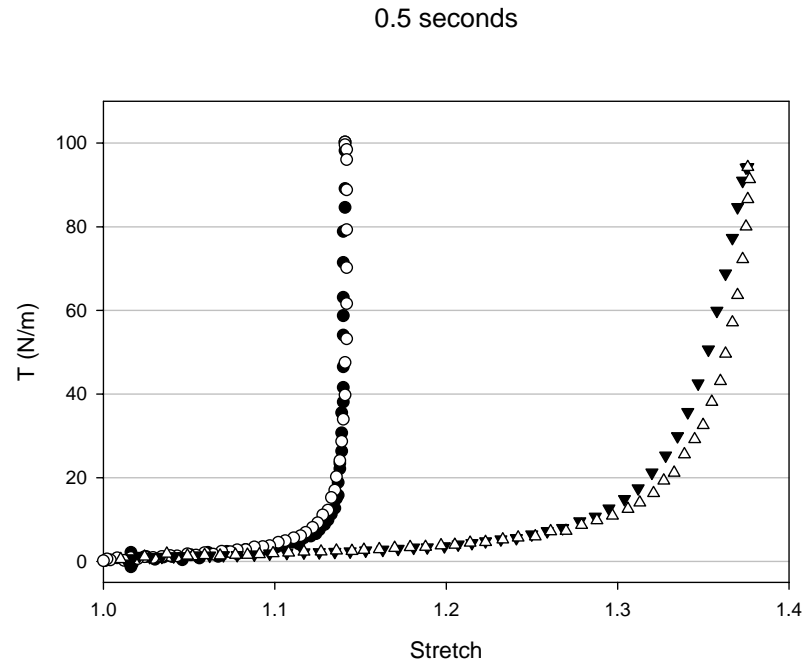


**Figure 43. Loading and unloading membrane tension (T) vs. stretch curves for 15, 1, 0.5 and 0.1 second loading and unloading of a single specimen.**

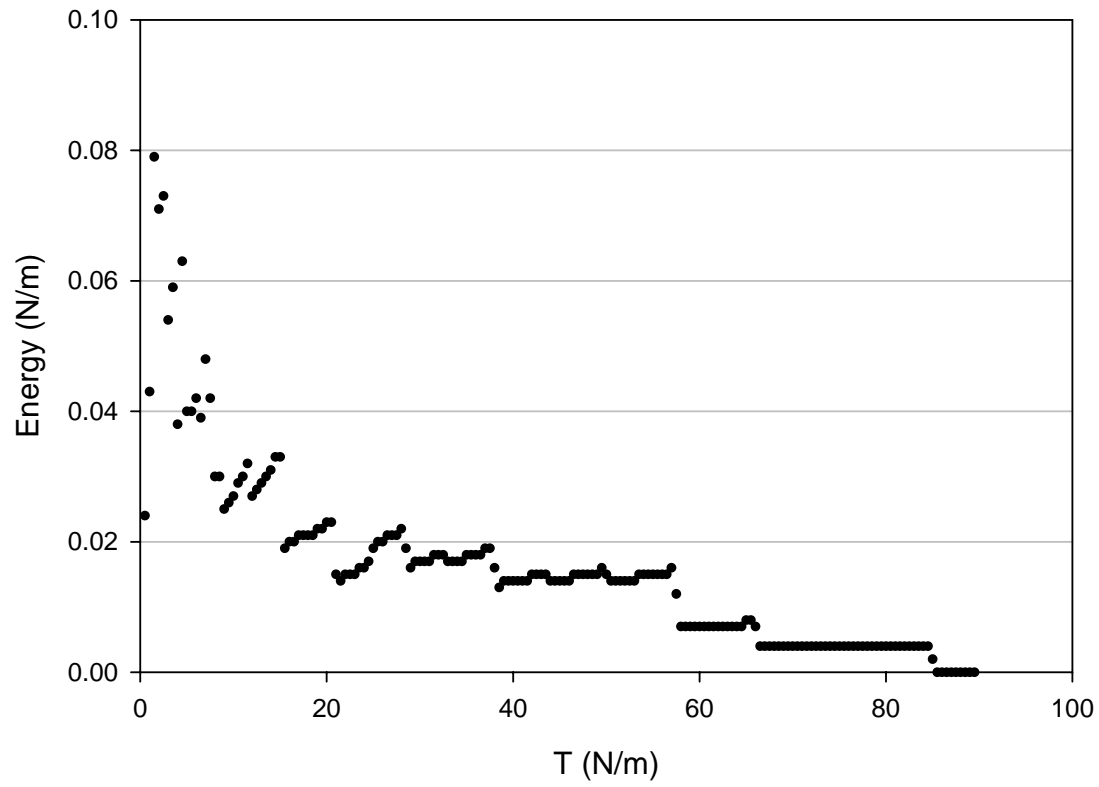


**Figure 44. Membrane stretch energy versus membrane tension for a typical loading cycle. Note the larger amount of energy storage in the tissue at lower tension levels due to the relatively higher tissue extensibility at low stretch levels.**

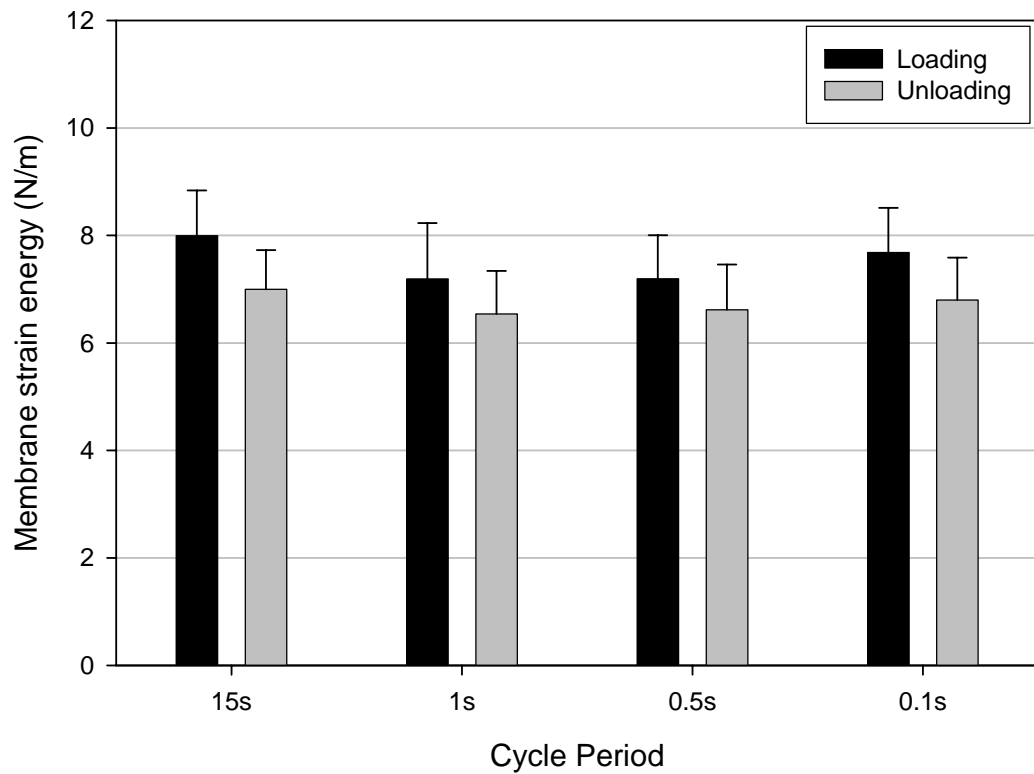


**Figure 45. Energy stored or dissipated within the leaflet specimens during loading and unloading phases with different cycle times.**

### 3.3 STRESS-RELAXATION AND CREEP

#### 3.3.1 Device control

The stretching device was able to load the MVAL specimens to the 90 N/m uniaxial or equibiaxial state smoothly, with minimal vibrations, over the initial 100 ms rise time (Figure 46). Due to the rapid speeds required to load the tissue within the 100 ms rise time and the high level of stiffness in the MVAL at the 90 N/m membrane tension level, the stretching mechanism occasionally slightly overshoot the 90 N/m target.

Due to the rapid speeds required to load the tissue within the 100 ms rise time and the high level of stiffness in the MVAL at the 90 N/m membrane tension level, the stretching mechanism occasionally slightly overshoot the 90 N/m target. Mean peak realized membrane tensions were  $93.2 \pm 2.1$  N/m on the circumferential axis and  $97.1 \pm 2.5$  N/m on the radial axis for uniaxial stress-relaxation experiments and  $102.2 \pm 2.8$  N/m on the circumferential axis and  $103.4 \pm 3.4$  N/m on the radial axis for biaxial experiments. Despite this overshoot, the ratio of the peak circumferential and radial membrane tensions was always maintained near 1 ( $0.99 \pm 0.01$ ) in biaxial experiments.

For stress-relaxation experiments, the overshoot was not corrected; however, as stated in the methods section, stress-relaxation results were calculated and normalized for each specimen based on the peak membrane tension measured for the proper individual experiment. In cases where overshoot occurred during creep experiments, the membrane tension state was corrected within the first second of the test by the same device control algorithm that maintained the 90 N/m equibiaxial tension state for the duration of the test. The creep algorithm was able to

maintain the 90 N/m membrane tensions very well over the entire duration of the creep tests (Table 4).

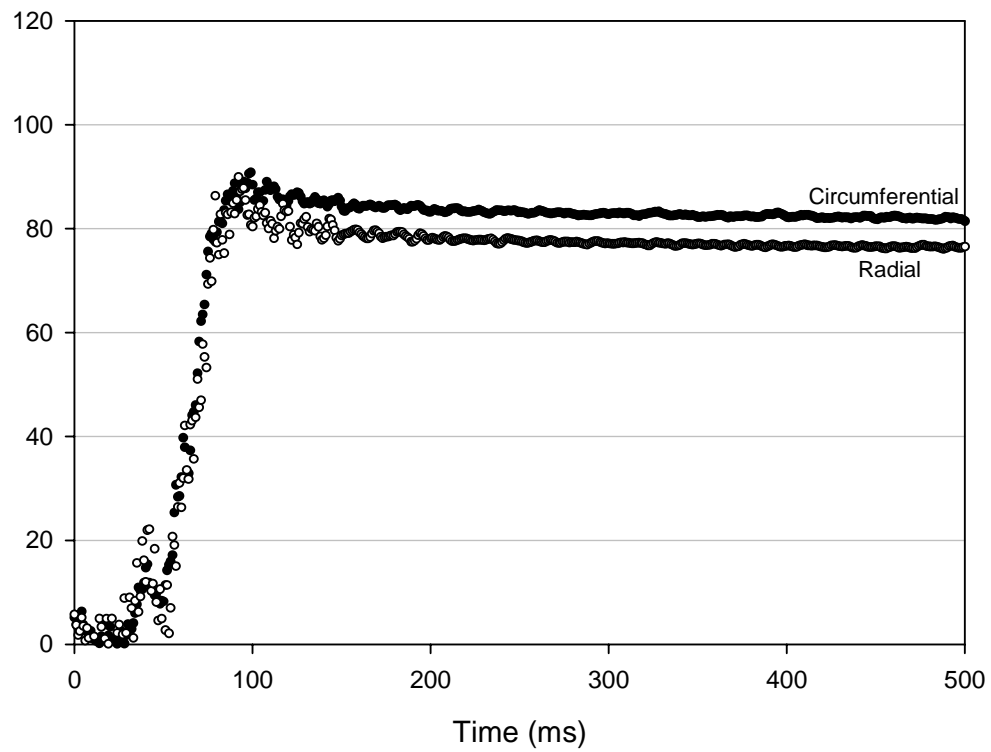


**Figure 46. Typical membrane tension versus time curves for the first 500 ms of a biaxial stress-relaxation experiment. The biaxial stretching mechanism was able to load the specimens within the allotted 100 ms rise time with minimal vibrations and overshoot.**

**Table 4. Circumferential and radial membrane tensions  $\pm$  STDEV for all creep tests after the initial loading phase.**

<b>Specimen</b>	<b>Circumferential (N/m)</b>	<b><math>\pm</math></b>	<b>Radial (N/m)</b>	<b><math>\pm</math></b>
1	89.96	0.34	89.87	0.37
2	89.97	0.24	89.92	0.30
3	89.88	0.58	89.75	0.93
4	89.97	0.31	89.94	0.15
5	90.03	0.71	89.88	0.48
6	89.94	0.13	89.91	0.21
<i>Mean</i>	89.96	0.39	89.88	0.41

### **3.3.2 Biaxial Stress-Relaxation**

Relaxation was observed on both the circumferential and radial axes (Figure 47). The most drastic relaxation was observed within the first 15 minutes of testing, but specimens continued to relax up to and beyond the 3 hour time point. The change in membrane tension from immediately after initial loading (at 100 ms) to 3 hrs was statistically different for each specimen axis ( $P < 0.001$  for both specimen axes). Relaxation was always greater in the radial direction. The ratio of circumferential to radial membrane tensions at 3 hours,  $1.10 \pm 0.02$ , was statistically different from the same ratio at 100 ms,  $0.99 \pm 0.01$  ( $P < 0.001$ ) and the relaxation percentage in the circumferential direction,  $24.67 \pm 0.93$  was statistically different from the relaxation percentage in the radial direction,  $32.09 \pm 0.77$  ( $P < 0.001$ ) (Figure 48).

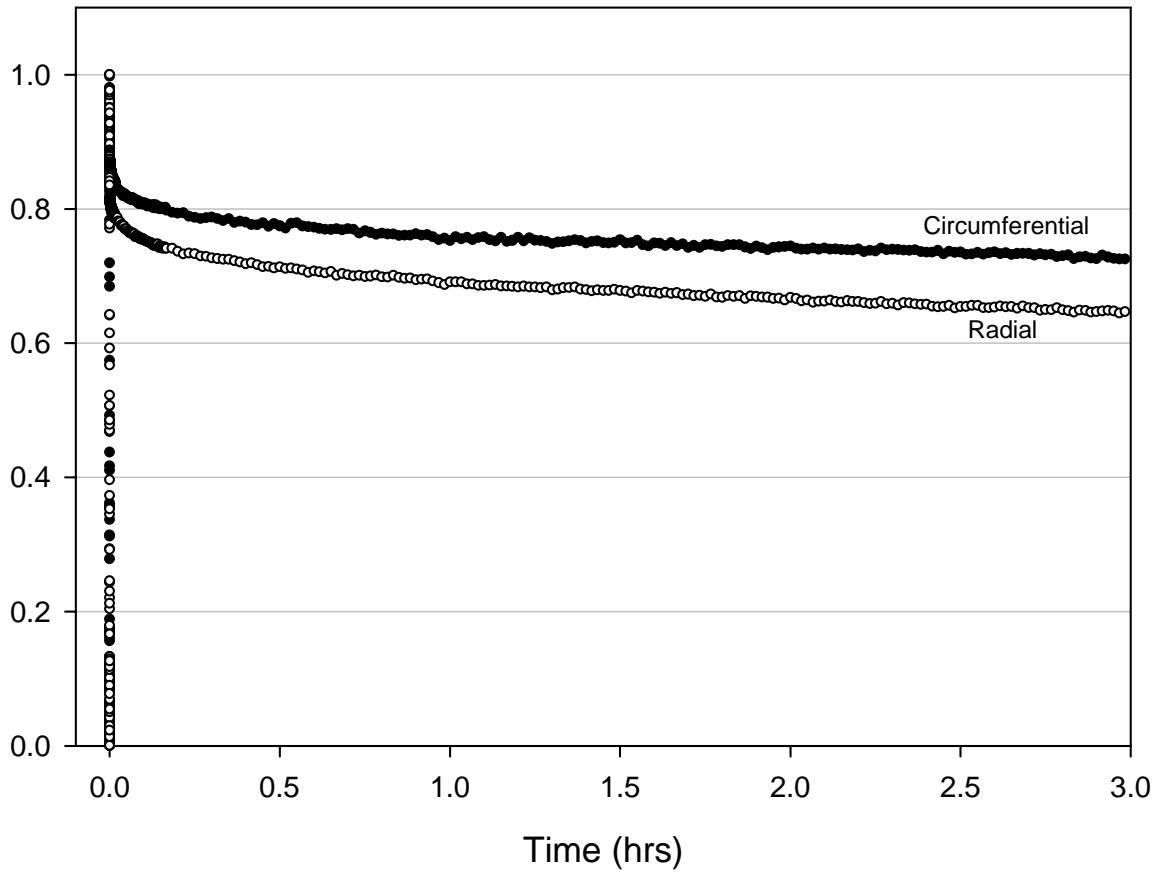


**Figure 47. Membrane tension versus time curves for a typical stress-relaxation experiment. Membrane tension levels at 3 hours were statistically less than those immediately after loading (100 ms) for both specimen axes.**

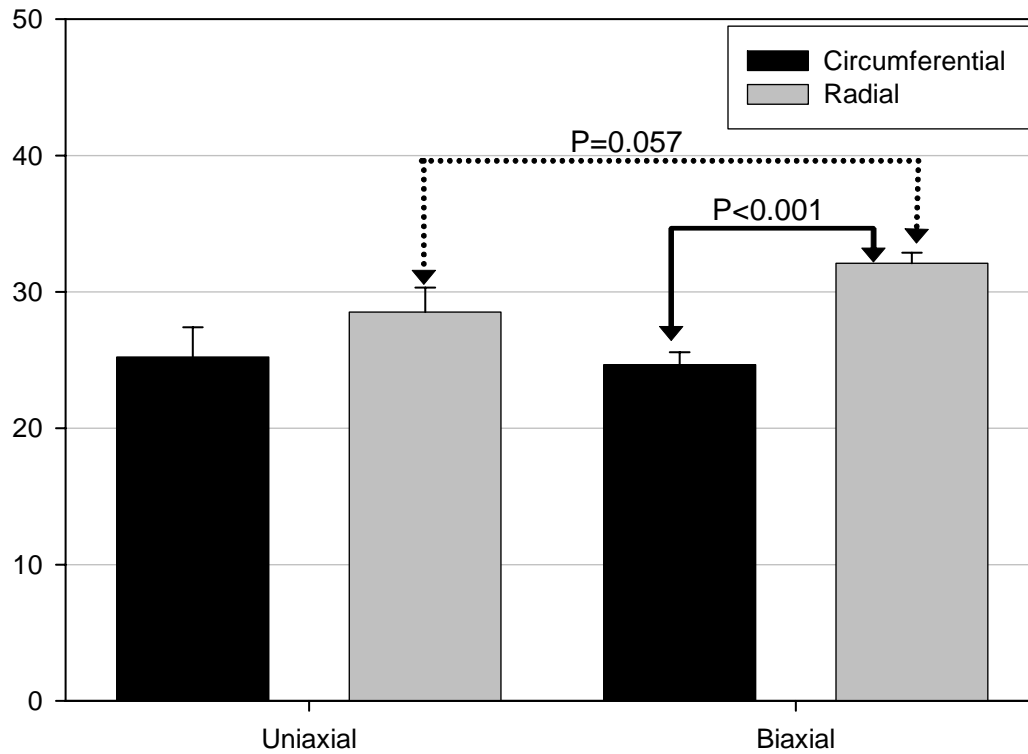


**Figure 48. Relaxation percentage for different test groups and specimen axes. Relaxation was observed in both uniaxial and biaxial experiments, however, the amount of radial relaxation was significantly greater in the biaxial experiments and the circumferential and radial relaxation percentages were not statistically different in the uniaxial experiments as they were in the biaxial experiments.**

### 3.3.3 Uniaxial Stress-Relaxation

Specimens tested uniaxially also exhibited relaxation on both the circumferential and radial specimen axes. As observed in the biaxial stress-relaxation experiments, the peak membrane tensions in both the circumferential and radial directions were statistically greater than the membrane tensions measured at the 3 hour time point ( $P < 0.001$  for each specimen axis). However, unlike the biaxial relaxation experiments, the relaxation percentages observed in the circumferential ( $25.2 \pm 2.2$ ) and radial ( $28.5 \pm 1.8$ ) experimental groups were not statistically different from each other ( $P = 0.305$ ) and a comparison between the uniaxial and biaxial relaxation percentages revealed that the biaxial relaxation was significantly greater ( $p < 0.05$ ) in the radial direction, while the uniaxial and biaxial relaxation percentages were not statistically different in the circumferential direction ( $p = 0.78$ ).

### 3.3.4 Reduced Relaxation Function Fit

Both the uniaxial and biaxial relaxation data for both the circumferential and radial axes were fit quite well (Figure 49) with the one phase reduced relaxation model with an  $r^2$  value of  $0.996 \pm 0.002$  for all specimens. Model parameters for all specimen fits are presented in appendix A.

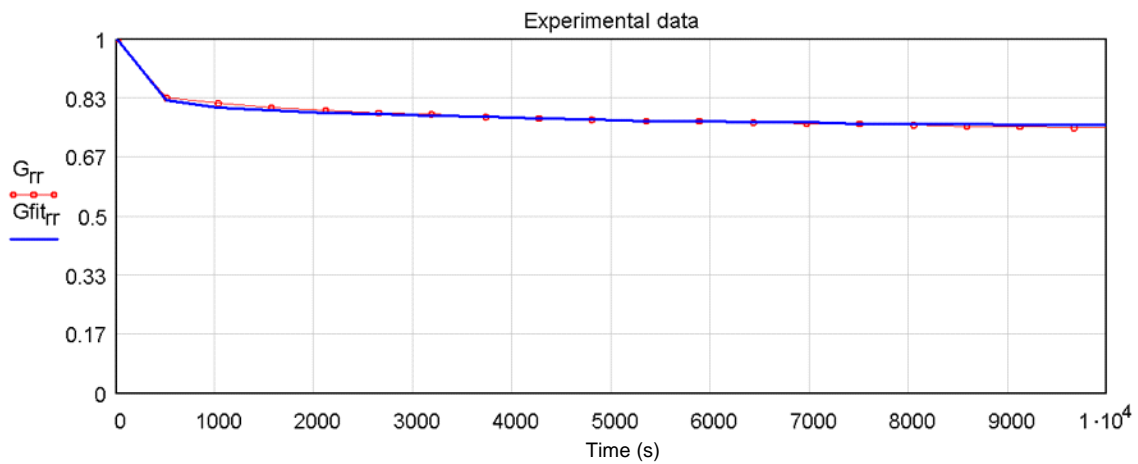


**Figure 49. The one phase reduced relaxation model fit both the uniaxial (pictured) and biaxial relaxation data very well for both the circumferential and radial (pictured) axes.**

### 3.3.5 Creep

The high degree of mechanical anisotropy in the leaflet, as seen in the stretch rate sensitivity protocols, was also observed in the creep experiments. Specifically, peak stretches at the 100 ms time point were  $1.12 \pm 0.014$  in the circumferential direction and  $1.36 \pm 0.048$  in the radial direction.

In sharp contrast to the relaxation results, the observed creep was minimal in both the circumferential and radial specimen axes (Figure 50). Mean stretches in the circumferential direction stayed constant over the entire three hour test duration, and were minimal in the radial direction. Creep percentages (Figure 51) were not statistically different from zero at any time point in the circumferential direction and were statistically different from zero only for the 3 hour time point in the radial direction (Table 5).

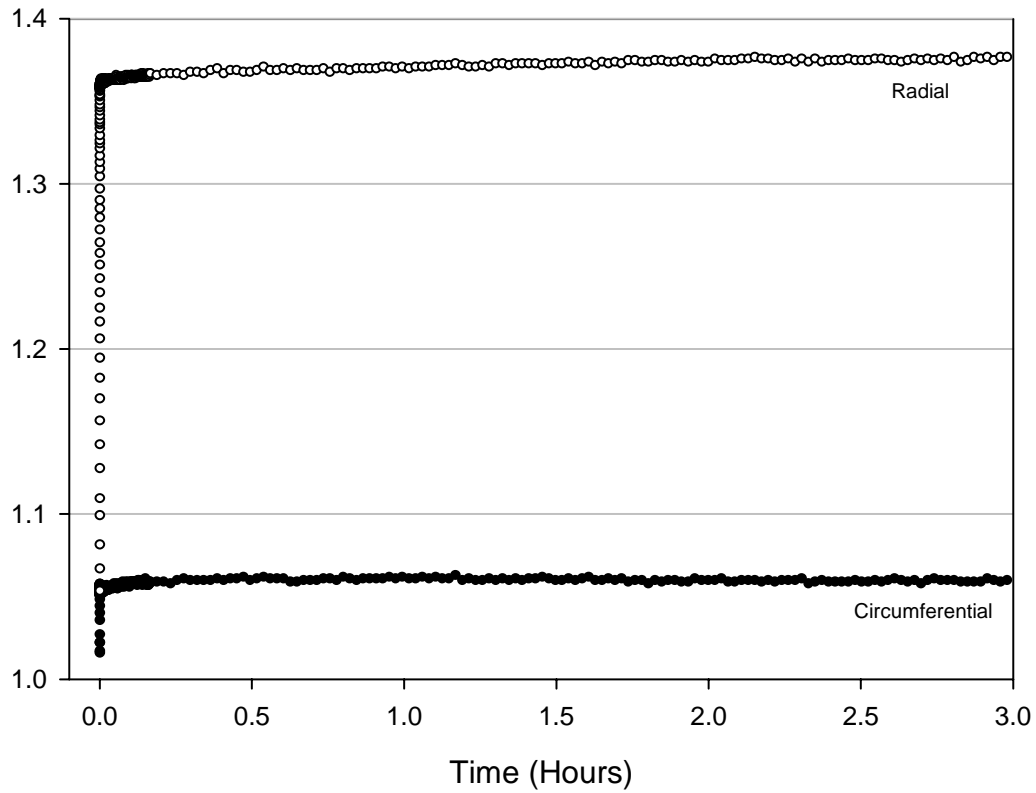


**Figure 50. Stretch versus time curves for a typical biaxial creep experiment. Minimal relaxation was observed on either axis. Note the anisotropic leaflet behavior exhibited by the relatively higher radial stretch required to maintain the 90 N/m membrane tension.**

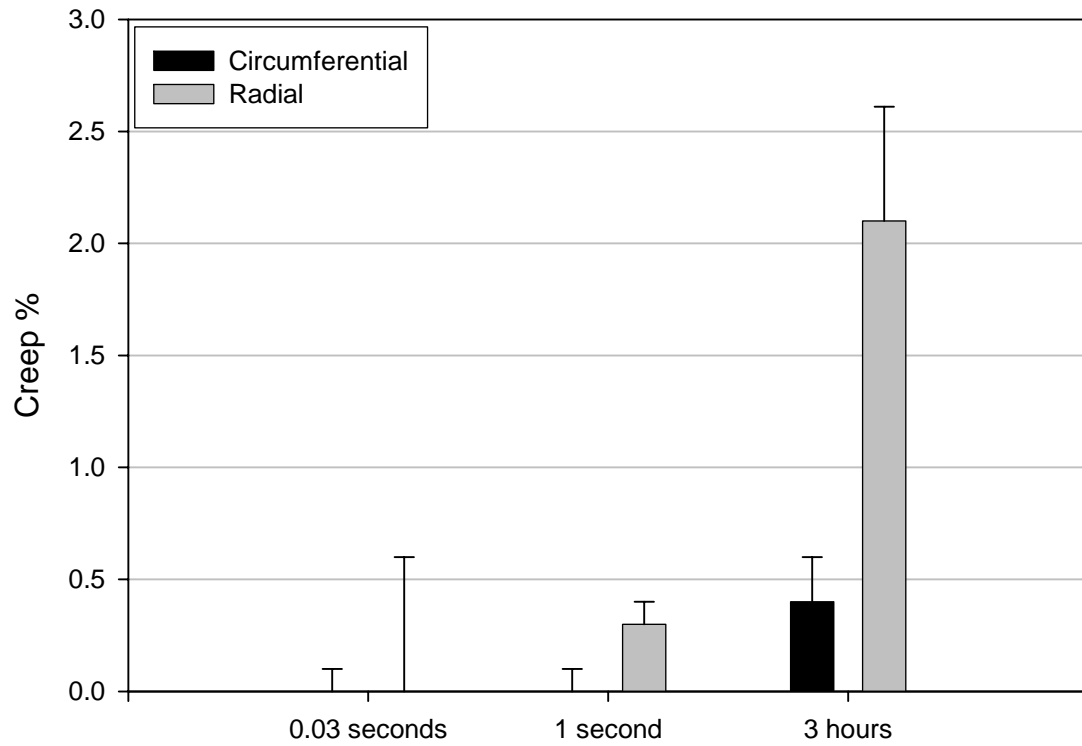


**Figure 51. Creep percentages were not statistically different from zero for any time point on the circumferential or radial axes.**

## **4.0 DISCUSSION**

### **4.1 RELEVANCE OF STUDY**

This work details the first known study of the effects of stretch rate on the biaxial mechanical properties of the MVAL, and indeed for any valve leaflet tissue. These studies are the first to report the application of high stretch rate studies under biaxial loading for any soft tissue. Furthermore, this is the first study known to the authors to report biaxial creep results for any soft tissue and is the first relaxation study to incorporate physiological loading times and a physiological biaxial loading condition. These findings are of particular importance to the development of time dependent constitutive models for valve leaflet tissues because they demonstrate tissue properties at physiologic stretch levels and rates. This characterization of the material properties of the native valve will provide an improved basis for the comparison and qualification of potential replacement materials and repair techniques and is a necessary step in the development of future computational models and material simulations [55].

## 4.2 MECHANICAL ANISOTROPY

The classic nonlinear stress-stretch relationship exhibited by the MVAL leaflet observed in the present study was consistent with previous biaxial findings of May-Newman and Yin [34], as well as the transvalvular pressure-areal stretch relationship observed by Sacks et al [32]. The three-phase curve consisted of a roughly linear toe region, in which the leaflet deformed extensively while developing minimal membrane tension, followed by a highly nonlinear transition region, in which leaflet stiffness increased rapidly before reaching a plateau and entering a second linear region. Efforts have been made to explain this phenomena using collagen fiber recruitment theories [56, 57], but the microstructural details remain to be elucidated for the MVAL.

In the present study, for all leaflet specimens the circumferential axis exhibited lower stretch levels for a given tension level than did its radial counterpart. This result supported the finding that the marker region used in this study consisted predominantly of circumferentially oriented collagen fibers [58], since collagen fibers primarily resist only axial loads. This finding was also consistent with the stretches observed by Sacks et al. [32] in a left-heart simulating flow loop. The close agreement of the peak stretches observed at the 90 N/m equitension state and the peak stretches observed in the left-heart simulating flow loop when the MVAL was in the closed configuration suggested that the 90 N/m peak equitension biaxial loading state was reasonably representative of the maximum physiologic stress state. The close agreement observed between the ratio of circumferential and radial stretches at the 90 N/m equitension state compared to those observed in-vitro for the functioning MVAL was of particular importance because it implied that

the rotational kinematics of the underlying fiber structure were comparable to those of the MVAL in vivo.

### 4.3 STRETCH RATE EFFECTS

One of the primary findings of this study was that the stress-stretch behavior of the anterior MVAL was independent of stretch rate in both the circumferential and radial directions over the full range of cycle periods from 15 seconds to 0.05 seconds studied. This result was in close agreement with the results reported by Naimark et al. [59] that showed no significant stretch rate-dependence in the stress-stretch relationship of mammalian pericardia for stretch rates between 1 and 100%/second. Naimark suggested that the lack of stretch rate dependence may be due to the pseudo-plastic shear-thinning of the glycosaminoglycan matrix surrounding the collagen fibers.

Conversely, this result differed from those detailed in the work of Leeson-Deitrich [42] for aortic and pulmonary valves who reported significant differences in the stress-stretch response at different stretch rates. Our results also differed from the results reported by Lee et al. [60] who observed stretch rate sensitivity of the glutaraldehyde-stabilized porcine aortic valve in the circumferential axis only. Lee et al. linked the explanation of this behavior to the presence of major collagen bundles, which were observed to span the valve parallel to the circumferential leaflet axis. It should be noted that a similar collagen arrangement has been observed in the anterior MV leaflet [58] and we observed no directional differences in stretch rate sensitivity. It is unclear whether the differences between our results and those reported in these two studies

were derived from differences in material, or if they were a product of the differences in loading condition (biaxial tension versus uniaxial tension).

The hysteresis of the MVAL was difficult to compare between different loading/unloading cycle times due to the extremely small amount of energy stored within the MVAL. The traditional definition of hysteresis: the difference between the areas beneath the loading and unloading curves may not be appropriate for biaxially loaded specimens because, due to coupling effects, one axis may actually contract at high tension levels, creating an undefined integration of the stress versus stretch relationship. Differences in the stretch energy beneath the stress-stretch curves were different for the circumferential and radial specimen axes due to the relatively higher distensibility of the radial axis. The slight differences in the areas beneath the loading and unloading curves for the 0.1 second loading time were not significant, and furthermore, could have been a reflection of the hysteresis of the load cells themselves which was specified as 0.5 percent.

#### 4.4 STRESS-RELAXATION

The stress-relaxation exhibited in the MVAL was consistent with findings for other collagenous soft tissues [47, 48, 50, 61, 62] including findings for the MV chordae tendineae [40]. However, due to the relatively large change in membrane tension that corresponded to extremely small changes in stretch on both axes near the 90 N/m equitension level (i.e. high stiffness), further analysis of the results is necessary. The main goal of this analysis is to show that the observed stress-relaxation was real and was not an artifact caused by small changes in the specimen attachments (i.e. specimen sutures pulling out slightly from the specimen edges) that could cause minute reductions in the specimen stretches. To do this, the change in stretch observed over the three hour duration of the biaxial stress-relaxation experiments was compared to the change in stretch observed in the unloading phase of the final preconditioning cycle for the same specimens from the peak membrane tension to the same membrane tension observed after the three hour duration of the stress-relaxation experiments (Figure 52).

The results of this analysis showed that the specimen stretches for the relaxation experiments were markedly different from those seen in the quasi-static unloading cycles. Specimen stretches observed in the relaxation experiments were statistically different from those observed in the quasi-static unloading cycles in both the circumferential ( $p=0.02$ ) and radial ( $p<0.01$ ) directions. As expected, the quasi-static results showed a negative change, or decrease in stretch to reach the relaxed membrane tension. Conversely, the stretches over the duration of the stress-relaxation experiment actually increased slightly. The increase in stretch was quite small, however it did occur in all but one specimen.

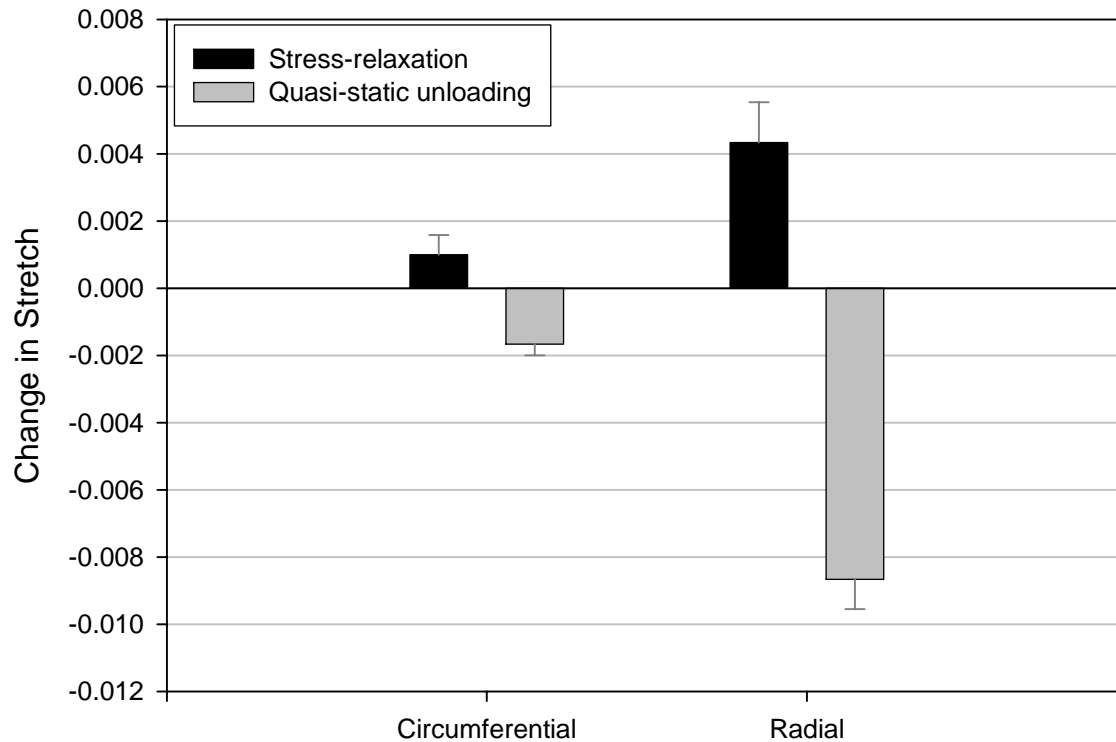


**Figure 52. Changes in stretch over the three hour duration of the stress relaxation experiments compared to the changes in stretch required to reach the same membrane tension in quasi-static unloading cycle.**

The increased stretches over the stress-relaxation duration indicate that a portion of the total specimen stretch may be redistributed into the central marker region as the specimen relaxes. For comparison, a similar analysis was done using the uniaxial stress-relaxation and quasi-static unloading data. As seen in the biaxial analysis, stretch levels for specimen axes

under tension increased over the duration of the stress-relaxation tests, while the quasi-static unloading cycles showed decreased stretch levels for the equivalent relaxed membrane tension state. Interestingly, the stretches on the unloaded axes in the stress-relaxation experiments all decreased (Figure 53) over the duration of the stress-relaxation experiments. This result was expected due to the mechanical coupling between specimen axes, however, and also showed that the stretch measurement system was not biased towards positive changes in stretch in the stress-relaxation experiments. The changes in stretch observed, while extremely small, were within the capabilities of the optical measurement system which was able to calculate stretches to within 0.001 (see RESULTS).

This result underscores the importance of performing biaxial experiments on membranous tissues. The difference between the change of stretch of the free and loaded axes indicates that the mechanism of relaxation may be different in uniaxial and biaxial experiments. In uniaxial experiments increases in stretch level on the loaded axis may be due to time-dependent Poisson-like effects minimizing the areal tissue stretch, while this cannot be the case in biaxial experiments since the stretch on both axes increases. In biaxial experiments, the observed relaxation was greater in the radial direction than the circumferential direction. This discrepancy may be linked to the higher distensibility of the MVAL in the radial direction; in order to achieve the desired 90 N/m equitension state, the required stretches in the radial direction were generally approximately 3 times greater than those required in the circumferential direction.

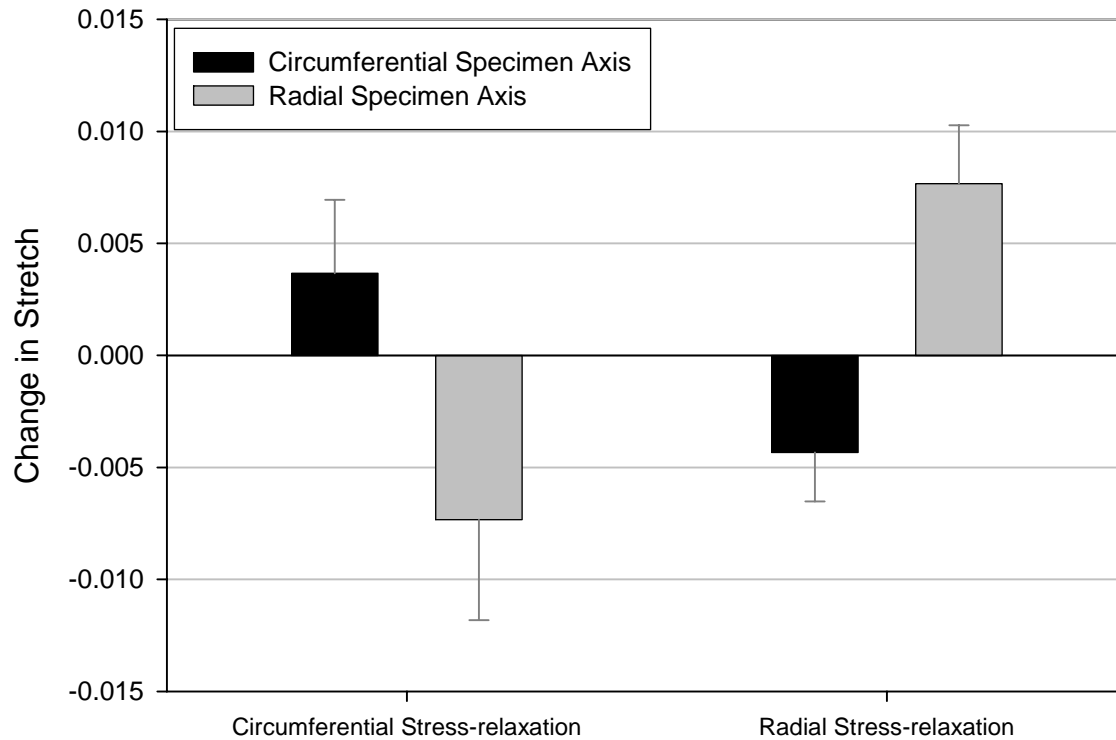


**Figure 53. In uniaxial stress-relaxation experiments, stretch levels increased for axes under tension and decreased on the free axis. Data presented as mean  $\pm$  SEM.**

In their study on ligament viscoelasticity, Provenzano et al [47] found that the uniaxial relaxation of the rat medial collateral ligament (MCL) was highly dependent on stretch level. However, in contrast to our findings, the observed relaxation decreased as the initial stretch level increased. Additionally, the results of Provenzano et al showed that the influence of stretch level on the relaxation behavior diminished after stretch levels increased to a level beyond the transition phase generally attributed to collagen recruitment in collagenous soft tissues; as shown in our earlier work the 90 N/m equitension state was achieved in the MVAL well after this

transition phase. In accord with this finding, Lee et al [46] observed that the amount of relaxation in the glutaraldehyde-stabilized porcine aortic valve leaflet was independent of initial load. Interestingly, this study noted relaxation differences between specimens tested in uniaxial tension in the circumferential and radial directions, but these differences were opposite to our findings, possibly due to the large amount of collagen cross-linking that resulted from the glutaraldehyde treatment. In contrast to the studies by Provenzano and Lee, a study by Dunn and Silver [48] reported increased relaxation levels in several soft tissues, including parietal pericardium, with increased stretch level. However, comparisons with this study are less direct since relaxations were calculated at 5% sequential stretch increments without returning to the original unloaded stretch state between relaxations. Another factor that could potentially play a role in the relaxation behavior observed in our study is the stretch rate differences between specimen axes. Due to the relatively greater stretch required to load the MVAL to the 90 N/m membrane tension in the radial direction and the fact that the rise times for the circumferential and radial axes were the same, the stretch rate in the radial direction was necessarily higher than that observed in the circumferential direction. In their study on the uniaxial relaxation behavior of porcine aortic valve (AV) cusps [50], Vesely et al observed that the relaxation percentage and the rate of relaxation were dependent on stretch rate. However, in this case, the relaxation of the AV decreased as the displacement rate in the initial loading phase increased. Although the results of Provenzano and Vesely seem contradictory to our results, these comparisons should be interpreted with caution since these studies reported the effects of stretch and stretch rate on a single specimen axis under uniaxial load. Because our result describes differences between two axes of the same specimen, the structural differences between specimen axes must also be considered.

Previous Small Angle Light Scattering studies [32] have shown that the leaflet subsection used in our experiments consists predominantly of circumferentially oriented fibers. This suggests that a larger portion of the 90 N/m membrane tension was borne by collagen fibers in the circumferential direction than in the radial direction since collagen most effectively resists axial loads. In their uniaxial stress relaxation study on the porcine MV chordae tendineae [40], Liao and Vesely linked decreases in relaxation rate and relaxation percentage to increased GAG content, hypothesizing that interfibrillar GAG linkages decreased relaxation by resisting shearing between collagen fibers. Using our result, we may expand on this hypothesis to state that, for the MVAL, the increased relaxation in the radial direction may be due to the fact that a relatively larger percentage of the total stress on the radial axis is borne by the GAGs, suggesting that interfibrillar GAG connections may preferentially resist shearing forces between individual fibrils, related to circumferential relaxation in the MVAL, and may be weaker when stressed orthogonally to the preferred collagen orientation, as they would be in response to radial stretch. Additional support for this idea may be supplied by our uniaxial stress-relaxation data. In the uniaxial case we observed significantly less radial relaxation than was observed for the biaxial relaxation protocols. This may be due to the fact that fiber rotations were not restricted in the uniaxial experiments allowing fibers to reorient themselves in a direction more parallel to the loaded specimen axis. This fibrillar reorientation would also reorient the proteoglycan linkages allowing them to resist shearing relaxations. Another hypothesis is that the GAG resistance to relaxation is not directionally dependent at all, but instead is dependent on areal stretch level. If this is the case, uniaxial stress-relaxation may not be as sensitive to stretch level because the free dimension may contract as the tissue is loaded, effectively minimizing the areal stretch. In either

case it is clear that the proper biaxial loading condition is critical when evaluating the physiologically functional viscoelastic properties of soft tissues.

#### **4.5 CREEP**

The results of our creep experiments showed that, despite the observed relaxation behavior, the MVAL did not exhibit a functionally significant degree of creep. The small amount of creep that was observed over the three hour time period was statistically insignificant for all time points except 3 hours on the radial specimen axis only. However, creep at this distant time point is irrelevant to the physiologic loading cycle of the valve, which occurs over approximately 0.5 seconds during ventricular systole. The lack of creep observed in the MVAL was inconsistent with previous findings for ligament [47, 49], pericardium [62] and AV leaflet [46], which all exhibited a much greater degree of creep than that observed in the MVAL. It should be noted again, that these experiments were all performed under uniaxial tension and that it is unclear whether the differences observed in our creep experiments are due to material differences or due to differences in loading condition.

#### **4.6 RELATIONSHIP OF STRESS-RELAXATION AND CREEP**

The presence of disproportionate degrees of creep and relaxation behavior has been observed, although to a lesser degree than was observed in this study, previously. Provenzano et al observed that the rate of relaxation proceeded faster than the rate of creep in contralateral ligaments, while Thornton et al reported a similar finding and showed that ligament creep could not be predicted from relaxation data using quasilinear viscoelastic assumptions [49]. In contrast to our study, in which the observed behavior occurred after stretching the MVAL through the transition phase of the stress-stretch relationship, Thornton et al observed this relaxation-creep imbalance at low stress and were able to properly relate creep and relaxation by incorporating fiber recruitment. Our findings suggest that the mechanisms responsible for creep and relaxation in the MVAL may be functionally independent.

#### 4.7 COMPARISONS TO SMALL ANGLE X-RAY SCATTERING RESULTS

Recent small angle x-ray scattering studies (SAXS) [63], also from the University of Pittsburgh by Liao et al may shed some light on the microstructural mechanisms responsible for the behavior observed in this study. For quasi-static loading of the MVAL, SAXS results (Figure 54) show that the D-spacing (see INTRODUCTION on collagen structure) of the collagen molecules does not increase until the specimen has been stretched into the stress-stretch transition zone and collagen fiber uncrimping has been initiated. This suggests that components other than collagen itself are primarily responsible for bearing specimen loads at low stretch levels.

In addition to dynamic loading, this study included SAXS analysis of biaxial creep (Figure 55) and stress-relaxation behavior (Figure 56). Our finding that the MVAL did not creep was supported by this SAXS study, which also found no appreciable creep in the MVAL over a one hour test duration. The SAXS creep results show that the collagen D-spacing does not change, as would be expected since the specimen does not deform. The SAXS stress-relaxation results, like our stress-relaxation results, are somewhat paradoxical. These results showed relaxation behavior similar to that observed in our biaxial study, but showed that the collagen D-spacing diminished extensively during relaxation. This suggests that the mechanism of stress-relaxation may depend on a non-collagenous component of the MVAL microstructure such as elastin or GAGs.

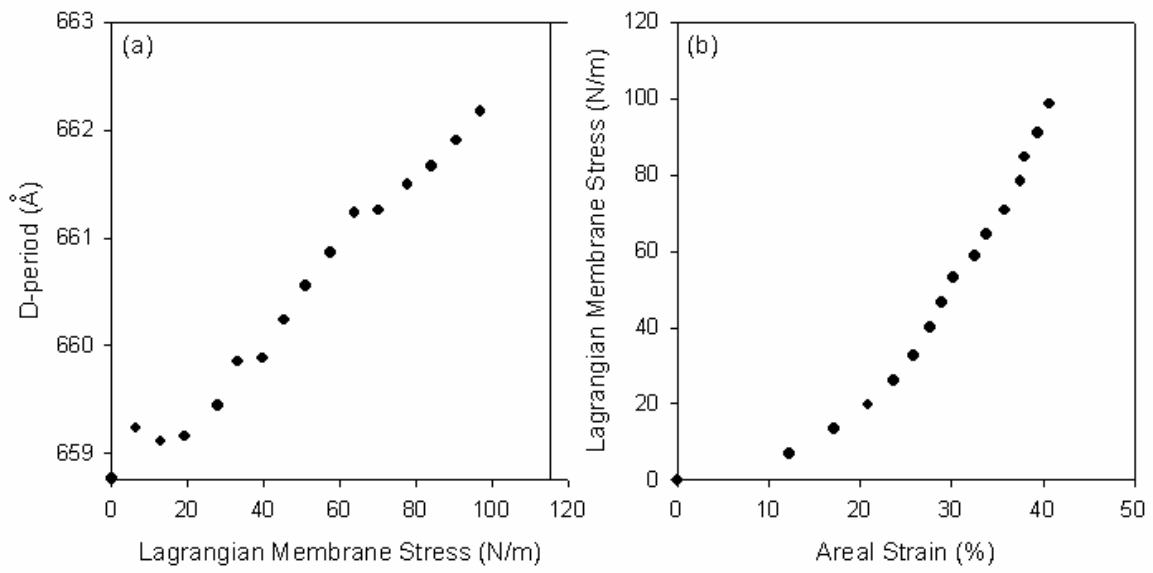


**Figure 54. Changes in collagen D-spacing as a function of membrane tension (left). Membrane tension versus areal stretch % for the same MVAL specimen. Reproduced from Liao, J. Unpublished Communication.**

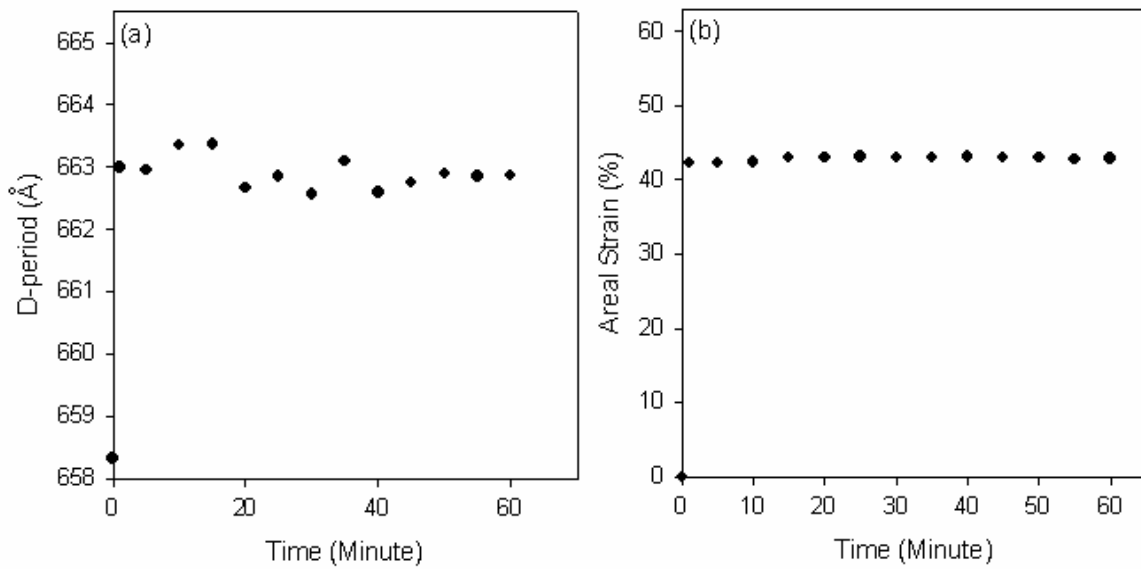


**Figure 55. D-spacing as a function of creep experiment duration (left). Areal stretch as a function of creep test duration for the same specimen (right). Reproduced from Liao, J. Unpublished Communication.**

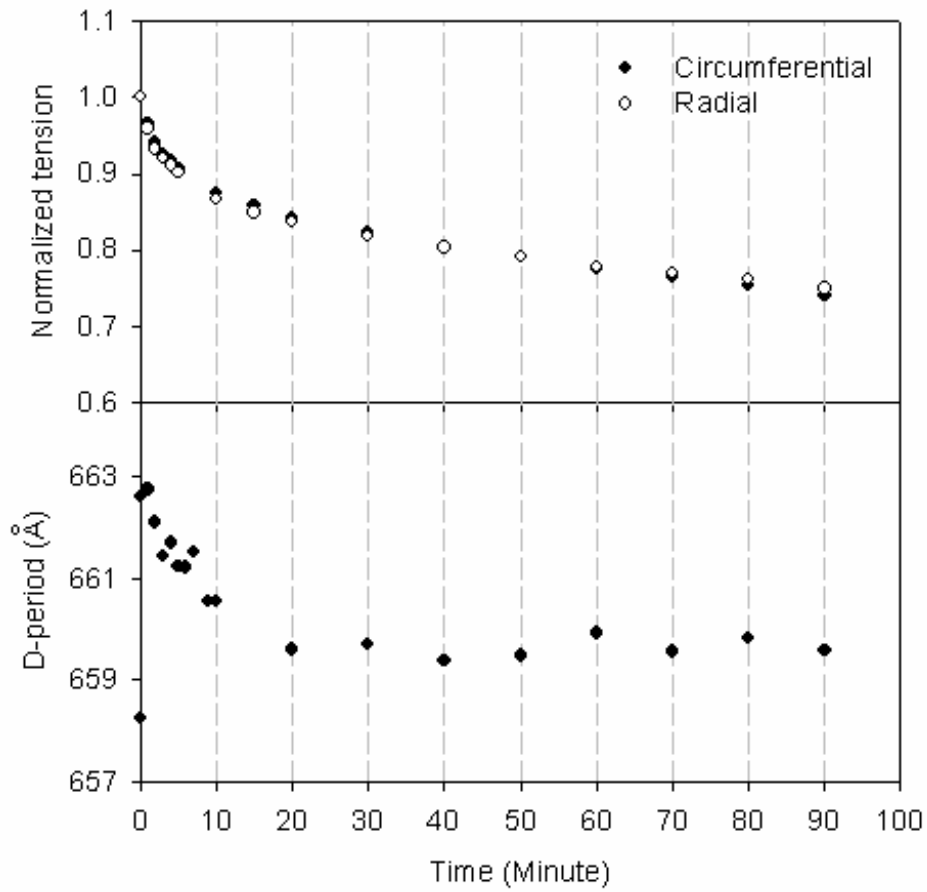


**Figure 56. Normalized membrane tension versus stress-relaxation test duration (top). Collagen D-spacing as a function of stress-relaxation test duration for the same specimen (bottom). Reproduced from Liao, J. Unpublished Communication.**

## 4.8 STUDY LIMITATIONS

One limitation of this study was the optical stretch measurement system. This system could only track four or nine markers in the central belly region of the leaflet. A more thorough analysis of the stretch state, in the entire specimen would provide insight into both the stress-relaxation and creep mechanisms. In addition to the stretch measurement system, the actuation components provided some study limits. While these actuation components provided a major improvement over previous biaxial testing devices, the component stability at the extremely high speeds necessary for the 0.05 second loading/unloading cycles was not sufficient.

In addition to limits of the device itself, in the current study it was assumed that the mechanical properties of the MVAL leaflet were dominated by its passive structural elements: collagen, elastin, and polysaccharides, which constitute 85-95% of the leaflet dry wt [64, 65]. No attempt was made to maintain cell viability within any of the test samples nor was there any effort to trigger an active response from the leaflet with an appropriate chemical stimulus. It was recently demonstrated in flexure that native aortic valve interstitial cells can contribute to leaflet stiffness [66]. However, the forces generated here are at several orders of magnitude lower than those experienced by the MVAL ECM components. However, changes in leaflet deformation in an in-situ preparation [8] suggest some contribution by the leaflet cells. While additional work in this is required to clarify issue, it is unlikely that cellular forces contribute substantially to the MVAL mechanical response. We note finally that only equitension protocols were performed in the present study. However, given the close agreement with normal physiologic stretches, this should be sufficient for characterizing the physiologically relevant viscoelastic properties of the MVAL.

## 4.9 CONCLUSIONS

The results of this study highlight the need to perform creep tests on soft tissues. Although, generally more difficult to perform, creep experiments are more representative of the physiologic conditions of most soft tissues, and as demonstrated by our results, creep behavior may be radically different from relaxation behavior. Furthermore, our results underscore the importance of performing mechanical tests on soft tissues using the appropriate loading condition, which, in the case of membranous soft tissues, usually consists of a biaxial loading state.

This study has provided insight into the dynamic mechanical properties of the MVAL. The combination of the stretch rate insensitivity of the stress level observed within the leaflet, the lack of an appreciable level of tissue hysteresis at physiologic stretch rates, and the lack of creep implies that the MVAL may be functionally modeled as a nonlinear quasi-elastic anisotropic biological material. The structural basis for this behavior is as yet unknown, but is likely an important functional aspect of native MV tissues and warrants further study. Also, additional studies using small angle X-ray scattering on MV leaflet collagen molecular structure under creep and relaxation, as done for recently for pericardium [63], may help to provide a structural basis for the mechanical behavior observed in this study.

#### **4.10 RECOMMENDATIONS FOR FUTURE STUDY**

The results of this study have provided novel and important data on the MVAL, but much remains to be studied before our understanding of mitral mechanics is complete. Recommended future studies include:

**1. A duplication of the current study for the posterior mitral valve leaflet.**

- This study would provide necessary data for the modeling of the posterior leaflet and would elucidate differences between the two leaflets.

**2. Stress-relaxation study of the MV leaflet using a high resolution camera and magnifying lens.**

- By studying the changes in the stretch state of all regions of the leaflet (as opposed to only the central region used in the current study) the details of the paradoxical stress-relaxation behavior may be further explored.

### **3. Creep experiments on the MV chordae tendineae.**

- Current studies of the MV chordae tendineae include only dynamic loading and stress-relaxation. Since it may be more representative of the physiological condition, creep experiments on the MV chordae tendineae may provide useful data.

## 5.0 THESIS SUMMARY

The list below summarizes the major findings of this study for the MVAL:

1. Dynamic biaxial loading and unloading cycles revealed that the stress-stretch relationship of the MVAL showed no dependence on stretch rate and indicated that the MVAL tissue may be functionally modeled as an anisotropic quasi-elastic material.
2. Creep experiments revealed that creep in the MVAL at a physiological load state was functionally insignificant, particularly when considered with respect to physiological creep duration of approximately 0.5 seconds.
3. Although the MVAL showed no creep, stress-relaxation experiments showed significant relaxation from the physiological loading state. This result underscored the necessity of performing creep experiments on soft tissues since creep may be more representative of the physiological loading condition and cannot be satisfactorily described using stress-relaxation data.

## **APPENDIX A**

### **REDUCED RELAXATION FUNCTION FIT PARAMETERS**

	CIRC				RAD			
Sample	C	T1	T2	R^2	C	T1	T2	R^2
<b>Biaxial</b>								
1	2.13E-02	1.06E-02	1.00E+08	9.82E-01	5.93E-02	8.92E-01	2.33E+07	9.98E-01
2	2.62E-02	1.05E-02	1.04E+08	9.90E-01	1.15E-01	1.20E+00	7.48E+08	1.00E+00
3	3.22E-02	1.27E-02	7.91E+07	9.91E-01	1.22E-01	5.70E-01	1.51E+09	9.98E-01
4	3.00E-02	1.20E-02	9.72E+07	9.95E-01	5.97E-02	3.51E+00	1.22E+06	9.99E-01
5	2.09E-02	1.00E-02	9.45E+07	9.87E-01	8.25E-02	3.52E+00	2.37E+07	9.97E-01
6	4.25E-02	1.18E-01	7.87E+07	9.91E-01	1.31E-01	5.28E+00	6.87E+07	9.98E-01
7	5.88E-02	1.47E+00	7.91E+07	9.99E-01	1.46E-01	8.07E+00	1.88E+08	1.00E+00
8	2.25E-02	1.02E-02	1.00E+08	9.80E-01	9.92E-02	4.85E+00	9.30E+07	9.98E-01
Mean	3.18E-02	2.06E-01	9.17E+07	9.89E-01	1.02E-01	3.49E+00	3.32E+08	9.98E-01
SEM	4.61E-03	1.80E-01	3.83E+06	2.23E-03	1.14E-02	9.12E-01	1.89E+08	3.73E-04
<b>Uniaxial (Circumferential)</b>								
1	2.01E-02	1.03E-02	1.00E+08	9.78E-01				
2	2.71E-02	1.02E-02	1.00E+08	9.97E-01				
3	6.64E-02	6.37E+00	2.35E+06	9.98E-01				
Mean	3.79E-02	2.13E+00	6.76E+07	9.91E-01				
SEM	1.44E-02	2.12E+00	3.26E+07	6.31E-03				
<b>Uniaxial (Radial)</b>								
1					3.59E-02	1.35E-02	8.03E+07	9.89E-01
2					1.08E-01	3.58E+00	2.76E+08	1.00E+00
3					4.36E-02	4.26E-01	3.10E+08	9.89E-01
Mean					6.24E-02	1.34E+00	2.22E+08	9.92E-01
SEM					2.28E-02	1.12E+00	7.15E+07	3.66E-03

**APPENDIX B**

**BIAXIAL TESTING DEVICE USER'S MANUAL**

# Biaxial Testing Manual

*Author(s): Jonathan Grashow*

*Version: 1.1*

*Original Release Date: 3/17/05*

*Last Revision Date: 3/24/05*

# Contents

**Section 1:** Background material

**Section 2:** Biaxial Tester Description

**Section 3:** Biaxial Testing Software Screens

3.1: Load Cell Calibration Screen

3.2: Image Setup Screen

3.3: Specimen Positioning Screen

3.4: Test Settings Screen (Load Control)

3.5: Test Settings Screen (Stretch Control)

3.6: Run Test Screen

**Section 4:** Biaxial Testing Protocols

4.1: General Notes

4.2: Setting Up the Biaxial Testing Device

4.3: Preparing the Specimen

4.4: Mounting the Specimen in the Biaxial Testing Device

4.5: Setting Up the Imaging System

4.6: Setting a Preload

4.7: Running a Test

**Section 5:** Biaxial Tester Output Files

**Section 6:** Software, Drivers & Virtual Channels

**Section 7:** System Diagrams

7.1: System Overview

7.2: System Orientation

7.3: Motor Wiring Diagram

7.4: Load Cell Wiring Diagram

7.5: Software Overview

**Section 8:** System Specifications

## **Section 1: Background Material**

Biaxial testing and analysis is a complicated and delicate process. The following articles are strongly suggested for anyone planning to perform biaxial experiments:

### ***For General Information on Biaxial Testing:***

1. [Sacks MS, Sun W.](#) Multiaxial mechanical behavior of biological materials. Annu Rev Biomed Eng. 2003;5:251-84. Epub 2003 Apr 18. Review.
2. [Sacks MS.](#) A method for planar biaxial mechanical testing that includes in-plane shear. J Biomech Eng. 1999 Oct;121(5):551-5.

### ***For Information on Optical Stretch Measurement Technique:***

1. [Hoffman AH, Grigg P.](#) A method for measuring stretches in soft tissue. J Biomech. 1984;17(10):795-800.

### ***For Examples of Biaxial Experiments:***

2. [Gloeckner DC, Sacks MS, Fraser MO, Somogyi GT, de Groat WC, Chancellor MB.](#) Passive biaxial mechanical properties of the rat bladder wall after spinal cord injury. J Urol. 2002 May;167(5):2247-52.
3. [Billiar KL, Sacks MS.](#) Biaxial mechanical properties of the natural and glutaraldehyde treated aortic valve cusp--Part I: Experimental results. J Biomech Eng. 2000 Feb;122(1):23-30.
4. [Wells SM, Sacks MS.](#) Effects of fixation pressure on the biaxial mechanical behavior of porcine bioprosthetic heart valves with long-term cyclic loading. Biomaterials. 2002 Jun;23(11):2389-99.

### ***For Examples of High-Speed Biaxial Experiments:***

1. [Nagatomi J, Gloeckner DC, Chancellor MB, DeGroat WC, Sacks MS.](#) Changes in the biaxial viscoelastic response of the urinary bladder following spinal cord injury. Ann Biomed Eng. 2004 Oct;32(10):1409-19.

## Section 2: Biaxial Tester Description

Figure 1

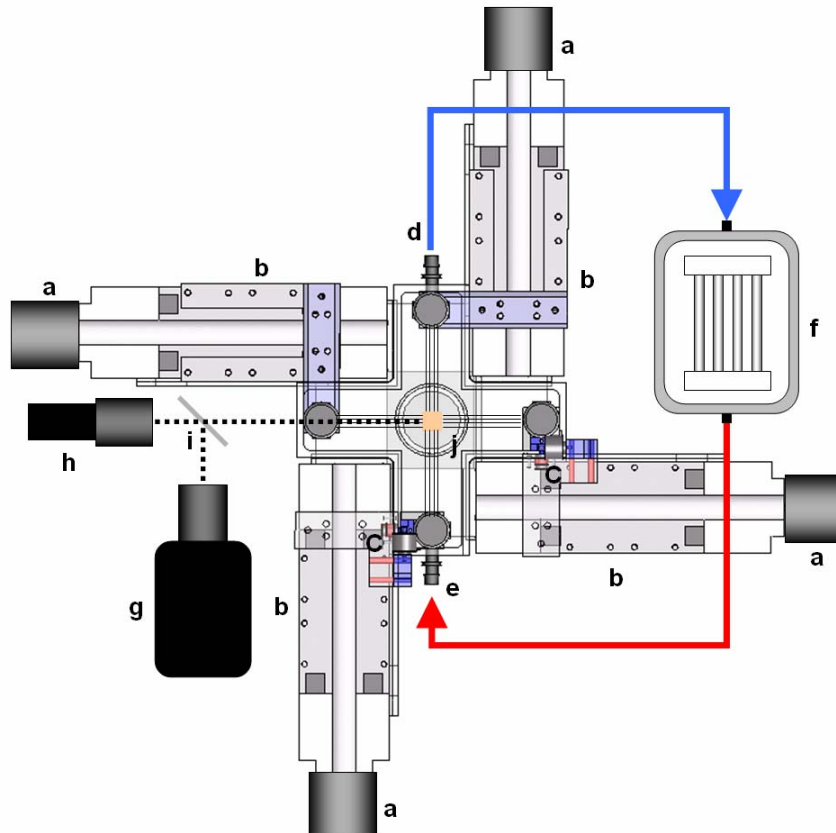


*Figure 1. Overhead schematic of the high speed biaxial testing device; a) stepper motors; b) screw-driven linear actuators; c) load cells; d) specimen bath outlet; e) specimen bath inlet; f) heating element maintained bath temperature at 37°C; g) high speed digital camera (high speed systems only); h) standard digital camera; i) beam splitter (high speed systems only); j) sub specimen mirror.*

The actuation components of the biaxial testing device (Fig. 1) are four ball-screw driven linear positioners (404XR, Parker Hannafin Corp., Irwin, PA). Each of these linear positioners is equipped with a 20mm lead capable of achieving a maximum carriage velocity of 1 m/s and maximum carriage acceleration of 25 m/s<sup>2</sup>. These four linear positioners are mounted in an opposing fashion such that one pair of positioners is aligned to stretch a

centered tissue sample along each device axis. Each linear positioner is driven by a rotary stepper motor (OS22B-SNL10, Parker Hannafin Corp., Irwin, PA) and each stepper motor is controlled with a microstepping drive (E-AC, Parker Hannafin Corp., Irwin, PA) that provides a step resolution of 50,800 steps per revolution, which, when coupled to each aforementioned linear positioner results in a spatial resolution of approximately 0.394  $\mu\text{m}$  for each positioner carriage. All the microstepping drives are controlled via a 4-axis PCI motion controller card (DMC 1740, Galil Motion Control Inc., Rocklin, CA) that is installed in the device control PC (Precision 550, Dell Inc., Round Rock, TX).

Custom attachment arms are mounted onto the carriage of each linear positioner in order to provide a mechanism for specimen attachment. Leaflet specimens are mounted to these attachment arms in a trampoline fashion by attaching two loops of 000 nylon suture to each side of the specimen via four stainless steel surgical staples (see specimen mounting procedure). The attachment arms are designed to fasten the two specimen suture loops and to transmit the total load applied by each actuator evenly through all of the attached suture lines. To accomplish this, each attachment arm is furnished with a pair of custom stainless steel pulleys which are free to rotate, ensuring that the forces applied through each pulley are balanced between both of the surgical staple attachments for the attached suture loop. Both pulleys are mounted symmetrically on either side of a central stainless steel ball bearing.

This mechanism distributes the total force applied by the positioner equally between both pulleys.

Leaflet deformations are measured optically with a digital camera (see background material for references on biaxial stretch measurement). Load measurements are acquired by the device control computer from a pair (one on each device axis) of load cells (Model 31, Honeywell Sensotec, Columbus, OH) via an analog/digital converter (PCI-6036E, National Instruments, Austin, TX).

## Section 3: Biaxial Testing Software Screens

### 3.1 – Load Cell Calibration

The screenshot displays the 'Load Control 4.0.vi' software interface. The 'Load Cells' tab is active, showing two graphs and associated data. The 'Load Cell Voltages' graph shows a blue line fluctuating around a horizontal red line at approximately 3.95. Below the graph, 'Voltage 1' is 3.991 and 'Voltage 2' is 3.930. The 'Loads' graph shows a blue line fluctuating around a horizontal red line at approximately 0.53. Below the graph, 'Load 1' is 0.533 g and 'Load 2' is 0.532 g. The 'Calibration Load Units' section shows 'Grams (g)' selected, with X-axis settings of Low: 0.00 g and High: 116.50 g, and Y-axis settings of Low: 0.00 g and High: 116.50 g. At the bottom, there are 'Save' and 'Load' buttons for the calibration file. The 'Program Status' bar shows 'Loading Specimen' and a 'Stop Program' button. Red arrows point to the following features:

- 1.1 Load Cell Tab
- 1.2 Load Cell Voltage Readings
- 1.3 Low & High Indicators
- 1.4 Loads Graph
- 1.5 Save Button
- 1.6 Load Button

### 3.2 – Image Setup

The screenshot displays the 'Load Control 4.0.vi' software interface. The 'Imaging' tab is selected, showing the 'Image Setup' section with seven numbered options: 1. Threshold Image (slider 0-255), 2. Number of Markers (9 and 4), 3. Initialize Marker Subregions (Initialize button), 4. Marker Color (Dark/Light), 5. Turn on Marker Tracking (checkbox), 6. Define Marker Size (slider 0-5000), and 7. Lock Subregions (checkbox). Below this is the 'Marker Positions' section, which includes a graph showing marker positions on a grid (0.0 to 1024.0 on the x-axis, 0.0 to 768.0 on the y-axis) and a list of reference settings: Current, Non-sutured, Free Floating, Preloaded, Reference 1, Reference 2, Reference 3, and Reference 4, each with a 'Set' button. At the bottom of the graph area are 'Save Reference File' and 'Compare References' buttons. The 'Program Status' section at the bottom shows 'Loading Specimen' and a 'Stop Program' button. On the right side, there are two 'spe' indicators, one showing '6.95'. Red arrows point from labels on the right to specific elements in the interface.

2.1 Imaging Tab

2.2 Image Setup

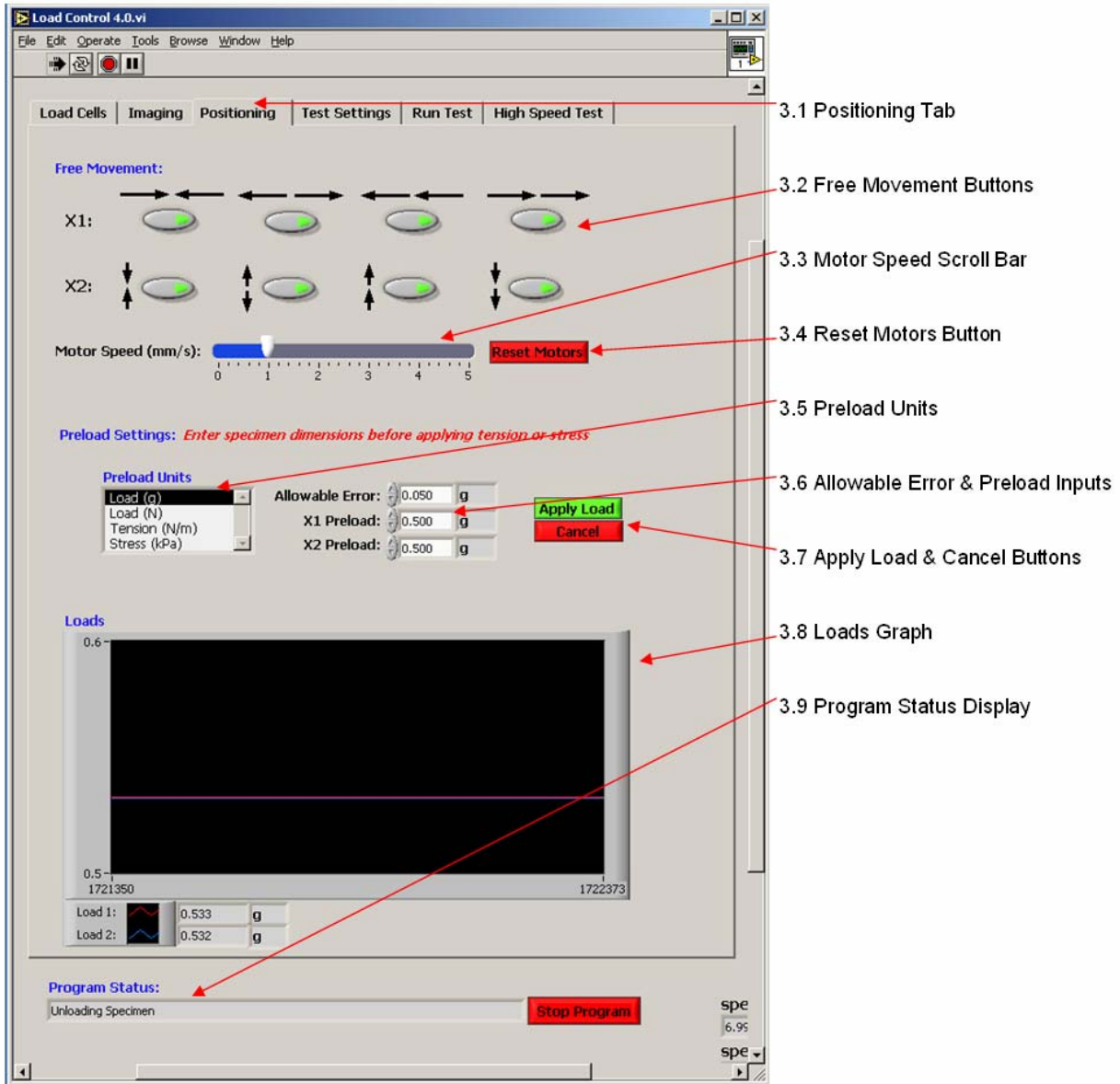
2.3 Marker Positions Graph

2.4 Set References

2.5 Save Reference File

2.6 Compare References

### 3.3 – Specimen Positioning



### 3.4 – Test Settings (Load Control)

The screenshot shows the 'Load Control 4.0.vi' software interface. The 'Test Settings' tab is selected. The interface is organized into several sections with corresponding callouts:

- 4.1 Test Settings Tab:** Points to the 'Test Settings' tab in the top navigation bar.
- 4.2 Specimen Dimension Inputs:** Points to the 'Specimen Dimensions' section, which includes 'X1 Length (mm): 10.00', 'X2 Length (mm): 10.00', and 'Thickness (mm): 0.58'.
- 4.3 Cycle Settings:** Points to the 'Cycle Settings' section, which includes 'Number of Cycles: 1' and '1/2 Cycle Time (s): 600.0'.
- 4.4 Stretch Limits:** Points to the 'Stretch Limits' section, which includes 'Stretch Limit 1: 3.0000' and 'Stretch Limit 2: 3.0000'.
- 4.5 Load Units:** Points to the 'Max Loads' dropdown menu, which is currently set to 'Load Control (g)'. Other options include 'Load Control (N)', 'Tension Control (N/m)', and 'Stress Control (kPa)'.
- 4.6 Test Loads:** Points to the 'Axis 1' and 'Axis 2' input fields, both set to '59.0000 g'.
- 4.7 Stretch Estimate Inputs:** Points to the 'Initial Stretch Estimates' section, which includes 'Stretch 1: 1.1100' and 'Stretch 2: 1.0900'.
- 4.8 Correction Gain Input:** Points to the 'Carriage Displacement Correction Mode' section, which includes 'Correction Gain: 0.50'.
- 4.9 File Settings Display:** Points to the 'File Settings' section, which includes 'Test Name' and 'Reference File' fields.

At the bottom of the interface, the 'Program Status' shows 'Unloading Specimen' and a 'Stop Program' button. The status bar at the bottom right displays 'spe' and '6.95'.

### 3.5 – Test Settings (Stretch Control)

The screenshot shows the 'Stretch Control 1.0.vi' software interface. At the top, there is a menu bar (File, Edit, Operate, Tools, Browse, Window, Help) and a toolbar with icons for navigation and execution. Below the toolbar is a tabbed interface with five tabs: 'Load Cells', 'Imaging', 'Positioning', 'Test Settings', and 'Run Test'. The 'Test Settings' tab is selected. The interface is divided into several sections, each with a blue header:

- Specimen Dimensions:** Contains three numeric input fields: 'X1 Length (mm):' (0.00), 'X2 Length (mm):' (0.00), and 'Thickness (mm):' (0.00).
- Cycle Settings:** Contains two numeric input fields: 'Number of Cycles:' (0) and '1/2 Cycle Time (s):' (0.00).
- Stretch Ratio Settings:** Contains a 'Stretch Ratio:' label and a mathematical expression:  $\frac{(\text{Stretch 1})-1}{(\text{Stretch 2})-1} = \frac{0.0000}{0.0000}$ .
- Load Settings:** Contains a checkbox 'Use Load Limits For This Test' (unchecked), a 'Max Loads:' dropdown menu (set to 'Load Control (g)'), and two numeric input fields: 'Axis 1:' (0.0000) and 'Axis 2:' (0.0000).
- Stretches:** Contains a checkbox 'Use Stretch Limits For This Test' (unchecked) and two numeric input fields: 'Stretch 1:' (0.0000) and 'Stretch 2:' (0.0000).
- Carriage Displacement Correction Mode:** Contains a numeric input field 'Correction Gain:' (0.00).
- File Settings (You will be prompted to enter these when you start a test):** Contains two text input fields: 'Test Name:' and 'Reference File:'.

At the bottom of the interface, there is a 'Program Status:' label and a red 'Stop Program' button.

Red arrows point from the following labels on the right to specific elements in the interface:

- 5.1 Test Settings Tab
- 5.2 Specimen Dimension Inputs
- 5.3 Cycle Settings
- 5.4 Stretch Ratio Settings
- 5.5 Load Settings
- 5.6 Test Load Limits
- 5.7 Stretch Settings
- 5.8 Correction Gain Input
- 5.9 File Settings Display

### 3.6 – Running a Test

The screenshot shows the 'Load Control 4.0.vi' software interface. At the top, there are tabs for 'Load Cells', 'Imaging', 'Positioning', 'Test Settings', 'Run Test', and 'High Speed Test'. Below the tabs are three buttons: 'Start Test' (green), 'Cancel Test' (red), and 'Update Image' (blue). To the right of these buttons is a 'Display:' label with a radio button set to 'Current Cycle Only' and another radio button for 'All Cycles'. The main area contains three graphs: 'Stretch vs Time (ms)', 'Loads (g) vs Time (ms)', and 'Load (g) vs Stretch'. The 'Stretch vs Time' graph shows two curves (red and blue) increasing over time. The 'Loads vs Time' graph shows two curves (red and blue) peaking around 600,000 ms. The 'Load vs Stretch' graph shows two curves (red and blue) increasing with stretch. To the right of the graphs are two small displays for 'Current Cycle' (1) and 'Acquisition Rate' (6 Hz). At the bottom, there is a 'Program Status' section showing 'Unloading Specimen' and a 'Stop Program' button. The interface also includes a 'Shear Angle' display set to -1.50 degrees and a 'Current Cycle Display' showing 37.697 g and 46.103 g. The 'Image-Load Alias' is set to 0 ms.

- 6.1 Run Test Tab
- 6.2 Cycle Display Toggle
- 6.3 Start Test, Cancel Test, and Update Image Buttons
- 6.4 Stretch Graph
- 6.5 Shear Angle Display
- 6.6 Loads Graph
- 6.7 Loads vs Stretches Graph
- 6.8 Current Cycle Display
- 6.9 Acquisition Rate Display
- 6.10 Image-Load Alias Display

## **Section 4: Biaxial Testing Protocols**

### **4.1 - General Notes**

1. The program can be run by pressing the LabView arrow in the upper left corner of the program window.
2. In order to properly shutdown the program, press the "Stop Program" button at the bottom of the screen while the program is in an idle state.
3. In case of an emergency, turn off power to the motors and stop the program by clicking the LabView arrow in the upper left corner of the program window.
4. Throughout the manual gray numbers in parentheses: (X.X) correspond to labels in the Biax Software Screens section.

## 4.2 - Setting up the Biaxial Testing Device

### Notes:

1. This protocol assumes that the device is properly installed and affixed to the testing tabletop.
2. During this protocol, care should be taken to limit contact and forces applied to the load cells. Applying forces greater than 150% of full scale to the load cells will result in permanent damage.
3. Caution should always be used around the biaxial testing device. Limit switches are in place to prevent the device from damaging itself, not you.
4. Power to the motors may be turned off to allow the device carriages to be moved manually. Power to the motors must be restored before setting either the low or high calibration points.

### Protocol:

1. Turn on power to all components: computer, motors, light, load cells, and camera.
2. Turn on device computer
3. Launch Biax software
  - a. Load Control 1.0 (load based test)
  - b. Stretch Control 1.0 (stretch based test)
4. Click on the "Load Cell" tab (1.1) at the top of the screen
5. Perform steps 6-10 independently on each load cell
6. Check to make sure that nothing is touching the load cell, and proceed to adjust the zero for each load cell within the inline amplifier until the voltage (1.2) for the cell reads ~0.
7. Using the calibration arm, hang a weight and adjust the load cell gain within the amplifier (See amplifier manual for details) such that the span of the load cell output voltage is maximized for the load range for your test.
  - a. If it is necessary, it is possible to mechanically amplify the load signal by mounting the load cell closer to the carriage arm pivot. Rough

amplifications are (from upper to lower mounting position): 1:1, 1.14:1, 1.33:1, 1.6:1

8. With no force on the load cell, check to make sure that 0 is entered next to the "low" indicator (1.3) for the appropriate axis and click the "set" button.
9. Hang an appropriate weight from the calibration arm, enter the weight next to the "high" indicator (1.3) for the appropriate axis and click the "set" button.
10. Repeat steps 8 and 9 until the loads displayed in the "Loads" graph (1.4) are correct and repeatable.
11. Click the "Save" button (1.5) to save the calibration file. If you choose not to save the calibration file and the computer crashes or freezes, you will have to repeat the load cell calibration.
  - a. You can reload any calibration file by click the "Load" button (1.6) and selecting the desired calibration file.

### 4.3 - Preparing the Specimen

#### Notes:

1. The biaxial tester is designed to test specimens that range in size from 0.7 x 0.7cm to 4.0 x 4.0 cm
2. Specimens should be properly hydrated throughout preparation procedure by submerging them in the appropriate fluid as needed

#### Protocol:

1. Prepare specimen for dissection
  - Thaw frozen specimens at the appropriate temperature
  - Rinse and clean specimens if needed
2. Cutout region for biaxial testing from sample
  - Biaxial specimens should be rectangular in shape
3. Insert suture staples along each side of the specimen
  - 2 suture loops (consisting of a total of 4 suture staples) should be attached to each side of the specimen
  - Care should be taken to space the 4 suture staples evenly across each specimen edge
  - Insert suture staples at least 1 mm away from the edge to prevent sutures from ripping out during testing. This spacing recommendation is a general rule and may have to be increased for materials that rip easily.
4. Glue or otherwise attach markers to the central region of the biaxial testing sample
  - The biaxial software can track either 4 (in a 2 x 2 array) or 9 (in a 3 x 3 array) markers
  - The marker array should be applied to the central region of the sample, spaced away from the suture staples to ensure an even stress distribution within the marker region.
  - Markers can be dark (on a light specimen) or light (on a dark specimen). Adequate contrast between the specimen and the markers is crucial to the success of the experiment.

#### 4.4 - Mounting the Specimen in the Biaxial Testing Device

##### Notes:

1. The mounting process is considered by many to be the crux of biaxial testing. It requires patience and practice. You can do it!
2. The suture attachment pulley pieces can be removed by unscrewing the thumbscrew located above each pulley attachment. When twisting the thumbscrew on a carriage that contains a load cell, be careful to hold the metal load cell-contacting arm away from the load cell to prevent from accidentally applying a force to the load cell.
3. It may be helpful to turn the power to the motors off in order to allow manual carriage position adjustment during the mounting procedure.

##### Protocol:

1. Steps 2-5 can be completed before preparing the specimen if desired.
2. Fill the specimen bath with the appropriate fluid
3. Begin external bath flow loop (if applicable)
4. Wait for bath parameters (i.e. temperature, gas concentrations) to reach appropriate stable condition.
5. Attach suture loops to device pulleys by lifting pulley caps, looping suture around pulley and dropping pulley cap over suture line.
6. Once the specimen is successfully mounted, make sure the power to the motors is on.
7. Click the "Positioning" tab (3.1) at the top of the software screen.
8. Adjust the motor speed on the "Motor Speed (mm/s)" scroll bar (3.3).
9. Using the "Free Movement" buttons (3.2), center the specimen within the bath. Note that the free movement directions should correspond to directions relative to the image window.

## 4.5 - Setting Up the Imaging System

### Notes:

1. If the markers are lost by the software at any time after they are initialized, disable the "lock subregions" feature (2.2) and repeat steps 5-10.
2. Once the imaging system is properly setup, you can save a reference file (X & Y marker positions) for reference or to use in your testing protocols by clicking the "Save Reference File" (2.5) in the lower right corner of the imaging tab.
3. The "Compare References" button (2.6) allows you to automatically calculate the stretches between two reference files that you will be prompted to select after clicking the "Compare References" button.
4. Clicking any of the "Set" buttons (2.4) next to the "Marker Positions" graph (2.3) allows you to plot marker positions on the graph for comparison. It does NOT save the marker positions as a reference file and will not allow you to use the current marker positions as a reference for a test. See note 3 for details on saving reference files.

### Protocol:

1. Position and focus the camera such that the markers are centered in the image window and leave enough room so that the markers will not move out of the camera field of view during testing.
2. Select the "Imaging" tab (2.1) at the top of the screen.
3. Click the "Threshold Image" button in step 1 of the image setup box (2.2) and adjust the threshold value using the scroll bar until the markers are clearly visible and the thresholded image is clean and free of noise and image specks.
4. Move to step 2 of the image setup box and select the number of markers you would like to track (4 or 9).
5. Move to step 3 of the image setup box and click the "initialize" button to launch the subregion initialization.
6. Using the mouse, draw a box around each marker in the image window that appears, clicking the "OK" button after drawing each box. A textual

description of the marker you should be selecting is written in the upper right hand corner of the marker initialization window. Note that the marker subregions should not overlap and the markers should be the only objects in each subregion.

7. Upon returning to the main screen after completing the marker initialization, the marker subregions that you drew should be overlaid in green on the image window.
8. Move to step 5 of the image setup box and click the "turn on marker tracking button."
9. Move to step 6 of the image setup box and adjust the upper and lower marker size thresholds until the software recognizes all markers. You can tell if the software recognizes a marker by looking for the presence of a small green cross in the center of the marker. Additionally, recognized markers should be plotted on the "Marker Positions" graph (2.3).
10. Move to step 7 of the image setup box and click the "Lock Subregions" button. This will center the marker subregions on the markers and force the marker subregions to translate with the markers such that the markers remain centered within their respective subregions.

## 4.6 - Setting a Preload

### Notes:

1. The automatic preload feature works best if you first manually (Using the "Free Movement" buttons (3.2)) stretch the specimen such that the loads displayed on the "Loads" graph (3.8) on the bottom of the "Positioning" tab (3.1) are close to the desired loads.
2. The autoloading feature is used during an actual test in order to ensure that the specimen returns to the proper tare loads between test cycles, using the autoloading feature will give you an idea how this feature will perform during the actual test.
3. Selecting a tare load that is too low (typically below 0.5g) or an allowable error that is too small (typically below 0.05g) can cause errors in the autoloading algorithm.

### Protocol:

1. Click on the "Test Settings" tab (4.1 or 5.1) at the top of the screen
2. Enter the specimen dimensions in the provided input boxes (4.2 or 5.2).
3. Click on the "Positioning" tab at the top of the screen (3.1).
4. Select the desired units in the "Preload Units" selection box (3.5).
5. Enter the Allowable Error, X1 Preload and X2 Preload (3.6)
6. If desired, manually stretch the specimen until it is close to the desired tare loads using the "Free Movement" buttons (3.2).
7. Click the "Apply Load Button" (3.7)
8. The "Program Status" bar (3.9) at the bottom of the screen will display complete when the autoloading algorithm has finished.

## 4.7 - Running a Test

### Notes:

1. During or before the test, a live image can be toggled on or off by clicking the "Update Image" button (6.3) at the top of the "Run Test" tab (6.1).
2. A test can be cancelled by clicking the "cancel" button (6.3) at the top of the "Run Test" tab. If the device does not respond to this action and the device needs to stop immediately, shut off power to the motors.
3. During or before a test, you can choose to view the data for the current test cycle only or for all test cycles with the toggle (6.2) in the upper right corner of the "Run Test" tab.

### Protocol:

1. Click the "Test Settings" tab (4.1 or 5.1) at the top of the screen.
2. Input all test parameters
  - a. Specimen dimensions (4.2 or 5.2): insert the specimen dimensions in mm
  - b. Number of Cycles (4.3 or 5.3)
  - c. ½ Cycle Time (4.3 or 5.3): The time in seconds that the specimen will be loaded (or unloaded). The duration of one cycle will be  $2 \times \frac{1}{2}$  Cycle Time).
  - d. Correction Gain (4.8 or 5.8): The testing device makes corrections between cycles based on the assumption that the material is linear. The more nonlinear your material is, the lower your correction gain should be to prevent overshoot. A typical correction gain for valve materials is 0.3.
3. Parameters in Load Control Only (4.1)
  - a. Control (4.5): Determine the units and type of control for the load test
  - b. Axis 1 & Axis 2 (4.6): Input the desired peak loads for each axis in the units specified in "Control"
  - c. Estimated Stretch 1 & 2 (4.7): Initial guesses for the stretches that will be required to stretch the specimen to the desired peak loads.
  - d. Allowable Stretch 1 & 2 (4.4): Safety limits for the stretches on each axis. If an axis is stretched beyond the allowable stretch the test will be stopped immediately.

4. Parameters in Stretch Control Only (5.1)
  - a. Stretch Ratio (5.4): the ratio of (stretch1-1) to (stretch2-1) desired for the peak stretches
  - b. Use Load Limits for this Test (5.5): If this option is selected, the test protocol will consist of the specimen being stretched at the ratio specified in "Stretch Ratio" until one of the load limits is reached on one axis (or both simultaneously). This option cannot be used in conjunction with "Use Stretch Limits for this Test," and should be unselected before selecting that option.
    - i. Max Loads (5.5): select the units for the max loads
    - ii. Axis 1 & 2 (5.6): the load limits that will be used if "Use Load Limits for this Test" is selected.
  - c. Use Stretch Limits for this Test (5.7): if this option is selected the test protocol will consist of the specimen being stretched at the ratio specified in "Stretch Ratio" until the stretch limit is reached on one axis (or both simultaneously). This option cannot be used in conjunction with "Use Load Limits for this Test," and should be unselected before selecting that option.
    - i. Stretch 1 & 2 (5.7): stretch limits that will be used if "Use Stretch Limits for this Test" is selected.
5. Click the "Run Test" tab (6.1) at the top of the screen.
6. Click the green "Start Test" button (6.3) at the top of the tab.
7. When prompted, enter a base file name for the test. The software will automatically write test data for each test cycle in a file named: <user entered base file name>\_<cycle #>.bx
8. When prompted, select a reference file to use for the test.
9. Sit back and watch the show.

## **Section 5: Biaxial Tester Output Files**

### ***BX Files***

Each file that is automatically generated during the biaxial test procedure (.bx file) is a tab delimited file that can be opened in Microsoft Excel or most other spreadsheet programs or text editors. The headings for these files are:

Time (ms), Stretch 1, Stretch 2, Shear Angle, Load 1 (g), Load 2 (g), Tension 1 (N/m), Tension 2 (N/m), Stress 1 (kPa), Stress 2 (kPa), x1, x2, x3, x4, x5, x6, x7, x8, x9, y1, y2, y3, y4, y5, y6, y7, y8, y9

### ***REF Files***

REF files are saved reference files that are saved by the user and used by the Biax software during test protocols. Each REF file is a tab delimited file that can be opened in Microsoft Excel or most other spreadsheet programs or text editors if further analysis is necessary. The field order is:

X1, X2, X3, X4, X5, X6, X7, X8, X9, Y1, Y2, Y3, Y4, Y5, Y6, Y7, Y8, Y9

## Section 6: Software, Drivers and Virtual Channels

### *Software & Drivers:*

<b>Manufacturer</b>	<b>Name</b>	<b>Version</b>
National Instruments	Measurement & Automation Explorer	3.0.0.3014
National Instruments	IMAQ Vision	6.0
National Instruments	IVI Engine	1.6
National Instruments	Labview Run-Time	6.0
National Instruments	Labview	6.0
National Instruments	NI-Spy	2.0.0.16
National Instruments	NI-488.2 Software	1.60
National Instruments	NI-DAQ	6.9.3f3
National Instruments	NI-IMAQ Software	2.5.5
National Instruments	NI-IMAQ for 1394	1.5
National Instruments	NI-PAL Software	1.6.3f0
National Instruments	NI-VISA	3.0
Galil Motion Control	DMC-18x0 Motion Controller Driver	4.0.3.0

### *Virtual Channels:*

<b>Channel Type</b>	<b>Name</b>	<b>Description</b>
Analog Input	X-Axis Load Cell	Differential Channel 0
Analog Input	Y-Axis Load Cell	Differential Channel 1
Analog Output	negative trigger	Channel 0: DAC0OUT, High-Speed System Only
Analog Output	positive trigger	Channel 1: DAC1OUT, High-Speed System Only

### *Biaxial Software Versions:*

Load Control 1.0: Quasi-static load control

Load Control 2.0: Quasi-static load control + Stress Relaxation

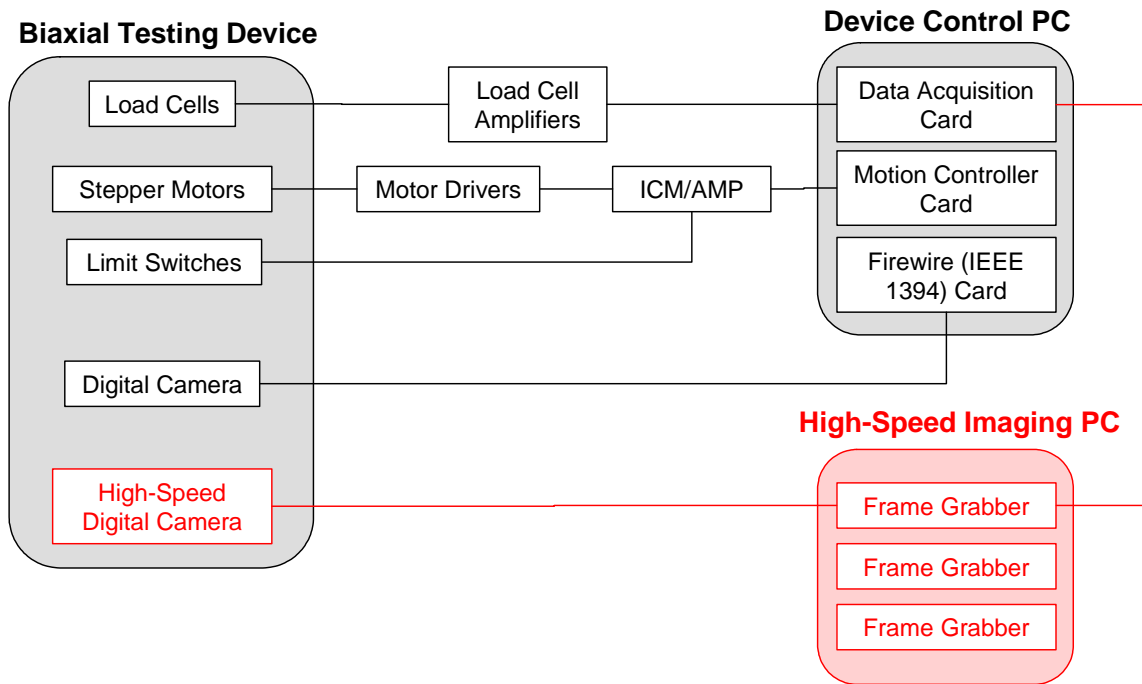
Load Control 3.0: Quasi-static load control + High stretch rate testing

Load Control 4.0: Quasi-static load control + Biaxial Creep

Stretch Control 1.0: Quasi-static stretch control

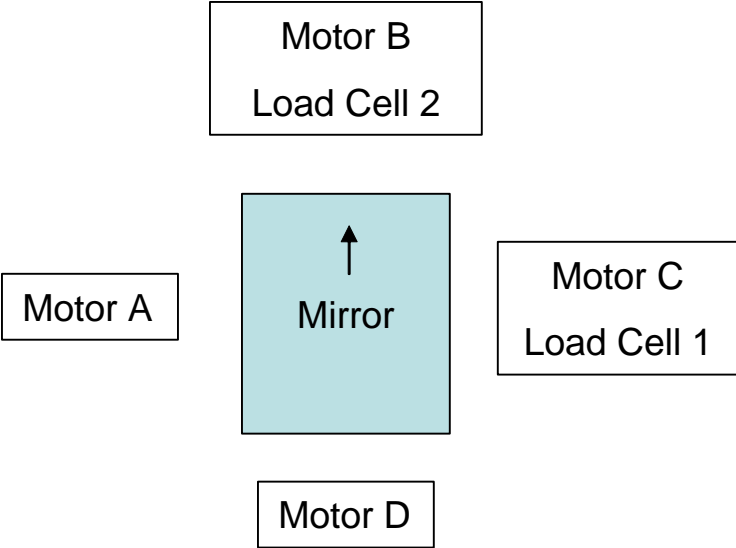
## Section 7: System Diagrams

### 7.1 System Overview

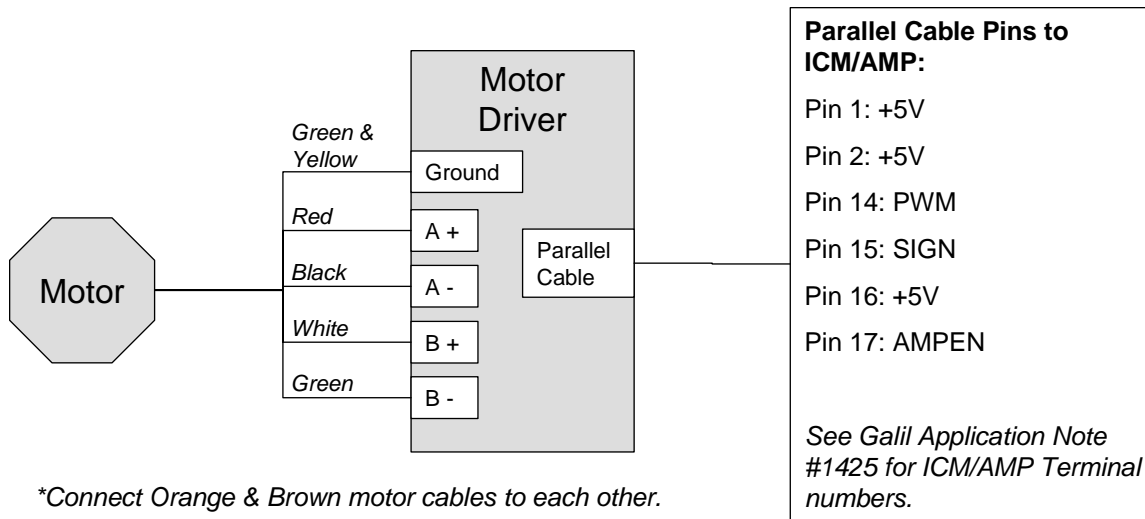


*\*Items in red are only included in the High-Speed Systems*

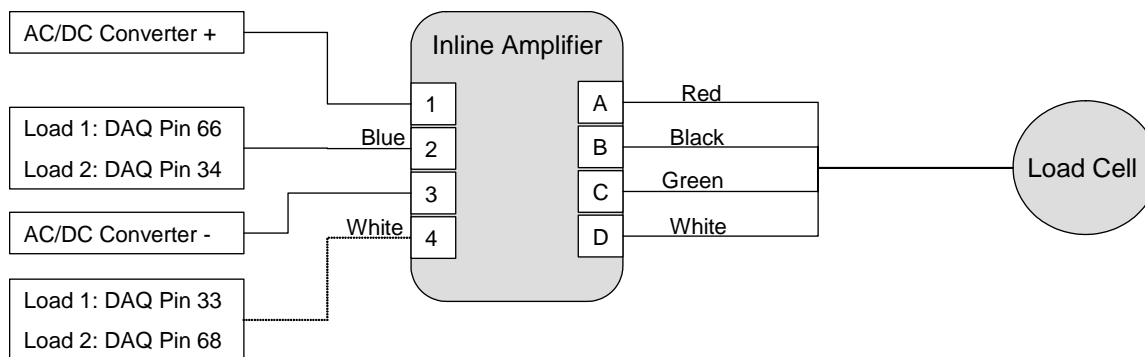
7.2 Setup Orientation



### 7.3 Motor Wiring Diagram

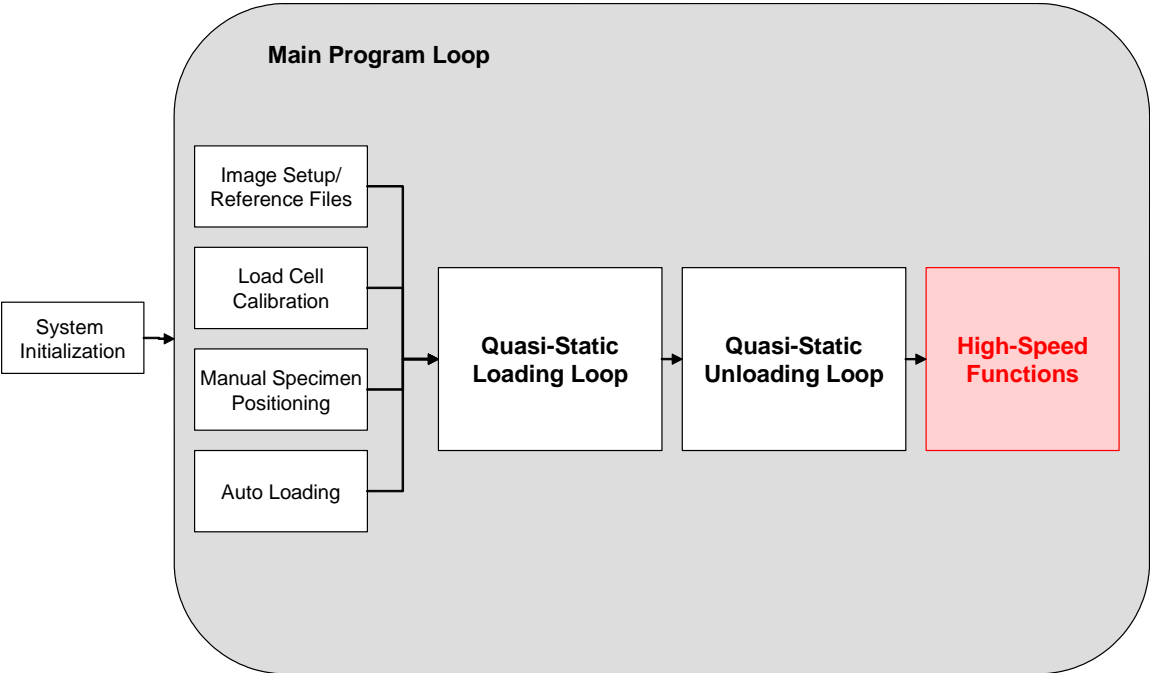


### 7.4 Load Cell Wiring Diagram



7.5 Software Overview

Use this diagram as a map of the LabView Wiring Diagram



*\*High-Speed functions are present only in Load Control 2.0, 3.0 and 4.0*

## Section 8: System Specifications

<b>Load Range</b>	0-1kg per carriage
<b>Actuator Max Speeds</b>	1 m/s
<b>Actuator Acceleration</b>	25 m/s <sup>2</sup>
<b>Actuator Displacements</b>	5 cm
<b>Displacement Precision</b>	0.4 $\mu$ m
<b>Camera Resolution</b>	1024 x 960
<b>Specimen Size Range</b>	0.5 x 0.5 to 4 x 4 cm

**APPENDIX C**

**HIGH-SPEED BIAxIAL TESTING MANUAL**

# Biaxial Testing Manual *High-Speed Testing Supplement*

*Author(s): Jonathan Grashow  
Version: 1.0  
Original Release Date: 3/16/05  
Last Revision Date: N/A*

# Contents

## **Section 1:** General Information

- 1.1 Warning
- 1.2 Program Descriptions

## **Section 2:** High-Speed Biaxial Testing Software Screens

- 2.1 Load Control 2.0 – Stress Relaxation
- 2.2 Load Control 3.0 – High Stretch Rate Testing
- 2.3 Load Control 4.0 - Creep

## **Section 3:** High-Speed Biaxial Testing Protocols

- 3.1 Stress Relaxation
- 3.2 High Stretch Rate Testing
- 3.3 Creep

## **Section 4:** High-Speed Biaxial Tester Output Files

Need to Add

## **Section 1: General Information**

### ***1.1 - Warning***

Please note that the high-speed biaxial testing programs (Load Control 2.0: Stress-Relaxation, Load Control 3.0: High stretch rate testing, and Load Control 4.0: Creep) are much more involved than the standard quasi-static Biaxial Testing programs. These three programs were all used to complete high-speed testing on the native Mitral Valve leaflet and their performance has not been qualified for other materials. It is strongly suggested that anyone who uses these programs have a good knowledge of LabView programming so that adjustments to the programs can be made as necessary. The high speeds involved in these tests increase the need for the user to be familiar with the device and its capabilities. Always make sure that limit switches are properly installed to avoid device damage.

### ***1.2 - Program Descriptions***

Each of the three high-speed testing programs works in a manner very similar to the quasi-static load control biaxial testing program (Load Control 1.0). Generally, each program is set up to run through a series of quasi-static test cycles (exactly like those in Load Control 1.0) then to perform a designated high-speed test at the end of the quasi-static testing based to the displacements determined in the quasi-static cycles.

### *Load Control 2.0: Stress-Relaxation*

This program runs a series of quasi-static cycles to user-defined load limits. After the final quasi-static cycle the program can be set to perform a stress-relaxation test, in which the specimen will be stretched from the preload state to the displacements that were determined to correspond to the load limits in the final quasi-static cycle. The specimen will be loaded in a user defined time and the carriage positions will then be locked for the duration of the experiment. This program triggers the high-speed camera to acquire stretch data in the loading phase of testing, then engages the standard digital camera to measure stretches for the remainder of the test.

### *Load Control 3.0: High-Speed Loading/Unloading*

This program runs a series of quasi-static cycles to user-defined load limits. After the final quasi-static cycle the program can be set to rapidly load and unload the specimen from the preload state to the displacements that were determined to correspond to the load limits in the final quasi-static cycle. The specimen will be subsequently loaded and unloaded in 1s, 0.5s, 0.25s, 0.1s, 0.05s and 1s  $\frac{1}{2}$  cycle times. This program triggers the high-speed camera to acquire stretch data during the high-speed testing.

### *Load Control 4.0: Creep*

This program runs a series of quasi-static cycles to user-defined load limits. After the final quasi-static cycle the program can be set to perform a creep test, in which the specimen will be stretched from the preload state to the displacements that were determined to correspond to the load limits in the final quasi-static cycle. The specimen is loaded in a user defined time after which a loading algorithm is engaged to maintain the specimen loads at user defined levels for the duration of testing. This program triggers the high-speed camera to acquire stretch data in the loading phase of testing, then engages the standard digital camera to measure stretches for the remainder of the test.

## Section 2: High Speed Biaxial Testing Software Screens

### 2.1 – Load Control 2.0: Stress Relaxation

The screenshot displays the 'High Speed Test' tab in the 'Load Control 2.0.vi' software. The interface includes a menu bar (File, Edit, Operate, Tools, Browse, Window, Help), a toolbar with icons for navigation and execution, and a series of tabs: Load Cells, Imaging, Positioning, Test Settings, Run Test, and High Speed Test. The 'High Speed Test' tab is active, showing a 'High-Speed Test' toggle button, 'Trigger Test' and 'Stop Test' buttons, and input fields for 'Loading Time' and 'Stop Test After' (both set to 0.00 s). On the right, there are input fields for 'Displacement 1' and 'Displacement 2' (both 0.00 mm) and 'Speed 1' and 'Speed 2' (both 0.0000 m/s). Below these are 'Stretch vs Time (ms)' and 'Loads ( ) vs Time (ms)' graphs. The 'Stretch vs Time' graph shows a linear decrease from 1.50 to 1.00 over 11000.0 ms. The 'Loads vs Time' graph shows a constant load of 0.0000 over the same duration. At the bottom, there is a 'Program Status' bar and a 'Stop Program' button. Red arrows point from numbered labels (1.1-1.9) to specific UI elements.

1.1 High Speed Test Tab

1.2 Stop Test Button

1.3 Trigger Test Button

1.4 Test Statistics Display

1.5 High-Speed Test Toggle

1.6 Loading Time Input

1.7 Test Duration Input

1.8 Stretch vs Time Graph

1.9 Load vs Time Graph

## 2.2 – Load Control 3.0: High Stretch Rate Testing

The screenshot shows the 'High Speed Test' tab of the 'Load Control 3.0.vi' software. The interface includes a menu bar (File, Edit, Operate, Tools, Browse, Window, Help), a toolbar, and a main control area. The 'High Speed Test' tab is active, showing a 'High-Speed Test' toggle, 'Trigger Test' and 'Stop Test' buttons, and input fields for Displacement 1 and 2 (0.00 mm), Speed 1 and 2 (0.0000 m/s), and Motor Delay (0.0000 ms). A 'Recalibrate LC' toggle and 'Apply Preload' toggle are also present, along with 'Axis 1 Return Factor' and 'Axis 2 Return Factor' input fields (both 0.00). A 'Time Remaining' display shows 0.00. At the bottom, a 'Program Status' bar and a 'Stop Program' button are visible. A 'Load vs Time Graph' is shown with a grid and axes ranging from 0 to 3000 ms on the x-axis and -10.0 to 80.0 on the y-axis. Red arrows point from numbered callouts to these various elements.

2.1 High Speed Test Tab

2.2 Stop Test Button (Disabled)

2.3 Trigger Test Button

2.4 Test Statistics Display

2.5 High-Speed Test Toggle

2.6 Load vs Time Graph

2.7 Recalibrate LC Button

2.8 Axis Return Factor Inputs

2.9 Apply Preload Toggle

## 2.3 – Load Control 4.0: Creep

The screenshot shows the 'Load Control 4.0.vi' software interface. The 'High Speed Test' tab is selected. The interface includes a 'High-Speed Test' toggle, 'Trigger Test' and 'Stop Test' buttons, and various input fields for displacement, speed, and creep stretch limits. Two graphs are displayed: 'Stretch vs Time (ms)' and 'Loads (g) vs Time (ms)'. A 'Program Status' bar at the bottom shows 'Unloading Specimen' and a 'Stop Program' button. Red arrows point from numbered labels to specific UI elements.

3.1 High Speed Test Tab

3.2 Stop Test Button

3.3 Trigger Test Button

3.4 Test Statistics Display

3.5 High-Speed Test Toggle

3.6 Test Duration Input

3.7 Creep Stretch Limits

3.8 Stretch vs Time Graph

3.9 Load vs Time Graph

## Section 3: High-Speed Biaxial Testing Protocols

### 3.1 – Stress Relaxation

#### Notes:

1. Load Control 2.0 is simply an expansion of Load Control 1.0. All quasi-static protocols can be run using Load Control 2.0.
2. The displacements used in the stress-relaxation loading are based on the displacements of the final quasi-static loading cycle. If anything is unusual with the final quasi-static cycle it is not recommended to proceed with the stress-relaxation test.
3. It is strongly recommended that all stress-relaxation tests are preceded by a standard quasi-static biaxial protocol to ensure that no abnormal characteristics are present in the test sample.
4. Currently a bug in the software causes every second stress-relaxation experiment to stop prematurely. For this reason it is recommended that you save all necessary calibration files and reference files, and manually shut down and restart the program between sequential stress-relaxation experiments; or fix this bug.

#### Protocol:

1. Input the desired quasi-static test settings (Refer to Biax Manual for instructions).
2. Click the “High Speed Test” Tab. (1.1)
3. Enter the desired loading time (in seconds) in the loading time input box. (1.6)
4. Enter the desired duration for the stress-relaxation portion of the experiment in the test duration input. (1.7)
5. Click the High-Speed Test toggle (1.5) such that the indicator light turns to bright green. Clicking this toggle will direct the biaxial testing software to perform the stress-relaxation test after completing the quasi-static protocol. Make sure to disable this toggle (by clicking the toggle again such that the indicator light is black) before proceeding with any additional quasi-static only experiments.

6. Select the Test Settings tab and run a quasi-static experiment as detailed in the Biax Manual.
7. After the quasi-static protocol is completed, the software will wait for the user to click the "Trigger Test" button (1.3) on the High Speed Test tab. Before you trigger the test check the final cycle of the quasi-static protocol to ensure that nothing abnormal occurred and that the carriage displacements resulted in a condition very close to the desired loads. If you are using the high-speed camera to track stretches during the initial loading phase, ensure that the camera is ready to receive the analog trigger signal from the biaxial testing software.
8. Press the "Trigger Test" button.
9. The specimen should be loaded in the user defined duration and the stretches as loads should be plotted in real-time on the screen.
10. The test will continue for the user specified duration unless you select the "Stop Test" button (1.2).

## 3.2 High Stretch Rate Testing

### Notes:

1. Load Control 3.0 is simply an expansion of Load Control 1.0. All quasi-static protocols can be run using Load Control 3.0.
2. The displacements used in the rapid loading and unloading cycles are based on the displacements of the final quasi-static loading cycle. If anything is unusual with the final quasi-static cycle it is not recommended to proceed with the high-speed test.
3. It is strongly recommended that all high stretch rate tests are preceded by a standard quasi-static biaxial protocol to ensure that no abnormal characteristics are present in the test sample.
4. The "Axis Return Factors" (2.8) allow the user to multiply the return stroke during the high-speed testing by the appointed return factor in order to account for overshoot or instabilities in the high speed protocols. Though these factors are present, no correction was ever needed (return factors = 1) in the mitral valve testing. Take care that a large number is not accidentally input into one of these fields as this could be devastating to your sample and the device if the limit switches are improperly installed.
5. The "Recalibrate LC" button allows the user to recalibrate the load cells between high-speed cycles. This was found to be unnecessary and this toggle should not be used since it was never fully qualified.
6. The "Apply Preload" toggle causes the testing software to reapply the specified preload (See Specimen Positioning in the Biax Manual) between high speed cycles. Better results were obtained in mitral valve testing when this feature was disabled (indicator light black).

### Protocol:

1. Input the desired quasi-static test settings (Refer to Biax Manual for instructions).
2. Click the "High Speed Test" Tab. (2.1)
3. Enter 1.0 in both of the "Axis Return Factor Inputs" (2.8)

4. Verify that the "Recalibrate LC" (2.7) and "Apply Preload" (2.9) toggles are deactivated (indicator lights black).
5. Click the High-Speed Test toggle (1.5) such that the indicator light turns to bright green. Clicking this toggle will direct the biaxial testing software to perform the high stretch rate tests after completing the quasi-static protocol. Make sure to disable this toggle (by clicking the toggle again such that the indicator light is black) before proceeding with any additional quasi-static only experiments.
6. Select the Test Settings tab and run a quasi-static experiment as detailed in the Biax Manual.
7. After the quasi-static protocol is completed, the software will wait for the user to click the "Trigger Test" button (1.3) on the High Speed Test tab. Before you trigger the test check the final cycle of the quasi-static protocol to ensure that nothing abnormal occurred and that the carriage displacements resulted in a condition very close to the desired loads. If you are using the high-speed camera to track stretches during the high speed cycles, ensure that the camera is ready to receive the analog trigger signal from the biaxial testing software.
8. Press the "Trigger Test" button.
9. The specimen should be loaded and unloaded in 1s and the load vs time curve should be plotted on the screen after the motion has completed.
10. If everything in the high-speed cycle went normally repeat steps 7-10 for each high speed protocol. Make sure to setup the high speed camera to receive the analog trigger before triggering each test.

### 3.3 – Creep

#### Notes:

1. Load Control 4.0 is simply an expansion of Load Control 1.0. All quasi-static protocols can be run using Load Control 4.0.
2. The displacements used in the creep initial loading are based on the displacements of the final quasi-static loading cycle. If anything is unusual with the final quasi-static cycle it is not recommended to proceed with the creep test.
3. It is strongly recommended that all creep tests are preceded by a standard quasi-static biaxial protocol to ensure that no abnormal characteristics are present in the test sample.
4. Currently a bug in the software causes every creep experiment to stop prematurely. For this reason it is recommended that you save all necessary calibration files and reference files, and manually shut down and restart the program between sequential creep experiments; or fix this bug.
5. The creep loading algorithm is used after the initial loading phase to maintain the desired specimen loads. This algorithm was tuned to prevent large loading oscillations for the mitral valve and may require adjustment for other materials.
6. Unlike the stress-relaxation software, the creep software does not allow the user to define the loading time. All loading is done in 100ms unless modified on the programming level.
7. The creep algorithm automatically loads the specimen to the peak levels defined in the Test Settings Tab (See Biax Manual). This was convenient for the mitral valve since the valve was stretch-rate insensitive, but this may need to be modified for other materials since loading the specimen in 100ms instead of quasi-statically may result in much higher load levels.

#### Protocol:

1. Input the desired quasi-static test settings (Refer to Biax Manual for instructions).

2. Click the "High Speed Test" Tab. (3.1)
3. Enter the desired duration for the creep portion of the experiment in the test duration input. (3.6)
4. Enter the desired "Creep Stretch Limits" (3.7). This is a safety function. If these limits are reached, the software will automatically stop the test.
5. Click the High-Speed Test toggle (3.5) such that the indicator light turns to bright green. Clicking this toggle will direct the biaxial testing software to perform the creep test after completing the quasi-static protocol. Make sure to disable this toggle (by clicking the toggle again such that the indicator light is black) before proceeding with any additional quasi-static only experiments.
6. Select the Test Settings tab and run a quasi-static experiment as detailed in the Biax Manual.
7. After the quasi-static protocol is completed, the software will wait for the user to click the "Trigger Test" button (3.3) on the High Speed Test tab. Before you trigger the test check the final cycle of the quasi-static protocol to ensure that nothing abnormal occurred and that the carriage displacements resulted in a condition very close to the desired loads. If you are using the high-speed camera to track stretches during the initial loading phase, ensure that the camera is ready to receive the analog trigger signal from the biaxial testing software.
8. Press the "Trigger Test" button.
9. The specimen should be loaded in the user defined duration and the stretches and loads should be plotted in real-time on the screen.
10. The test will continue for the user specified duration unless you select the "Stop Test" button (1.2).

## Section 4: High Speed Biaxial Tester Output Files

### *Stress Relaxation:*

"<Filename>\_first\_second.hsbx": This file contains the first second of data from stress-relaxation test. File column headings are: Time (ms), Load 1 (units selected in Test Settings Tab), Load 2 (units selected in Test Settings Tab).

"<Filename>\_entire\_test.hsbx": This file contains all data from the stress-relaxation test. File column headings are: Time (ms), Stretch 1, Stretch 2, Shear Angle (degrees), Load 1 (N or g), Load 2 (N or g), Tension 1 (N/m), Tension 2 (N/m), Stress 1 (kPa), Stress 2 (kPa).

### *High Stretch-Rate Testing:*

Each data file for the High Stretch Rate testing includes time and load data for approximately 2 x the half cycle time + 1 additional second of data all at the noted acquisition rate. File Headings for each file are: Time (ms), Load 1 (units selected in Test Settings Tab), Load 2 (units selected in Test Settings Tab).

"<Filename>\_HS 0.hsbx": 1 second ½ cycle time, 50 Hz acquisition rate.

"<Filename>\_HS 1.hsbx": 0.5 second ½ cycle time, 100 Hz acquisition rate.

"<Filename>\_HS 2.hsbx": 0.1 second ½ cycle time, 500 Hz acquisition rate.

"<Filename>\_HS 3.hsbx": 0.05 second ½ cycle time, 500 Hz acquisition rate.

"<Filename>\_HS 4.hsbx": 1 second ½ cycle time, 50 Hz acquisition rate.

### *Creep:*

"<Filename>\_first\_second.hsbx": This file contains the first second of data from creep test. File column headings are: Time (ms), Load 1 (units selected in Test Settings Tab), Load 2 (g or N).

"<Filename>\_entire\_test.hsbx": This file contains all data from the creep test. File column headings are: Time (ms), Stretch 1, Stretch 2, Shear Angle (degrees), Load 1 (N or g), Load 2 (N or g), Tension 1 (N/m), Tension 2 (N/m), Stress 1 (kPa), Stress 2 (kPa).

## BIBLIOGRAPHY

1. Lam, J.H., N. Ranganathan, E.D. Wigle, and M.D. Silver, Morphology of the human mitral valve. I. Chordae tendineae: a new classification. *Circulation*, 1970. **41**(3): p. 449-58.
2. Ormiston, J.A., P.M. Shah, C. Tei, and M. Wong, Size and motion of the mitral valve annulus in man. I. A two-dimensional echocardiographic method and findings in normal subjects. *Circulation*, 1981. **64**(1): p. 113-20.
3. Otto, C.M., *Valvular Heart Disease*. 2nd ed. 2004, Philadelphia: Saunders.
4. Ranganathan, N., J.H. Lam, E.D. Wigle, and M.D. Silver, Morphology of the human mitral valve. II. The valve leaflets. *Circulation*, 1970. **41**(3): p. 459-67.
5. Silverman, M.E. and J.W. Hurst, The mitral complex. Interaction of the anatomy, physiology, and pathology of the mitral annulus, mitral valve leaflets, chordae tendineae, and papillary muscles. *Am Heart J*, 1968. **76**(3): p. 399-418.
6. Wells, S., *Mitral Valve Disease*. 1996, Oxford: Butterworth-Heinemann.
7. Fulchiero, G., S.M. Wells, T.L. Sellaro, E. Rabkin, F.J. Schoen, and M.S. Sacks, Alterations in Collagen Fiber Crimp morphology with Cyclic Loading in Zero and Low Pressure-Fixed porcine bioprosthetic heart valves. *Biomaterials*, in-press.
8. Curtis, M.B. and D.V. Priola, Mechanical properties of the canine mitral valve: effects of autonomic stimulation. *Am J Physiol*, 1992. **262**(1 Pt 2): p. H56-62.
9. Marron, K., M.H. Yacoub, J.M. Polak, M.N. Sheppard, D. Fagan, B.F. Whitehead, M.R. de Leval, R.H. Anderson, and J. Wharton, Innervation of human atrioventricular and arterial valves. *Circulation*, 1996. **94**(3): p. 368-75.
10. Sacks, M.S., D.B. Smith, and E.D. Hiester, A small angle light scattering device for planar connective tissue microstructural analysis. *Ann Biomed Eng*, 1997. **25**(4): p. 678-89.
11. Wood, P., An appreciation of mitral stenosis. I. Clinical features. *Br Med J*, 1954. **4870**: p. 1051-63; contd.
12. Burge, D.J. and R.J. DeHoratius, Acute rheumatic fever. *Cardiovasc Clin*, 1993. **23**: p. 3-23.

13. Glower, D.D., K.P. Landolfo, R.D. Davis, Y.Y. Cen, J.K. Harrison, T.M. Bashore, J.E. Lowe, and W.G. Wolfe, Comparison of open mitral commissurotomy with mitral valve replacement with or without chordal preservation in patients with mitral stenosis. *Circulation*, 1998. **98**(19 Suppl): p. II120-3.
14. Baptist Health Foundation, I., The Autonomic Disorders Mitral Valve Prolapse Center. 2003, Webspaces Enterprises.
15. Kontos, J., V. Papademetriou, K. Wachtell, V. Palmieri, J.E. Liu, E. Gerdtts, K. Boman, M.S. Nieminen, B. Dahlof, and R.B. Devereux, Impact of valvular regurgitation on left ventricular geometry and function in hypertensive patients with left ventricular hypertrophy: the LIFE study. *J Hum Hypertens*, 2004. **18**(6): p. 431-6.
16. Pierard, L.A. and P. Lancellotti, The role of ischemic mitral regurgitation in the pathogenesis of acute pulmonary edema. *N Engl J Med*, 2004. **351**(16): p. 1627-34.
17. Alfieri, O. and F. Maisano, An effective technique to correct anterior mitral leaflet prolapse. *J Card Surg*, 1999. **14**(6): p. 468-70.
18. Borer, J.S. and K. Kupfer, Mitral Regurgitation: Current Treatment Options and Their Selection. *Curr Treat Options Cardiovasc Med*, 2004. **6**(6): p. 509-517.
19. El Khoury, G., P. Noirhomme, R. Verhelst, J. Rubay, and R. Dion, Surgical repair of the prolapsing anterior leaflet in degenerative mitral valve disease. *J Heart Valve Dis*, 2000. **9**(1): p. 75-80; discussion 81.
20. Perier, P., B. Clausnizer, and K. Mistarz, Carpentier "sliding leaflet" technique for repair of the mitral valve: early results. *Annals of Thoracic Surgery*, 1994. **57**: p. 383-386.
21. Smedira, N.G., R. Selman, D.M. Cosgrove, P.M. McCarthy, B.W. Lytle, P.C. Taylor, C. Apperson-Hansen, R.W. Stewart, and F.D. Loop, Repair of anterior leaflet prolapse: chordal transfer is superior to chordal shortening. *J Thorac Cardiovasc Surg*, 1996. **112**(2): p. 287-91; discussion 291-2.
22. David, T.E., M. Komeda, C. Pollick, and R.J. Burns, Mitral valve annuloplasty: the effect of the type on left ventricular function. *Ann Thorac Surg*, 1989. **47**(4): p. 524-7; discussion 527-8.
23. Kreindel, M.S., W.A. Schiavone, H.M. Lever, and D. Cosgrove, Systolic anterior motion of the mitral valve after Carpentier ring valvuloplasty for mitral valve prolapse. *Am J Cardiol*, 1986. **57**(6): p. 408-12.
24. Yacoub, M.H. and L.H. Cohn, Novel approaches to cardiac valve repair: from structure to function: Part II. *Circulation*, 2004. **109**(9): p. 1064-72.

25. Yoganathan, A., Cardiac Valve Prostheses, in *The Biomedical Engineering Handbook*. 1995, CRC Press: Boca Raton.
26. Hashim, S.R., A. Fontaine, S. He, R.A. Levine, and A.P. Yoganathan, A three-component force vector cell for in vitro quantification of the force exerted by the papillary muscle on the left ventricular wall. *J Biomech*, 1997. **30**(10): p. 1071-5.
27. He, S., A.A. Fontaine, E. Schwammenthal, A.P. Yoganathan, and R.A. Levine, Integrated mechanism for functional mitral regurgitation: leaflet restriction versus coapting force: in vitro studies. *Circulation*, 1997. **96**(6): p. 1826-34.
28. Perloff, J.K. and W.C. Roberts, The mitral apparatus: functional anatomy of mitral regurgitation. *Circulation*, 1972. **46**: p. 227-239.
29. Tsakiris, A.G., R. Padiyar, D.A. Gordon, and I. Lipton, Left atrial size and geometry in the intact dog. *Am J Physiol*, 1977. **232**(2): p. H167-72.
30. Karlsson, M.O., J.R. Glasson, A.F. Bolger, G.T. Daughters, M. Komeda, L.E. Foppiano, D.C. Miller, and N.B. Ingels, Jr., Mitral valve opening in the ovine heart. *Am J Physiol*, 1998. **274**(2 Pt 2): p. H552-63.
31. Tsakiris, A.G., D.A. Gordon, Y. Mathieu, and L. Irving, Motion of both mitral valve leaflets: a cinerentgenographic study in intact dogs. *J Appl Physiol*, 1975. **39**(3): p. 359-66.
32. Sacks, M.S., Z. He, L. Baijens, S. Wanant, P. Shah, H. Sugimoto, and A.P. Yoganathan, Surface strains in the anterior leaflet of the functioning mitral valve. *Annals of Biomedical Engineering*, 2002. **30**(10): p. 1281-90.
33. Iyengar, A.K.S., H. Sugimoto, D.B. Smith, and M.S. Sacks, Dynamic in vitro quantification of bioprosthetic heart valve leaflet motion using structured light projection. *Ann Biomed Eng*, 2001. **29**(11): p. 963-73.
34. May-Newman, K. and F.C. Yin, Biaxial mechanical behavior of excised porcine mitral valve leaflets. *Am J Physiol*, 1995. **269**(4 Pt 2): p. H1319-27.
35. Billiar, K.L. and M.S. Sacks, Biaxial mechanical properties of the native and glutaraldehyde-treated aortic valve cusp: Part II--A structural constitutive model. *Journal of Biomechanical Engineering*, 2000. **122**(4): p. 327-35.
36. Fung, Y.C., *Biomechanics: Motion, Flow, Stress, and Growth*. 1990, New York: Springer-Verlag. 569.
37. Fung, Y.C., *Biomechanics: Mechanical Properties of Living Tissues*. 1981, New York: Springer-Verlag.

38. Woo, S.L., M.A. Gomez, and W.H. Akeson, The time and history-dependent viscoelastic properties of the canine medial collateral ligament. *J Biomech Eng*, 1981. **103**(4): p. 293-8.
39. Nagatomi, J., D.C. Gloeckner, M.B. Chancellor, W.C. DeGroat, and M.S. Sacks, Changes in the biaxial viscoelastic response of the urinary bladder following spinal cord injury. *Ann Biomed Eng*, 2004. **32**(10): p. 1409-19.
40. Liao, J. and I. Vesely, Relationship between collagen fibrils, glycosaminoglycans, and stress relaxation in mitral valve chordae tendineae. *Ann Biomed Eng*, 2004. **32**(7): p. 977-83.
41. Lim, K.O. and D.R. Boughner, Low frequency dynamic viscoelastic properties of human mitral valve tissue. *Cardiovasc Res*, 1976. **10**(4): p. 459-65.
42. Leeson-Dietrich, J., D. Boughner, and I. Vesely, Porcine Pulmonary and Aortic Valves: A Comparison of Their Tensile Viscoelastic Properties at Physiological Strain Rates. *The Journal of Heart Valve Disease*, 1995. **4**: p. 88-94.
43. Naimark, W.A., Structure/function relations in mammalian pericardial tissue: implications for comparative and developmental physiology. 1995, University of Toronto.
44. Lydon, C., J. Crisco, M. Panjabi, and M. Galloway, Effect of elongation rate on the failure properties of the rabbit anterior cruciate ligament. *Clin Biomech (Bristol, Avon)*, 1995. **10**(8): p. 428-433.
45. Haut, R.C., Age-dependent influence of strain rate on the tensile failure of rat-tail tendon. *J Biomech Eng*, 1983. **105**(3): p. 296-9.
46. Lee, J.M., D.W. Courtman, and D.R. Boughner, The glutaraldehyde-stabilized porcine aortic valve xenograft. I. Tensile viscoelastic properties of the fresh leaflet material. *J Biomed Mater Res*, 1984. **18**(1): p. 61-77.
47. Provenzano, P., R. Lakes, T. Keenan, and R. Vanderby, Jr., Nonlinear ligament viscoelasticity. *Ann Biomed Eng*, 2001. **29**(10): p. 908-14.
48. Dunn, M.G. and F.H. Silver, Viscoelastic behavior of human connective tissues: relative contribution of viscous and elastic components. *Connect Tissue Res*, 1983. **12**(1): p. 59-70.
49. Thornton, G.M., A. Oliynyk, C.B. Frank, and N.G. Shrive, Ligament creep cannot be predicted from stress relaxation at low stress: a biomechanical study of the rabbit medial collateral ligament. *J Orthop Res*, 1997. **15**(5): p. 652-6.

50. Vesely, I., D.R. Boughner, and J. Leeson-Dietrich, Bioprosthetic Valve Tissue Viscoelasticity: Implications on Accelerated Pulse Duplicator Testing. *Annals of Thoracic Surgery*, 1995. **60**: p. S379-383.
51. Sacks, M.S., Biaxial mechanical evaluation of planar biological materials. *Journal of Elasticity*, 2000. **61**: p. 199-246.
52. May-Newman, K. and F.C. Yin, A constitutive law for mitral valve tissue. *J Biomech Eng*, 1998. **120**(1): p. 38-47.
53. Hoffman, A.H. and P. Grigg, A Method for Measuring Strains in Soft Tissue. *Journal of Biomechanics*, 1984. **10**: p. 795-800.
54. Sacks, M.S. and W. Sun, Multiaxial Mechanical Behavior of Biological Materials. *Annu Rev Biomed Eng*, 2003.
55. Butler, D.L., S.A. Goldstein, and F. Guilak, Functional tissue engineering: the role of biomechanics. *J Biomech Eng*, 2000. **122**(6): p. 570-5.
56. Lanir, Y., Constitutive Equations for Fibrous Connective Tissues. *journal of biomechanics*, 1983. **16**: p. 1-12.
57. Lanir, Y., A Structural Theory for the Homogeneous Biaxial Stress-Strain Relationships in Flat Collageneous Tissues. *Journal of Biomechanics*, 1979. **12**: p. 423-436.
58. Kunzelman, K.S., M.S. Sacks, R.P. Cochran, and R.C. Eberhart, Mitral Valve Leaflet Collagen Distribution by Laser Analysis, in *Seventh Southern Biomedical Engineering Conference*. 1988. p. 82-85.
59. Naimark, W.A., J.M. Lee, H. Limeback, and D. Cheung, Correlation of structure and viscoelastic properties in the pericardia of four mammalian species. *American Journal of Physiology*, 1992. **263**(32): p. H1095-H1106.
60. Lee, J.M., D.R. Boughner, and D.W. Courtman, The glutaraldehyde-stabilized porcine aortic valve xenograft. II. Effect of fixation with or without pressure on the tensile viscoelastic properties of the leaflet material. *Journal of Biomedical Materials Research*, 1984. **18**: p. 79-98.
61. Rigby, B.J., N. Hirai, J.D. Spikes, and H. Eyring, The mechanical properties of rat tail tendon. *The Journal of General Physiology*, 1959. **43**: p. 265-282.
62. Lee, J.M. and D.R. Boughner, Mechanical properties of human pericardium. Differences in viscoelastic response when compared with canine pericardium. *Circ Res*, 1985. **57**(3): p. 475-81.

63. Liao, J., L. Yang, J. Grashow, and M.S. Sacks, Molecular orientation of collagen in intact planar connective tissues under biaxial stretch. *Acta Biomaterialia*, 2004. **1**(1).
64. Cole, W.G., D. Chan, A.J. Hickey, and D.E. Wilcken, Collagen composition of normal and myxomatous human mitral heart valves. *Biochem J*, 1984. **219**(2): p. 451-60.
65. Lis, Y., M.C. Burleigh, D.J. Parker, A.H. Child, J. Hogg, and M.J. Davies, Biochemical characterization of individual normal, floppy and rheumatic human mitral valves. *Biochem J*, 1987. **244**(3): p. 597-603.
66. Merryman, W.D., H.Y.S. Huang, F.J. Schoen, and M.S. Sacks, The effects of cellular contraction on aortic valve leaflet flexural stiffness. *Journal of Biomechanics*, In press.